

Numerical Methods for Collapsing Gravitational Waves

Dissertation

zur Erlangung des akademischen Grades
doctor rerum naturalium (Dr. rer. nat.)

vorgelegt dem Rat der Physikalisch-Astronomischen Fakultät
der Friedrich-Schiller-Universität Jena

von Dipl.-Phys. Andreas Weyhausen
geboren am 29. Juni 1982 in Leonberg

Gutachter:

1. Prof. Dr. Bernd Brüggemann, Friedrich-Schiller-Universität Jena
2. Prof. Dr. Wolfgang Tichy, Florida Atlantic University
3. Prof. Dr. Mark Hannam, Cardiff University

Tag der Disputation: 12. Mai 2015

Contents

1	Introduction	3
1.1	Numerical General Relativity	3
1.2	Collapsing gravitational waves	4
2	Setups of Numerical Relativity	7
2.1	The BSSN setup	8
2.2	The GHG setup	10
3	Evolution of collapsing gravitational waves with the BSSN setup	13
3.1	Evolution of Brill waves	13
3.2	Comparing Brill with Teukolsky wave evolutions	17
3.3	Brill waves with $A < 0$	20
4	A pseudospectral method for gravitational wave collapse	23
4.1	Formulation setup	23
4.1.1	GHG evolution equations, constraints and boundary conditions	23
4.1.2	Constraint preserving boundary conditions and damping . . .	31
4.2	The <code>bamps</code> code	33
4.2.1	Grid setup	33
4.2.2	Numerical method	36
4.2.3	Imposition of octant symmetry	38
4.2.4	Patching boundary conditions	40
4.2.5	Outer boundary implementation	41
4.2.6	Code implementation details	43
4.3	Energy estimate for the penalty factor	44
4.3.1	The continuum case	44
4.3.2	The semi-discrete case	46
5	Axisymmetric considerations	50
5.1	The analytic Cartoon method	50
5.2	Apparent horizons	53
5.3	Initial data	57

6	Code validation	60
6.1	Gauge boundary	60
6.2	Constraint experiments	61
6.3	Lapse power in constraint damping	62
6.4	BAM vs. bamps comparison	63
6.5	Octant and Cartoon	63
6.6	Convergence	66
6.7	Filtering	67
6.8	Performance	68
7	Evolution of single blackholes with bamps	71
7.1	Initial data	71
7.2	Freezing gauge source functions	72
7.3	Phasing-in the damped wave gauge	78
8	Evolution of collapsing Brill waves with bamps	82
8.1	Agreement with earlier work	82
8.2	Disagreement with Sorkin	86
8.3	Evolution of supercritical waves	88
8.4	Going to the critical regime	93
9	Conclusions	97
A	List of publications	101
B	List of presentations	103
C	Bibliography	105
D	Abbreviations and Notations	115
E	Acknowledgements	117
F	Lebenslauf	119
G	Ehrenwörtliche Erklärung	121
H	Zusammenfassung	123

1 Introduction

1.1 Numerical General Relativity

Around one hundred years ago, in 1915, Albert Einstein published his theory of General Relativity [45, 46]. It describes gravity as the curvature of spacetime, generated by the energy content of the universe. This fundamental relationship is expressed by the famous Einstein's equations

$$G_{ab} = 8\pi T_{ab}. \quad (1.1)$$

On the left side, the Einstein tensor G_{ab} represents the geometry of spacetime, whereas on the right side the stress-energy tensor T_{ab} contains the matter sources. Solutions to this set of equations are spacetimes describing a diverse set of interesting physics such as blackholes, neutron stars and gravitational waves. However, only few exact solutions to Einstein's equations, derived by the aims of analytical methods, are known [42, 67, 89, 90]. Additionally these solutions only describe idealized, highly symmetric systems. Solutions for more general scenarios, such as binary systems of compact objects or highly dynamical collapse scenarios cannot be provided by analytical methods. For many weak field scenarios, approximation methods, such as post-Newtonian methods [24, 87], are powerful tools to study the physics of General Relativity. But in strong field cases, such as the merger of binaries of compact objects, also these methods fail. Nowadays, the availability of supercomputers allows for a third approach namely that of Numerical Relativity [10, 21]. It uses numerical methods to simulate solutions of Einstein's equations on a computer. However, this is not an easy task. It is necessary to have an understanding of many different topics to be successfully master this challenge. In the context of this thesis such topics are:

Mathematics provides the necessary understanding to recast Einstein's equations in a form which is suitable for numerics.

Numerics is needed to have stable and accurate methods to approximate and simulate solutions of Einstein's equations on a computer.

Technology is essential to implement numerical methods in software and run simulations in a reasonable amount of time.

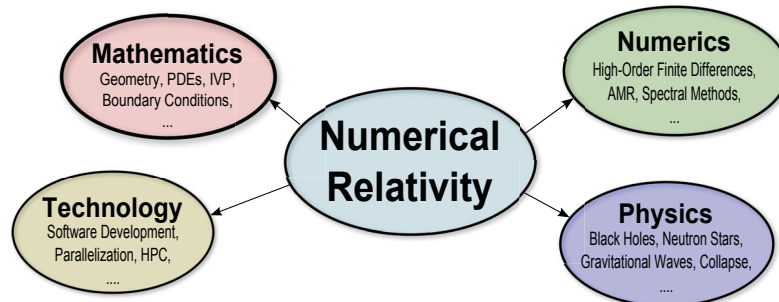


Figure 1: Many different topics have to be understood in order to successfully solve Einstein’s equations on a computer using the methods of Numerical Relativity.

Physics is the motivation and also the goal of all numerical studies of Einstein’s equations.

In its relatively short time of existence, Numerical Relativity has already produced many important results which contributed significantly to the understanding of the theory of gravity. It allowed the study of the physics of blackholes, neutron stars, merging binary systems, gravitational wave signals and collapsing spacetimes.

1.2 Collapsing gravitational waves

The main topic of this work is the simulation of gravitational waves, which are solutions to the vacuum Einstein equations¹

$$R_{ab} = 0, \tag{1.2}$$

where R_{ab} is the Ricci tensor. In the history of numerical relativity, gravitational waves have always played an important role, especially in the context of gravitational detection. The numerical simulation of binary systems allows the production of wave form templates [8] which will be a crucial component in the possible future detection measured by experiments such as LIGO [1], KAGRA [2] or VIRGO [3].

The focus of this thesis, however, is on the simulation of strong gravitational waves which are acting in a highly nonlinear way and which can even collapse to a blackhole. There are two primary questions which motivate this work. The first is: *Can two popular setups of Numerical Relativity, the BSSN and the GHG setup, be successfully used to simulate the collapse of gravitational waves?* There have been several studies about the evolution and collapse of gravitational waves, which

¹Note that in the following work always the vacuum Einstein equations are considered.

Authors	Year	Data type	Slicing and gauge	References	Comments
Eppley	1978	Brill	maximal slicing/quasiisotropic	[47]	small amplitude waves only
Abrahams & Evans	1992	Teukolsky	maximal slicing/quasiisotropic	[6, 7]	reported critical behavior
Alcubierre <i>et al.</i>	2000	Brill	maximal slicing/zero shift	[11]	
Garfinkle & Duncan	2001	Brill	maximal slicing/quasiisotropic	[49]	
Santamaria	2006	Brill	multiple choices	[85]	
Rinne	2008	Brill	maximal slicing/quasiisotropic	[79]	
Sorkin	2011	Brill	family of gauge source functions	[94]	reported critical behavior

Table 1: Summary of published results on numerical simulations of nonlinear waves. This table was created by Thomas Baumgarte and is taken from [Wey2].

are summarized in table 1. However, evolving *strong* gravitational waves has always turned out to be difficult. In this work a fresh attempt is made to study the evolution and collapse of gravitational waves, using the BSSN setup including moving-puncture coordinates and finite-differences and in a second study, the GHG setup with generalized harmonic coordinates and a multi-domain pseudospectral method.

The second question is raised in the context of critical collapse [52]. In gravity, critical collapse was first reported in 1993 by Choptuik [37]. In his study he simulated numerically the collapse of scalar fields in spherical symmetry. He evolved waves of different strength, parametrized by the wave amplitude A , and made the following discoveries: for small A the waves finally dispersed and left behind flat space. For big A the waves collapsed and formed a blackhole. Studying the transition region between dispersion and collapse, he made the amazing discovery that there is a dividing critical amplitude A_\star which marks the threshold of blackhole formation. Approaching this amplitude, he found critical behavior known from other fields of physics. This means:

1. The mass M of the blackhole can be made arbitrary small and scales as

$$M \approx (A - A_\star)^\gamma. \quad (1.3)$$

2. The scaling exponent γ is universal with respect to the initial data.
3. Tuning A to the threshold of blackhole formation, a critical self-similar solution is approached. This solution is independent from the chosen family of initial data.

Shortly afterwards, similar critical behavior was found by Abrahams and Evans [6, 7], who reported critical phenomena in the collapse of axisymmetric gravitational

waves. Unfortunately it has proven difficult to reproduce these results. Since then, in all of the published work about the evolution of gravitational wave initial data, summarized in table 1, only Sorkin [94] has been able to identify critical behavior. However, his study found qualitative differences from the earlier work about gravitational wave collapse. For example, he reports that, at least for part of the parameter space, the waves collapse to form a singularity on a ring in the equatorial plane, whereas Abrahams and Evans [7] found the singularity forming at the origin. Sorkin also found a significantly larger value for the critical amplitude than in earlier studies of the same data. This topic motivates the second question for this work: *How close can the threshold of blackhole formation be approached with the setups considered in this work and what findings can be made in this regime?*

This thesis presents the work which has been carried out to answer these two questions. According to the guidelines of the Physics faculty of the University of Jena it is restricted to 100 pages. Its content is structured in the following way: Section 2 starts with presenting the two setups of Numerical Relativity which will be used within this work. Section 3 summarizes the results of the study of collapsing gravitational waves using the BSSN setup with moving puncture coordinates. Its conclusion is that, even though there are cases in which collapsing waves can be successfully evolved, this setup is not good enough to study the collapse of gravitational waves in satisfying detail. Therefore, a second approach is taken with the GHG setup. For this purpose a new 3d numerical relativity code, **bamps**, has been developed. The specific formulation of GHG and the numerical method the code implements are derived and presented in section 4. All gravitational waves which are evolved in this work are axisymmetric. Therefore section 5 discusses different aspects of axisymmetric reductions. In particular this includes the discussion of an axisymmetric apparent horizon finder, **AHloc**, which is the second code developed within this work. After having discussed all implementation details, different aspects of the **bamps** code such as convergence, accuracy and performance are carefully tested in section 6. Evolutions of single blackholes with **bamps** are subject of section 7. These are necessary components for the study of gravitational waves collapsing to blackholes which are presented in section 8. Furthermore, in this section results of Brill wave evolutions in **bamps** are compared with earlier work on this topic and an attempt is made to approach the critical amplitude for this data. Finally, in section 9 this work is concluded and future considerations are discussed.

2 Setups of Numerical Relativity

In this section two setups of Numerical Relativity, the BSSN setup and the GHG setup are presented. Each setup is a configuration consisting of a set of variables describing the spacetime, evolution equations to evolve the spacetime, a gauge choice, and a numerical method which implements the system numerically. The two setups are perhaps the most popular configurations in Numerical Relativity and will be used later in this work to study the evolution and collapse of gravitational waves. Both methods make use of the 3+1 decomposition of spacetime to recast Einstein's equations as a initial value problem [50]. Therefore the basic idea of it will be sketched here. The spacetime metric is written in the form

$$ds^2 = g_{ab}dx^a dx^b = -\alpha^2 dt^2 + \gamma_{ij}(dx^i + \beta^i dt)(dx^j + \beta^j dt), \quad (2.1)$$

where α is the lapse function, β^i the shift vector, and γ_{ij} the spatial metric. Einstein's equations split into a set of constraint equations, the Hamiltonian and the momentum constraint

$$R + K^2 - K_{ij}K^{ij} = 0, \quad (2.2)$$

$$D_j K^{ij} - D^i K = 0. \quad (2.3)$$

and evolution equations

$$\begin{aligned} \partial_t \gamma_{ij} &= -2\alpha K_{ij} + \mathcal{L}_\beta \gamma_{ij}, \\ \partial_t K_{ij} &= \alpha(R_{ij} - 2K_{ik}K^k_j + KK_{ij}) + \mathcal{L}_\beta K_{ij}. \end{aligned} \quad (2.4)$$

Here, the Ricci tensor R_{ij} , its trace R and the covariant derivative D_i are associated with the spatial metric γ_{ij} . K_{ij} is the extrinsic curvature and $K = \gamma^{ij}K_{ij}$ is its trace. These equations are often referred to as the ADM equations [17]. In numerical simulations typically a *free evolution* scheme is applied. This means that an initial slice of constraint satisfying data is evolved forward in time using the evolution equations. The constraint equations are only used to monitor the error during the evolution.

2.1 The BSSN setup

The BSSN setup consists of the BSSN evolution equations [20], the moving-puncture gauge [34] and the finite-differences method [75]. It has been used in the majority of the relevant simulations in Numerical Relativity and played an important role in astrophysical relevant simulations of binary blackholes [34] and neutron stars [98], as well as in collapse scenarios of stars [100]. The popularity of this setup is predominantly based on two facts. Firstly, it recasts Einstein's equations as a well-posed evolution system and secondly, the moving-puncture coordinates allow to simulate blackholes without the need to excise the blackhole inside its horizon from the numerical domain.

BSSN evolution equations

In the BSSN formulation the spatial metric γ_{ij} is conformally decomposed

$$\bar{\gamma}_{ij} = e^{-4\phi} \gamma_{ij}, \quad (2.5)$$

and the conformal metric $\bar{\gamma}_{ij}$ is constrained to have a unit determinant. The extrinsic curvature is split into its trace-free part and its trace

$$K_{ij} = e^{4\phi} \tilde{A}_{ij} + \frac{1}{3} \gamma_{ij} K. \quad (2.6)$$

Furthermore, an auxiliary variable, the contracted conformal Christoffel symbol

$$\bar{\Gamma}^i = \bar{\gamma}^{ij} \bar{\gamma}^{kl} \partial_l \bar{\gamma}_{jk}, \quad (2.7)$$

is introduced. The evolution of this set of variables is given by the BSSN equations

$$\begin{aligned} \partial_t \bar{\gamma}_{ij} &= -2\alpha \tilde{A}_{ij} + \mathcal{L}_\beta \bar{\gamma}_{ij}, \\ \partial_t \phi &= -\frac{1}{6} \alpha K + \mathcal{L}_\beta \phi, \\ \partial_t \tilde{A}_{ij} &= e^{-4\phi} \left[-D_i D_j \alpha + \alpha (\bar{R}_{ij} + R_{ij}^\phi) \right]^{\text{TF}} + \alpha (K \tilde{A}_{ij} - 2\tilde{A}_{ik} \tilde{A}_j^k) + \mathcal{L}_\beta \tilde{A}_{ij}, \\ \partial_t K &= -D^i D_i \alpha + \alpha (\tilde{A}_{ij} \tilde{A}^{ij} + \frac{1}{3} K^2) + \mathcal{L}_\beta K, \\ \partial_t \bar{\Gamma}^i &= -2\alpha \left(\frac{2}{3} \bar{\gamma}^{ij} D_j K - 6\tilde{A}^{ij} D_j \phi - \bar{\Gamma}_{jk}^i \tilde{A}^{jk} \right) - 2\tilde{A}^{ij} D_j \alpha + \bar{\gamma}^{jk} \partial_j \partial_k \beta^i \\ &\quad - \frac{4}{3} (\bar{\Gamma}^i - \bar{\gamma}^{jk} \bar{\Gamma}_{jk}^i) \partial_l \beta_l + \frac{1}{3} \bar{\gamma}^{ij} \partial_k \partial_j \beta^j - \bar{\Gamma}^j \partial_j \beta^i + \frac{2}{3} \bar{\Gamma}^i \partial_k \beta^k + \beta^j \partial_j \bar{\Gamma}^i. \end{aligned} \quad (2.8)$$

Here, D_i is the covariant derivative compatible with γ_{ij} . The label TF denotes the trace-free part of the expression it is attached to. Quantities with a bar, such as \bar{R}_{ij} and $\bar{\Gamma}_{jk}^i$, are associated with the conformal metric and it is

$$R_{ij}^\phi = -2\bar{D}_i\bar{D}_j - 2\bar{\gamma}_{ij}\bar{D}^l\bar{D}_l\phi + 4(\bar{D}_i\phi)(\bar{D}_j\phi) - 4\bar{\gamma}_{ij}(\bar{D}^l\phi)(\bar{D}_l\phi). \quad (2.9)$$

The definition of the Lie derivatives acting on tensor densities can be found for example in [10]. This system of partial differential equations is a first order in time and second order in space-system. Still to be determined is the choice of the gauge variables α and β^i .

Moving-puncture coordinates

The standard gauge choice used in combination with the BSSN evolution equation is the puncture gauge. It consists of the *1+log slicing* condition [25]

$$(\partial_t - \beta^j\partial_j)\alpha = -2\alpha K, \quad (2.10)$$

and the *Gamma-driver shift* condition [14, 107]

$$(\partial_t - \beta^j\partial_j)\beta^i = \mu_S\bar{\Gamma}^i - \eta\beta^i, \quad (2.11)$$

with freely specifiable scalars μ_S and η . This gauge together with the BSSN equations are proven to be a strongly hyperbolic initial value problem and are therefore suitable for the treatment with numerical methods [53, 66, 86].

Finite-differences

Although the BSSN formulation has been evolved with different type of numerical methods [104, 105], the most common approach for solving the BSSN system numerically is using finite-differences in combination with the *method of lines*. The basic idea of this method is to treat the spatial and the time discretization separately. First all evolution fields f are discretized on a spatial grid at N grid points x_α ,

$$f(x) \longrightarrow f(x_\alpha) \equiv f_\alpha, \quad \alpha = 0, \dots, N-1. \quad (2.12)$$

The spatial derivatives are approximated on this grid using finite difference stencils. For example, second order accurate finite difference stencils in 1d are given by

$$\begin{aligned}\partial_x f &\longrightarrow (\partial_x f)_\alpha = \frac{f_{\alpha+1} - f_{\alpha-1}}{2\Delta x} + \mathcal{O}(\Delta x^2), \\ \partial_x^2 f &\longrightarrow (\partial_x^2 f)_\alpha = \frac{f_{\alpha+1} - 2f_\alpha + f_{\alpha-1}}{(\Delta x)^2} + \mathcal{O}(\Delta x^2).\end{aligned}\tag{2.13}$$

Second, after the spatial discretization, a standard ODE integrator, such as a Runge-Kutta-scheme, is applied to evolve the equations forward in time

$$f^{n+1} = f^n + \Delta t \sum_i^s c_i k_i.\tag{2.14}$$

Here c_i depends on the specific Runge-Kutta-scheme and k_i is determined by evaluating the right hand side of the evolution equations at appropriate in-between times.

2.2 The GHG setup

The generalized harmonic gauge (GHG) system is based on the idea of using harmonic coordinates in which Einstein's equations are manifestly hyperbolic. It was first introduced in [48] and played a major role in the binary blackhole evolutions of [76–78]. The GHG setup which will be presented in this section is based on a fully first order evolution system and is numerically solved using a pseudospectral method. It was proposed by [70] and has been successfully implemented with the SpEC code [4].

Fully first order GHG evolution equations

Generalized harmonic coordinates x_a evolve according to the inhomogeneous wave equation

$$\nabla^b \nabla_b x_a = H_a(x, g) = -\Gamma_a,\tag{2.15}$$

where Γ_a is the contracted Christoffel symbol and H_a is a freely specifiable gauge source function that only depends on the coordinates and the metric but not on derivatives of the metric. In these coordinates the principal part of the Einstein's

equations is the wave operator

$$g^{cd}\partial_c\partial_d g_{ab} = -2\nabla_{(a}H_{b)} + 2g^{cd}g^{ef}(\partial_e g_{ac}\partial_f g_{bd} - \Gamma_{ace}\Gamma_{bdf}). \quad (2.16)$$

Introducing the variables

$$\Pi_{ab} = -n^c\partial_c g_{ab}, \quad \Phi_{iab} = \partial_i g_{ab}, \quad (2.17)$$

the system can be reduced to be first order in time and space. In [70] the following set of evolution equations was proposed

$$\begin{aligned} \partial_t g_{ab} &= \beta^i\partial_i g_{ab} - \alpha\Pi_{ab} + \gamma_1\beta^i C_{iab}, \\ \partial_t \Phi_{iab} &= \beta^j\partial_j \Phi_{iab} - \alpha\partial_i \Pi_{ab} + \gamma_2\alpha C_{iab} + \frac{1}{2}\alpha n^c n^d \Phi_{icd}\Pi_{ab} + \alpha\gamma^{jk}n^c \Phi_{ijc}\Phi_{kab}, \\ \partial_t \Pi_{ab} &= \beta^i\partial_i \Pi_{ab} - \alpha\gamma^{ij}\partial_i \Phi_{jab} + \gamma_1\gamma_2\beta^i C_{iab} - \frac{1}{2}\alpha n^c n^d \Pi_{cd}\Pi_{ab} - \alpha n^c \gamma^{ij}\Pi_{ci}\Phi_{jab} \\ &\quad + 2\alpha g^{cd}(\gamma^{ij}\Phi_{ica}\Phi_{jdb} - \Pi_{ca}\Pi_{db} - g^{ef}\Gamma_{ace}\Gamma_{bdf}) + \alpha\gamma_0[2\delta^c_{(a}n_{b)} - g_{ab}n^c]C_c \\ &\quad - 2\alpha\nabla_{(a}H_{b)}. \end{aligned} \quad (2.18)$$

This system of partial differential equations is symmetric hyperbolic. It includes the constraints

$$C_a = \Gamma_a + H_a = 0, \quad C_{iab} = \partial_i g_{ab} - \Phi_{iab} = 0, \quad (2.19)$$

and constraint damping parameters γ_0 , γ_1 , and γ_2 . The constraint subsystem will be studied in more detail in section 4. The system also makes use of several $3+1$ quantities such as the inverse of the spatial metric γ^{ij} , the lapse α and the shift β^i and the normal vector $n_a = -\alpha\delta_a^0$.

Pseudospectral method

The idea of the pseudospectral method [51, 61, 68] is to expand all evolution fields f in space into a finite series of suitable basis functions T_l at N collocation points x_α

$$f_\alpha \equiv f(x_\alpha) = \sum_{l=0}^{N-1} c_l T_l(x_\alpha). \quad (2.20)$$

For simplicity it is assumed here that $x \in [-1, 1]$. Otherwise an appropriate coordinate transformation has to be applied. In the context of the GHG setup Gauss-

Lobatto collocation points,

$$x_\alpha = -\cos\left(\frac{\pi}{N_x - 1}\alpha\right), \quad \alpha = 0, \dots, N - 1, \quad (2.21)$$

in combination with Chebyshev polynomials,

$$T_l(x) = \cos\left[l \arccos(x)\right], \quad (2.22)$$

are used. The first derivatives of the fields are computed at the collocation points by means of a matrix multiplication,

$$(\partial_x f)_\alpha = \sum_{l=0}^{N-1} D_{\alpha l} f_l, \quad (2.23)$$

with the Gauss-Lobatto derivative matrix

$$D_{\alpha\beta} = \begin{cases} -\frac{2(N-1)^2+1}{6} & \alpha = \beta = 0 \\ \frac{q_\alpha (-1)^{\alpha+\beta}}{q_\beta x_\alpha - x_\beta} & \alpha \neq \beta \\ \frac{-x_\beta}{2(1-x_\beta^2)} & \alpha = \beta = 1, \dots, N - 2 \\ \frac{2(N-1)^2+1}{6} & \alpha = \beta = N - 1 \end{cases} \quad (2.24)$$

Here it is $q_\alpha = 2$ at boundary points and $q_\alpha = 1$ elsewhere. For the time integration, again a standard ODE integrator can be used to evolve the fields forward in time. The pseudospectral method is known to provide fast convergence of the numerical to the continuum solution, in the case of smooth solutions to the partial differential equation. This convergence behavior is often called *exponential convergence*. In the case of the Einstein equations, solutions in vacuum are indeed smooth. However, spectral methods are very sensitive regarding errors on the numerical domain, which makes their successful implementation more tricky compared to the robust finite-difference method.

3 Evolution of collapsing gravitational waves with the BSSN setup

In this section the evolution of gravitational waves with the BSSN setup is studied. The primary question is how well the moving-puncture gauge allows one to follow the collapse of gravitational waves to a blackhole. In the context of stellar-collapse, previous work by [18] and [95, 100] found that moving-puncture coordinates can lead to stable evolutions, with the newly-formed blackhole expressed in a trumpet geometry [56]. However, in the context of collapsing gravitational waves, it is not obvious that the moving-puncture coordinate also lead to successful simulations. The results of this section have been published in [Wey2].

The BAM code: All simulations of this section have been carried out with the BAM code, which is described in [28, 29, 64, 99]. The evolutions were performed with an explicit 4th-order Runge-Kutta method and 4th-order finite-differences for the spatial derivatives. Mesh refinement is provided by a hierarchy of cell-centered nested Cartesian grids and Berger-Oliger time stepping. Metric variables are interpolated in space by means of 6th-order Lagrangian polynomials. Interpolation in Berger-Oliger time stepping is performed at 2nd order.

3.1 Evolution of Brill waves

A Brill wave is an axisymmetric gravitational wave solution of Einstein's equations. They are constructed by writing the spatial metric in a conformal form

$$dl^2 = \gamma_{ij}dx^i dx^j = \psi^4 [e^{2q}(d\rho^2 + dz^2) + \rho^2 d\phi^2], \quad (3.1)$$

where ρ , z and ϕ are cylindrical coordinates, ψ is the conformal factor, and $q = q(r, \theta)$ is an arbitrary axisymmetric seed function. Assuming a moment of time-symmetry, the extrinsic curvature vanishes and the momentum constraint (2.3) is solved identically. The Hamilton constraint (2.2) reduces to a linear elliptic equation for the conformal factor ψ ,

$$\nabla^2 \psi = -\frac{\psi}{4} \left(\frac{\partial^2 q}{\partial \rho^2} + \frac{\partial^2 q}{\partial z^2} \right), \quad (3.2)$$

with ∇^2 being the flat, three-dimensional Laplace operator. In the following the seed function q is taken to be

$$q(\rho, z) = A \left[\frac{\rho}{\sigma} \right]^2 e^{-[(\rho-\rho_0)^2 - z^2]/\sigma^2}. \quad (3.3)$$

Here A is a measure of the resulting wave amplitude, σ of the wavelength, and ρ_0 of the center of the initial wave. Throughout it is $\sigma = 1$, which determines the units of all dimensional results. For a given set of parameters equation (3.2) is solved for ψ using a spectral elliptic solver, described in [44]. Initial data for Brill waves evolution with BAM is then set up setting the extrinsic curvature to zero and setting up the spatial metric according to (3.1) using the numerical solution for ψ , together with the associated seed function q . The following simulations focus on “central” Brill waves with $\rho_0 = 0$ for different choices of amplitude A . As a measurement for the strength of curvature typically the Kretschmann scalar,

$$I = C_{abcd}C^{abcd}, \quad (3.4)$$

where C_{abcd} is the Weyl tensor, is stated.

Evolution of $A = 1.0$ centered Brill wave: Brill waves with small amplitude A represent linear perturbations of flat space. They will propagate to spatial infinity and leave behind flat space. As an example, an evolution of a centered wave with $A = 1$ is studied. In this simulation the maximum of the curvature in spacetime is reached at the center, with the Kretschmann scalar reaching the value $I \approx 216$. For this run the parameters of the puncture gauge are set to be $\mu_S = 1$ and $\eta = 3 \approx 1/(10M)$. The evolution of the lapse function decreases initially and reaches its minimum at around the same time as the curvature of the peaks. Afterwards it quickly moves back towards unity. In Fig. 2 this behavior with that for other amplitudes is shown. The initial pulse in the Kretschmann scalar disperses away and leaves behind $I = 0$, indicating that the space is flat.

Evolution of $A = 2.5$ centered Brill wave: For larger, but still subcritical A , the waves will interact nonlinearly before dispersing, but ultimately they still leave behind flat space. Again, the Kretschmann scalar for centered Brill data with $A = 2.5$ takes its maximum at the origin, but now with value of ≈ 2320 . The gauge parameter for this data is $\mu_S = 1$ and $\eta = 2 \approx 2/(5M)$. The lapse at the origin again decreases at early times, this time to smaller values than for $A = 1$, and then

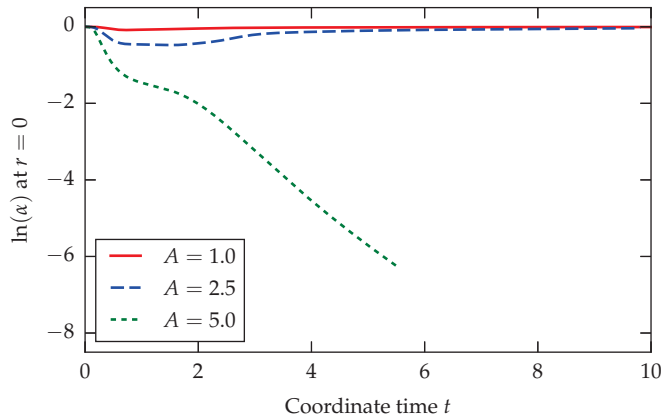


Figure 2: The central value of the lapse as a function of time for differently strongly centered Brill waves. The waves are evolved using the puncture gauge conditions. For weak-field initial data with $A = 1$, the wave disperses to spatial infinity and leaves behind flat space, as expected. For larger values of A , however, the simulations lead to discontinuities in the metric functions, which spoil the further evolution of the wave.

returns to unity. The Kretschmann scalar also disperses to infinity, as before.

Evolution of $A = 5.0$ centered Brill wave: For simulations of amplitudes which are larger than some critical A_* it is expected that the Brill waves will collapse to a blackhole. However, for these amplitudes the carried out BAM simulations are not successful. This means that it is not possible to track the formation of an apparent horizon as it settles down to a Schwarzschild blackhole. More detailed results for $A = 5$ are shown in Fig. 3, where profiles of the lapse function α , the metric component γ_{xx} and trace K are plotted at different instants of time. The lapse collapses in the central region and develops a minimum along a ring of radius $r \approx 2.0$ in the equatorial plane in a simulation with $\eta = 11.4 \approx 8/M$. The metric simultaneously develops an increasingly large gradient across this ring, which ultimately turns into a discontinuity if in the gamma-driver condition (2.11) $\eta = 0$ is used. Associated with this gradient is a large numerical error which can be seen, for example, in the violation of the constraints. A pulse in the lapse then approaches the origin, so that the region with nearly-vanishing lapse becomes smaller. As this happens the trace of the extrinsic curvature at the incoming lapse pulse becomes large, negative and sharp, ending in a numerical failure that looks like a coordinate singularity. Similar behavior has been observed with the $1 + \log$ gauge elsewhere, for example in [15].

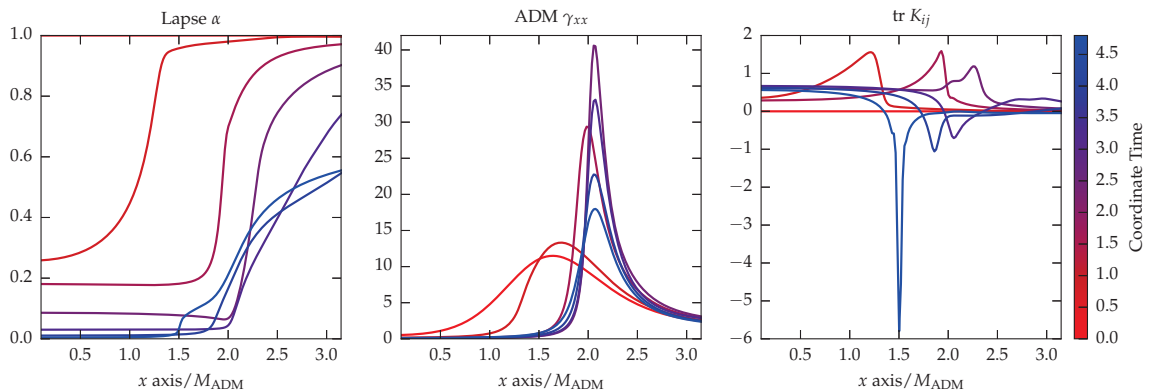


Figure 3: Snapshots of the lapse function α (left panel), the ADM metric component γ_{xx} (center panel) and the trace of the extrinsic curvature $\text{tr}K_{ij}$ at different instants of time, for $A = 5$. All quantities are shown along the x axis, with time indicated by hot-to-cold colors. The lapse develops a minimum on a ring of radius $r \approx 2.0$, which then travels towards the origin. The spatial metric develops a large gradient around the same ring. A sharp feature at radius $r \approx 1.5$ appears in the lapse, and K diverges around the same place. The latter feature is not visible in the metric.

Furthermore, this failure can be reproduced in the spherical code used to develop the Z4c formulation [22, 35, 64, 84, Wey1] by evolving flat space with a perturbed initial lapse with precisely studying evolutions of the gauge of the Brill wave evolutions. This feature causes the numerical approximation to fail at around $t = 5.5$. Curiously here, in preliminary tests, it was found that mesh-refinement can cause problems. Often coarser grids are used to push the outer boundary far away inexpensively. But it turns out that the solutions being constructed are so extreme that if the grids are too coarse then they will fail during the single Runge-Kutta time-step needed before the data from the finer boxes can be used to overwrite coarse grid data.

Summary: The simulations considered in this section showed that moving-puncture coordinates are not suitable for the evolution of the Brill waves. For several other coordinate choices, including maximal slicing for the lapse, as well as quasi-isotropic or zero shift, it also appears to be difficult to obtain sufficiently reliable simulations that allow the study of critical phenomena in the vicinity of the critical amplitude. However, other studies proved that moving-puncture coordinates can be used in other collapse scenarios. So rather than altering the gauge choice different initial gravitational wave data will be chosen in the following section.

3.2 Comparing Brill with Teukolsky wave evolutions

In [Wey2] it was found by Thomas Baumgarte, Pedro Montero and Ewald Müller that with a similar type of gravitational wave initial data, Teukolsky waves, it is possible to evolve the collapse of the waves in moving-puncture coordinates. At least for amplitudes that are not too close to the critical point, they have been able to detect the formation of apparent horizons and evolve the blackhole spacetime until it settled down to spherical symmetry. The simulations of section 3.1 showed that this was not possible with Brill wave data. While it is difficult to pin-point what exactly creates this difference in behavior, in this section some possible reasons on these differences are discussed. An obvious set of questions present themselves. The Brill data was centered at the origin, whereas the Teukolsky data was not. Could this be the cause of the difference? Are the two types of data somehow geometrically different? If so, would this difference be maintained in time evolution, and can the Brill wave data be modified to make it more amenable to numerical evolution with the moving-puncture gauge?

Off-center Brill wave evolutions

Small data: Two sets of weak, off-center Brill wave initial data with offset $\rho_0 = 4$ in (3.3) are evolved. Specifically, the waves have the amplitudes $A = 0.053$ and $A = 0.0815$, which have ADM masses ≈ 0.59 and ≈ 1.4 respectively. For the weaker $A = 0.053$ data the shift damping is set to $\eta \approx 1/M$, while for the $A = 0.0815$ data $\eta \approx 2/M$ is chosen. As for the earlier weak, center Brill data, both waves disperse after a brief interaction around the origin. For the weaker data, the Kretschmann scalar takes a maximum value ≈ 48 at the origin, while for the stronger data the maximum is ≈ 200 , again at the origin.

Large data: Now the amplitude is increased to $A = 0.12$, which makes the ADM mass ≈ 3.15 . The shift damping is set to $\eta = 8/M$. As in the “small data” tests, the lapse initially decreases most rapidly around the peak of the seed function in the xy -plane. It then decreases to zero near the origin. Then an incoming gauge wave travels along the z -axis towards the origin. Since the speed of the gauge wave is $\sim \sqrt{2\alpha}$, and travels from a region with $\alpha \sim 1$ to one with $\alpha \sim 0$, there is a rapid blueshift effect; the solution becomes badly resolved. At some point in time, around the interface of these two regions, the trace of the extrinsic curvature becomes negative, which leads to an increase in the lapse (see eq. (2.10)). Ultimately, this results in a coordinate singularity causing the code to fail at $t \approx 16$. There is a

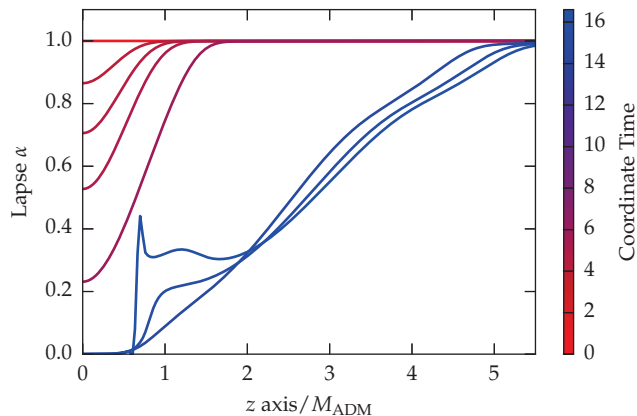


Figure 4: Profiles of the lapse at different instances of time along the z axis for a off-centered Brill wave with $A = 0.12$ and $\rho_0 = 4.0$. Initially the lapse collapses at the center. At late times of the evolution, a gauge pulse is traveling in and gets blue-shifted. At the interface between the collapsed lapse and the gauge pulse, a coordinate singularity appears. This leads to a failure of the simulation.

remarkable similarity between the lapse profile obtained in this simulations, shown in Fig. 4, and that shown in Fig. 2 of [15] where such coordinate singularities were studied in evolutions of flat-space. This leads to the conclusion that for sufficiently large amplitudes, moving-puncture coordinates fail even for off-centered Brill wave initial data.

Axisymmetric twist-free, time symmetric data

Harmonic spatial coordinates: As the different behavior of Brill and Teukolsky data is not caused by the different offset, now the difference in the geometry of Brill and Teukolsky waves is studied. In cylindrical coordinates, the conformally related metric for Brill wave initial data is given by

$$\bar{\gamma}_{ij} = \begin{pmatrix} e^q & 0 & 0 \\ 0 & e^q & 0 \\ 0 & 0 & \rho^2 \end{pmatrix} \quad (3.5)$$

(see eq. (3.1)), whereas for Teukolsky waves the conformally related metric takes the form

$$\bar{\gamma}_{ij} = \begin{pmatrix} \bar{\gamma}_{\rho\rho} & \bar{\gamma}_{\rho z} & 0 \\ \bar{\gamma}_{\rho z} & \bar{\gamma}_{zz} & 0 \\ 0 & 0 & \bar{\gamma}_{\phi\phi} \end{pmatrix}. \quad (3.6)$$

Evidently, the two data sets are given in different coordinate systems, and a meaningful comparison can only be made once they have been expressed in the same coordinates. However, any axisymmetric, twist-free metric can be brought into the form

$$\bar{\gamma}_{ij} = \begin{pmatrix} e^q & 0 & 0 \\ 0 & e^q & 0 \\ 0 & 0 & \rho^2 V \end{pmatrix}, \quad (3.7)$$

in some coordinate system (ϱ, ξ, ϕ) . Broadly speaking, this is possible because the two-metric in the ρ - z subspace can always be brought into an explicitly conformally flat form [108, Ch. 3, Ex. 2].

Geometrically oblate and prolate initial data: Any spherically symmetric metric can be brought into the form (3.7) with $V = e^q$. For the gravitational wave initial data used in this work, which is not spherically symmetric, V will, in general, be different from e^q . Evidently, deviations of V from e^q can be produced in two ways: either $V > e^q$ or $V < e^q$. In the following data with $V > e^q$ is called *geometrically oblate* and data with $V < e^q$ *geometrically prolate*. Here, the word ‘geometrically’ is used to distinguish the terminology from that normally used with Brill waves, where the word oblate or prolate applies to the seed function. Clearly, both V and e^q are functions of the coordinates, so that data may be geometrically oblate in some region and prolate in another. Also it is important to notice that this characterization is only applied to the initial data; it is not evident whether or how this characterization is maintained during a time evolution, even if the data is globally geometrically oblate or prolate initially. The characterization as geometrically oblate or prolate may nevertheless be a useful distinction between the geometries of Brill and Teukolsky data evolved earlier. An example of initial data of a certain character which is maintained is given in [38].

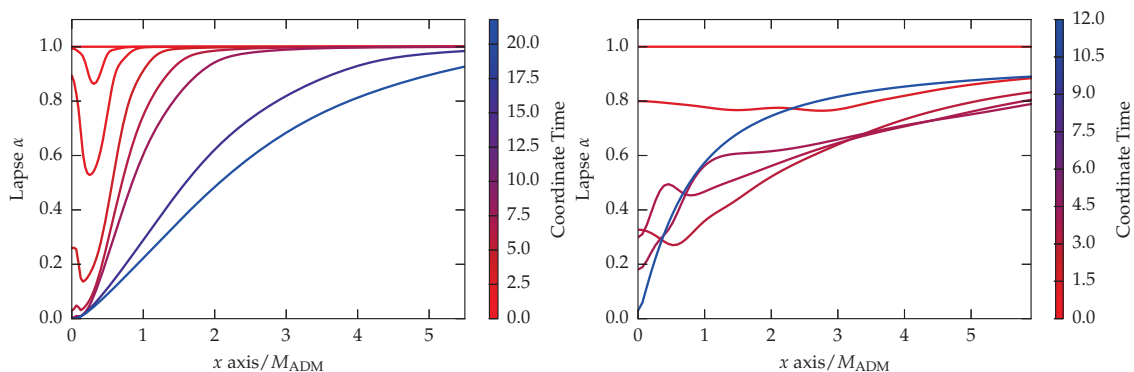


Figure 5: On the left profiles of the lapse at different instances of time for a centered Brill wave with $A = -5$ are plotted. These profiles should be compared with (a) those of a positive-amplitude Brill wave in the top panel in Fig. 3, and (b) those for a Teukolsky wave which are plotted on the right (Figure taken from [Wey2]).

Geometric oblateness of Brill and Teukolsky data: For the Brill wave initial data of Section 5.3 it is $V = 1$; moreover the positive A in the seed function (3.3) results in $e^q \geq 1$. This means that the Brill wave initial data of Section 5.3 is geometrically prolate everywhere except on the z -axis. For Teukolsky waves the classification is less obvious, because it requires an additional coordinate transformation. Interestingly, however, Fig. 3 in [7] shows that the geometry close to the center is geometrically oblate. (The quantity e^η used by [7] is a measure of the ratio e^q/V ; the fact that their η is negative in a region around the origin implies that the geometry is oblate there.) This observation could point to a fundamental difference in the geometries of $A > 0$ Brill and Teukolsky waves.

Discussion: These arguments are neither rigorous nor complete, but they lead to an immediate suggestion: if it were true that geometrically oblate data is better behaved in dynamical evolutions than prolate data – for example in the sense that it forms a singularity at the center rather than on a ring – then it would be of interest to produce geometrically oblate Brill wave initial data. Such data will be considered next.

3.3 Brill waves with $A < 0$

In this section the evolution of geometrically oblate Brill wave data is studied. Such data can be produced in exactly the same way as the prolate data in Section 5.3, by adopting “negative amplitudes” $A < 0$ in the seed function (3.3).

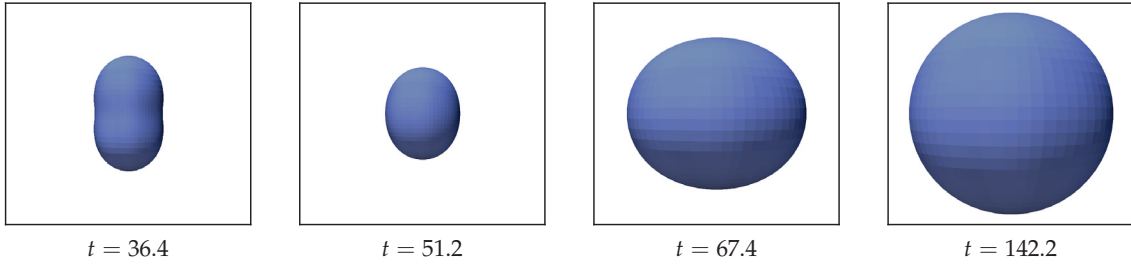


Figure 6: Snap-shots of the apparent horizon for supercritical off-center geometrically oblate Brill waves. The apparent horizon is first discovered at $t = 36.4$ and has a peanut-like shape, where in the plots the z -axis runs vertically. The subsequent frames show the oscillations of the horizon, which jumps at $t \approx 65$.

Centered geometrically oblate Brill waves: Three sets of initial data with $\rho_0 = 0$ and $A < 0$, namely $A = -1$, -2.5 and $A = -5$ are evolved, with ADM masses of approximately 0.61, 1.37 and 3.15 respectively. As in the geometrically prolate case, the first two data sets just allow the Kretschmann scalar to propagate away, taking maximal values of about 56 and 1072 appearing at the origin. For the stronger field evolution the numerics again eventually fail, although now at around $t = 22.5$. On the left of Fig. 5 profiles of the lapse at different instances of time for such a Brill wave with $A = -5$ are shown. Interestingly, these profiles are qualitatively different from those for the geometrically prolate, positive-amplitude Brill waves shown in the top panel of Fig. 3. While for geometrically prolate Brill waves the lapse always takes a minimum at finite radius, which coincides with the development of increasingly large gradients in the spatial metric, for $A < 0$ Brill waves the lapse ultimately reaches a minimum at the center. This is the same behavior that was found in the Teukolsky waves, which is shown in Fig. 5 on the right. In these simulations it was possible to follow the collapse of geometrically oblate Brill waves past blackhole formation, and in contrast to positive-amplitude Brill waves also apparent horizons have been located. However, at least with the chosen setup, the BAM apparent horizon finder did not give reliable results. At late times, steep gradients in the metric functions again appeared, but this time well inside the horizon, close to the center. Ultimately, these gradients spoil further numerical evolution.

Off-center geometrically oblate Brill waves: Again three sets of initial data $A = -0.044$, -0.061 and $A = -0.08125$, all with $\rho_0 = 4$, are evolved. The ADM masses of these spacetimes are approximately 0.61, 1.36 and 3.15 with peak values of the Kretschmann scalar initially around 64, 108, and 88 respectively. It is interesting that the “larger” initial data does not have the largest initial Kretschmann, but the

evolution leaves no doubt that the $A = -0.08125$ data is indeed the stronger one. As in the previous results the two weaker data sets leave behind $I = 0$, with greater oscillations in the Kretschmann scalar in the $A = -0.061$ case. The maximum of the Kretschmann scalar in the evolution of the $A = -0.044$ is around 19 and occurs at the origin at $t \simeq 7.4$. Likewise with the $A = -0.061$ data, the maximum occurs at the origin, with a value around 373 at $t \simeq 12$. In both the $A = -0.044$ and the $A = -0.061$ evolutions the Kretschmann scalar propagates away predominantly along the symmetry axis. The strongest data $A = -0.08125$ evolves in the BAM code until $t = 150$. It collapses to form a blackhole similarly to the Teukolsky data presented in [Wey2]. An apparent horizon was first discovered at $t = 36.4$. In Fig. 6 some snapshots of the evolution of the horizon are plotted. The apparent horizon mass eventually settles down to $M = 1.73$. So by choosing the parameters in the Brill wave data carefully, evolutions comparable to those with Teukolsky initial data, presented in [Wey2], are possible.

4 A pseudospectral method for gravitational wave collapse

The previous section led to the conclusion that with the BSSN setup the collapse of Brill waves cannot be studied in a satisfying manner. The two main difficulties were the formation of coordinate singularities and a lack of accuracy. Therefore the focus is now shifted to the GHG setup, which uses different coordinates and provides the more accurate pseudospectral method. In order to study the collapse of Brill waves within this work, a new 3d numerical relativity code, **bamps**, was developed [Wey3]. It is based on the idea of the SpEC code but with different improvements towards the evolution of strong gravitational waves in mind. This section gives several implementation details of **bamps**. The focus is first on the specific GHG formulation which is implemented in the code. Special care is taken at the formulation of constraint preserving boundary conditions which work well in the case of close outer boundaries. Later in this section the actual implementation details are discussed. This includes the grid setup, the numerical method and the patching boundary treatment.

4.1 Formulation setup

4.1.1 GHG evolution equations, constraints and boundary conditions

The evolution system: The **bamps** code implements the fully first order GHG equations of motion as

$$\begin{aligned}
\partial_t g_{ab} &= \beta^i \partial_i g_{ab} - \alpha \Pi_{ab} + \gamma_1 \beta^i C_{iab}, \\
\partial_t \Phi_{iab} &= \beta^j \partial_j \Phi_{iab} - \alpha \partial_i \Pi_{ab} + \gamma_2 \alpha C_{iab} + \frac{1}{2} \alpha n^c n^d \Phi_{icd} \Pi_{ab} + \alpha \gamma^{jk} n^c \Phi_{ijc} \Phi_{kab}, \\
\partial_t \Pi_{ab} &= \beta^i \partial_i \Pi_{ab} - \alpha \gamma^{ij} \partial_i \Phi_{jab} + \gamma_1 \gamma_2 \beta^i C_{iab} - \frac{1}{2} \alpha n^c n^d \Pi_{cd} \Pi_{ab} - \alpha n^c \gamma^{ij} \Pi_{ci} \Phi_{jab} \\
&\quad + 2\alpha g^{cd} (\gamma^{ij} \Phi_{ica} \Phi_{jdb} - \Pi_{ca} \Pi_{db} - g^{ef} \Gamma_{ace} \Gamma_{bdf}) + \alpha \gamma_0 [2\delta^c_{(a} n_{b)} - g_{ab} n^c] C_c \\
&\quad - 2\alpha (\nabla_{(a} H_{b)} + \gamma_4 \Gamma^c_{ab} C_c - \frac{1}{2} \gamma_5 g_{ab} \Gamma^c C_c). \tag{4.1}
\end{aligned}$$

The formulation here agrees with that of [70], which was also presented in section 2.2, except for the inclusion of the γ_4 and γ_5 parameters. These control whether or not the constraint addition made in the construction of the formulation is done either with the covariant or the partial derivative, or some combination. The latter choice has the effect of simplifying the constraint subsystem. In the following work they

are either set to vanish, or chosen to be $\gamma_4 = \gamma_5 = 1/2$. The terms involving γ_0 are included so as to damp away high-frequency constraint violations [54]. In matrix notation this system can be written as

$$\partial_t u^\mu = A^{k\mu}{}_\nu \partial_k u^\nu + S^\mu, \quad (4.2)$$

with

$$u^\mu = \begin{pmatrix} g_{ab} \\ \Pi_{ab} \\ \Phi_{iab} \end{pmatrix}, \quad A^{k\mu}{}_\nu = \begin{pmatrix} (1 + \gamma_1)\beta^k & 0 & 0 \\ \gamma_1\gamma_2\beta^k & \beta^k & -\alpha\gamma^{ik} \\ \gamma_2\alpha\delta_i^k & -\alpha\delta_i^k & \beta^k \end{pmatrix}, \quad (4.3)$$

and S^μ containing all source terms of the right hand side. This compact notation will be used in the following calculations of this work. In the first order reduction the Christoffel symbols are shorthands for

$$\Gamma_{abc} = \gamma^i{}_{(b} \Phi_{i|c)a} - \frac{1}{2}\gamma^i{}_a \Phi_{ibc} + n_{(b} \Pi_{c)a} - \frac{1}{2}n_a \Pi_{bc}, \quad (4.4)$$

As described in section 2.2, the system is symmetric hyperbolic, having the same principal part as a particular first order reduction of the wave equation. Its characteristic variables are given by

$$u_{ab}^{\hat{0}} = g_{ab}, \quad u_{ab}^{\hat{\pm}} = \Pi_{ab} \mp s^i \Phi_{iab} - \gamma_2 g_{ab}, \quad u_{Aab}^{\hat{\beta}} = q^i{}_A \Phi_{iab}, \quad (4.5)$$

with the projection operator $q^j{}_i = \delta^j{}_i - s^j s_i$, and speeds

$$v^{\hat{0}} = (1 + \gamma_1)\beta^s, \quad v^{\hat{\pm}} = \beta^s \pm \alpha, \quad v^{\hat{\beta}} = \beta^s, \quad (4.6)$$

respectively. A convenient way to transform from the evolution variables to the characteristic variables is to write $u^{\hat{\alpha}} = T^{-1\alpha}{}_\beta u^\beta$, where again the matrix notation has been used, in which the characteristic variables are combined as

$$u^{\hat{\alpha}} = \begin{pmatrix} u_{ab}^{\hat{0}} \\ u_{ab}^{\hat{\pm}} \\ u_{Aab}^{\hat{\beta}} \end{pmatrix}, \quad (4.7)$$

and the similarity matrix is

$$T^{-1\hat{\alpha}}_{\mu} = \begin{pmatrix} 1 & 0 & 0 \\ -\gamma_2 & 1 & -s^i \\ -\gamma_2 & 1 & s^i \\ 0 & 0 & q^i_j \end{pmatrix}, \quad (4.8)$$

It has the left inverse

$$T^{\mu}_{\hat{\alpha}} = \begin{pmatrix} 1 & 0 & 0 & 0 \\ \gamma_2 & 1/2 & 1/2 & 0 \\ 0 & -s_i/2 & s_i/2 & \delta^i_j \end{pmatrix}, \quad (4.9)$$

but note that $T^{-1\hat{\alpha}}_{\mu} T^{\mu}_{\hat{\beta}} \neq \delta^{\hat{\alpha}}_{\hat{\beta}}$. The strength of this particular representation in practical terms is the avoidance of special cases in the numerical implementation, like for example $s^x = 0$, in the characteristic decomposition.

Gauge source functions: The gauge source functions H_a are chosen to be

$$H_a = \eta_L \log \left(\frac{\gamma^{p/2}}{\alpha} \right) n_a - \frac{\eta_S}{\alpha^2} \gamma_{ai} \beta^i. \quad (4.10)$$

This convention differs from that of both [96] and [94] in a trivial normalization of the spatial part with respect to the lapse function. In terms of the lapse and the shift this gauge choice is

$$\begin{aligned} \partial_t \alpha &= -\alpha^2 K + \eta_L \alpha^2 \log \left(\frac{\gamma^{p/2}}{\alpha} \right) + \beta^i \partial_i \alpha, \\ \partial_t \beta^i &= \alpha^2 {}^{(3)}\Gamma^i - \alpha \partial^i \alpha - \eta_S \beta^i + \beta^j \partial_j \beta^i, \end{aligned} \quad (4.11)$$

with K being the trace of the extrinsic curvature and ${}^{(3)}\Gamma^i$ the contracted Christoffel symbol of the spatial metric. Before blackhole formation in simulations of collapsing gravitational waves, the scalar functions η_L, η_S are set to

$$\eta_L = \bar{\eta}_L \alpha^q, \quad \eta_S = \bar{\eta}_S \alpha^r, \quad (4.12)$$

with $\bar{\eta}_L, \bar{\eta}_S, q, r$ being some constants. The default choice is $p = 1$ and $q = r = 0$, which naturally maintains the shift damping term even if the lapse function is close to zero, in contrast to the standard condition employed in SpEC [96], which takes $r = 1$.

Since the plan is to study near-singular gravitational effects in the computational domain and run-away growth of the shift vector needs to be avoided this seems reasonable. Adjustments to these choices when evolving near-critical data will be reported later in this work. Following [96], in simulations of blackholes using excision the parameter r is set to be $r = 1$. However, it was not found to be necessary to use the \log^2 form of η_L proposed by [96].

The constraint subsystem: The first order reduced harmonic constraints are

$$C_a = H_a + \gamma^{ij}\Phi_{ija} - \frac{1}{2}\gamma_a^i g^{cd}\Phi_{icd} + n^b\Pi_{ab} - \frac{1}{2}n_a g^{bc}\Pi_{bc}. \quad (4.13)$$

The terms without H_a are simply Γ_a . In these variables the vacuum ADM Hamiltonian 2.2 and momentum constraints 2.3 can be expressed as

$$\begin{aligned} 2G_{nn} &= \gamma^{ij}\gamma^{kl}(\partial_k\Phi_{ijl} - \partial_k\Phi_{lij} + \Gamma_{jk}^a\Gamma_{ail} - \Gamma_{ij}^a\Gamma_{akl}), \\ -\gamma^a_i G_{na} &= \gamma^{jk}(\partial_{[j}\Pi_{i]k} + \frac{1}{2}d_j\Phi_{kin} - \frac{1}{2}d_i\Phi_{jkn} - \frac{1}{2}\Pi_{j[i}\Phi_{j]nn} \\ &\quad + \gamma^{lm}\Phi_{mk[j}\Phi_{i]ln} + 2\Gamma_{an[i}\Gamma^a_{k]j}). \end{aligned} \quad (4.14)$$

Here the subscript n denotes the contraction with the normal vector n^a , with the convention that d_i stands for the partial derivative, but *with any such contraction outside of the derivative*. The Hamiltonian and momentum constraints can be put together as a four-vector of constraints

$$M^a = G^{an}. \quad (4.15)$$

Working with the first order system creates the reduction and closely related ordering constraints

$$\begin{aligned} C_{iab} &= \partial_i g_{ab} - \Phi_{iab} = 0, \\ C_{ijab} &= \partial_i\Phi_{jab} - \partial_j\Phi_{iab} = 2\partial_{[j}C_{i]ab} = 0. \end{aligned} \quad (4.16)$$

The constraints C_a and C_{iab} evolve according to

$$\begin{aligned}
\partial_t C_a &= (1 + \gamma_1)\beta^i \partial_i C_a - \gamma_1 \beta^i \bar{\partial}_i C_a + \alpha G_a + (\gamma_4 - \gamma_5)\alpha n_a \Gamma^b C_b - \alpha(2\gamma_4 - 1)\Gamma^b{}_{an} C_b \\
&\quad + 2\gamma_0 \alpha n^b n_{(a} C_{b)} + \alpha \gamma^{ij} \gamma^{kl} \Phi_{ikn} C_{ljn} n_a - \alpha \gamma^i{}_a C_{ijn} \left[\frac{1}{2} g^{bc} \Phi^j{}_{bc} + \Phi^j{}_{nn} \right] \\
&\quad - \gamma_1 \gamma_2 \beta^i \left(\frac{1}{2} g^{cd} C_{icd} n_a - C_{ina} \right), \\
\partial_t C_{iab} &= \beta^j (\partial_j C_{iab} + \gamma_1 \partial_i C_{jab}) + \alpha \left[(1 + \gamma_1) d_i g_{jn} C^j{}_{ab} \right. \\
&\quad \left. - \gamma_2 C_{iab} + \Phi^j{}_{ab} C_{ijn} + \frac{1}{2} C_{inn} \Pi_{ab} \right], \tag{4.17}
\end{aligned}$$

with the introduction of the constraint

$$G_a = 2M_a + (n_a \gamma^{ib} - \gamma^i{}_a n^b) (\bar{\partial}_i C_b - \Gamma^c{}_{ib} C_c) + \gamma_2 (\delta^c{}_a \gamma^{ib} - \frac{1}{2} g^{bc} \gamma^i{}_a) C_{ibc}, \tag{4.18}$$

and where the notation $\bar{\partial}_i$ means taking the partial derivative, and afterwards replacing all first derivatives of the metric with the reduction variable Φ_{iab} . Up to lower derivatives in the constraints it is

$$\partial_t G_a \approx \beta^i \partial_i G_a + \alpha \gamma^{ij} \partial_i \partial_j C_a - \alpha \gamma^{jk} \gamma^{li} \partial_l C_{ijka} + \frac{1}{2} \alpha \gamma^j{}_a \gamma^{il} g^{cd} \partial_l C_{ijcd}, \tag{4.19}$$

where \approx denotes equality up to non-principal terms, the remainder having been suppressed for brevity. The equation of motion for C_{ijab} is readily derived by taking derivatives of that of C_{iab} . Notice that the parameter γ_2 serves to damp the reduction constraint. In the description of [70] the equivalent reduction variable is called F_a , with, including γ_4 and γ_5 in the natural way

$$F_a = G_a - (1 - \gamma_4)(n_a \Gamma^b - 2 \Gamma^b{}_{an}) C_b - \gamma_5 n_a \Gamma^b C_b, \tag{4.20}$$

in terms of the variables used in this work. The difference is not substantial, being only that G_a appears slightly more naturally in the second order form of the equations. Note that in (4.20), the final term contains a piece which is simply the Harmonic constraint in the pure harmonic case, but will act as a non-zero coefficient otherwise.

First order reduction of the constraint subsystem: Following [70], a first order reduction of the constraint subsystem is formally introduced by defining the

new variable C_{ia} with

$$\begin{aligned}
 C_{ia} &= \gamma^{jk} \partial_j \Phi_{ika} - \frac{1}{2} \gamma_a^j g^{cd} \partial_j \Phi_{icd} + d_i \Pi_{an} - \frac{1}{2} n_a g^{cd} \partial_i \Pi_{cd} \\
 &+ \partial_i H_a + \frac{1}{2} \gamma_a^j \Phi_j^{cd} \Phi_{icd} + \frac{1}{2} \gamma^{jk} \Phi_{jc}{}^c \Phi_{ikn} n_a \\
 &- \gamma^{jk} \gamma^{lm} \Phi_{jla} \Phi_{ikm} + \frac{1}{2} \Phi_{icd} \Pi_{be} n_a (g^{cb} g^{de} + \frac{1}{2} g^{be} n^c n^d) \\
 &- \Phi_{icn} \Pi_{ba} (g^{bc} + \frac{1}{2} n^b n^c) + \frac{1}{2} \gamma_2 (n_a g^{cd} - 2 \delta_a^c n^d) C_{icd}.
 \end{aligned} \tag{4.21}$$

The principal part of this formal reduction is given by

$$\begin{aligned}
 \partial_t C_a &\approx 0, \\
 \partial_t G_a &\approx \beta^i \partial_i G_a + \alpha \gamma^{ij} \partial_i C_{ja}, \\
 \partial_t C_{ia} &\approx \beta^j \partial_j C_{ia} + \alpha \partial_i G_a, \\
 \partial_t C_{iab} &\approx (1 + \gamma_1) \beta^j \partial_j C_{iab}, \\
 \partial_t C_{ijab} &\approx \beta^k \partial_k C_{ijab}.
 \end{aligned} \tag{4.22}$$

The characteristic variables of the constraint subsystem are then found to be

$$\begin{aligned}
 c_a^{\hat{\pm}} &= F_a \mp C_{sa}, & c_a^{\hat{0}} &= C_a, \\
 c_{Aa}^{\hat{\beta}} &= q^i A C_{ia}, & c_{iab}^{\hat{1}} &= C_{iab}, \\
 c_{ijab}^{\hat{\beta}} &= C_{ijab},
 \end{aligned} \tag{4.23}$$

with speeds $\beta^s \mp \alpha, 0, \beta^s, (1 + \gamma_1) \beta^s$ and β^s respectively. A suitable norm of the constraint violation is given by the constraint monitor which is defined as

$$\begin{aligned}
 C_{\text{mon}} &= \int d^3x \sqrt{\gamma} \left(\delta^{ab} F_a F_b + \delta^{ab} C_a C_b + \gamma^{ij} \delta^{ab} C_{ia} C_{jb} \right. \\
 &\quad \left. + \gamma^{ij} \delta^{ac} \delta^{bd} C_{iab} C_{jcd} + \gamma^{ij} \gamma^{kl} \delta^{ac} \delta^{bd} C_{ikab} C_{jlcd} \right).
 \end{aligned} \tag{4.24}$$

The gravitational wave degrees of freedom: In vacuum the Weyl scalars Ψ_0, Ψ_4 can be expressed as

$$\begin{aligned}
 \Psi_0 &= m^A m^B [\perp^{(P)bd}{}_{AB} l^a l^c R_{abcd}], \\
 \Psi_4 &= m^A m^B [\perp^{(P)bd}{}_{AB} k^a k^c R_{abcd}],
 \end{aligned} \tag{4.25}$$

respectively. Here a null tetrad

$$\begin{aligned} l^a &= \frac{1}{\sqrt{2}}(n^a + s^a), & k^a &= \frac{1}{\sqrt{2}}(n^a - s^a), \\ m^a &= \frac{1}{\sqrt{2}}(v^a + iw^a), & \bar{m}^a &= \frac{1}{\sqrt{2}}(v^a - iw^a), \end{aligned} \quad (4.26)$$

was used with s^a , v^a and w^a mutually orthogonal unit spatial vectors. Furthermore the projection operator

$$\perp^{(P)cd}{}_{ab} = q^c{}_{(a}q^d{}_{b)} - \frac{1}{2}q^{cd}q_{ab} = m_{(a}m_b)\bar{m}^{(c}\bar{m}^{d)} + \bar{m}_{(a}\bar{m}_b)m^{(c}m^{d)}, \quad (4.27)$$

has been introduced. In terms of the first order GHG variables the principal part of the Riemann tensor can be expressed as

$$\begin{aligned} R_{abcd} &\approx \gamma^j{}_a\partial_i\Phi_{jb[c}\gamma_{d]}^i - \gamma^j{}_b\partial_i\Phi_{ja[c}\gamma_{d]}^i + n_a\partial_i\Pi_{b[c}\gamma_{d]}^i - n_b\partial_i\Pi_{a[c}\gamma_{d]}^i + \gamma^i{}_a\partial_i\Pi_{b[c}n_{d]} \\ &\quad - \gamma^i{}_b\partial_i\Pi_{a[c}n_{d]} - n_a\gamma^{ij}\partial_i\phi_{jb[c}n_{d]} + n_b\gamma^{ij}\partial_i\phi_{ja[c}n_{d]} - \gamma_1\gamma_2n_a n^k\partial_k g_{b[c}n_{d]} \\ &\quad + \gamma_1\gamma_2n_b n^k\partial_k g_{a[c}n_{d]} - \gamma_2\gamma^i{}_a\partial_i g_{b[c}n_{d]} + \gamma_2\gamma^i{}_b\partial_i g_{a[c}n_{d]}. \end{aligned} \quad (4.28)$$

Of course this expression is unique only up to constraint additions. Note that upon contraction with $\perp^{(P)}$ and l to form the Weyl scalar Ψ_0 , and after a single addition of C_{ijab} , naturally a projection of the incoming characteristic variable $d_s u_{ab}^\dagger$ is formed. This is used in the construction of the boundary condition. Again the spatial vector s^i is taken to be the unit normal to the boundary.

Boundary conditions: At the outer boundary the incoming constraint violation, gauge perturbations and physical radiation need to be controlled. By default initially

$$F_a + C_{sa} + \frac{1}{r}C_a \hat{=} 0, \quad (4.29)$$

is imposed on the constraint subsystem assuming that the characteristic variable c_a^\dagger is always incoming. These conditions are essentially those of [70], with just the additional $1/r$ term. Other conditions for this variable will be motivated and tested in what follows. The remaining constraint subsystem characteristic variables may or may not be incoming, and are dealt with on this basis as described in section 4.2.5, but always according to the same prescription. For the gravitational wave degrees of freedom

$$\Psi_0 \hat{=} q_0, \quad (4.30)$$

is imposed. This is the lowest order member of a cascade of conditions on incoming radiation [30, 31], with given data q_0 . Examining (4.25) it is obvious that this is equivalent to setting

$$\perp_{AB}^{(P)bd} (l^a l^c R_{abcd}) = \perp_{AB}^{(P)bd} q_{bd}^{(P)}, \quad (4.31)$$

which is in practice how the conditions are implemented in **bamps**. For the remaining gauge degrees of freedom either the improved gauge boundary conditions of [82],

$$\perp_{ab}^{(G)cd} \partial_t [u_{cd}^{\hat{\dagger}} + (\gamma_2 - r^{-1})g_{cd}] \hat{=} 0, \quad (4.32)$$

or the alternative

$$\perp_{ab}^{(G)cd} \left[d_s u_{cd}^{\hat{\dagger}} - 2\bar{d}_s [n_{(c} H_{d)}] + \gamma_2 \Phi_{scd} + r^{-1} (u_{cd}^{\hat{\dagger}} - 2n_{(c} H_{d)} + \gamma_2 g_{cd}) \right] \hat{=} 0, \quad (4.33)$$

are set. Here, the gauge projection operator

$$\perp_{ab}^{(G)cd} = l_{(a} k_b) l^{(c} k^{d)} + k_a k_b l^c l^d - 2k_{(a} q_b)^{c} l^d \quad (4.34)$$

was used. The overbar derivative notation has the same meaning as in equation (4.18). The given data $q_{cd}^{(G)}$ will often be chosen to vanish. These conditions are similar to the ‘freezing’ gauge boundary conditions employed in [70], but taking into consideration the discussion of gauge reflections given in [82]. Furthermore, they are constructed so that the conditions are naturally applied to metric components (in ADM form) and their derivatives, but excluding contributions from the gauge sources. In the **bamps** simulation typically it is tried to choose the given data to be fixed in time, and such that initially the time derivatives vanish for these quantities. The above boundary conditions are implemented in **bamps** using the Bjørhus method [23] as in SpEC. Details of the method are explained in section 4.2.5. For completeness here the constraint projection $\perp^{(C)} = I - \perp^{(P)} - \perp^{(G)}$ is

$$\perp_{ab}^{(C)cd} = \frac{1}{2} q_{ab} q^{cd} - 2l_{(a} q_b)^{c} k^{d)} + l_a l_b k^c k^d, \quad (4.35)$$

It plays an important role in the implementation of the boundary conditions, as they are again naturally written in the form $\perp_{ab}^{(C)cd} d_s u_{cd}^{\hat{\dagger}} = (\text{transverse derivatives})_{ab}$.

4.1.2 Constraint preserving boundary conditions and damping

Generalized harmonic constraint subsystem: The constraint subsystem of the first order reduction of the GHG system was already presented in the previous section. In order to get a better idea of the effect of the different constraint preserving boundary conditions now the subsystem without the reduction is considered. It is

$$\begin{aligned}\nabla^b Y_{ba} &= -R_{ab} C^b, \\ Y_{ba} &= \nabla_b C_a + 2\gamma_4 \Gamma^c{}_{ab} C_c - (\gamma_4 - \gamma_5) g_{ab} \Gamma^c C_c - 2\gamma_0 n_{(a} C_{b)}.\end{aligned}\quad (4.36)$$

The shorthand Y_{ab} and the variable G_a that follows will be related to quantities present in the first order reduction of the GHG formulation shortly. Equivalently this can be express as

$$\begin{aligned}n^b \partial_b C_a &= G_a - (2\gamma_4 - 1) \Gamma^c{}_{ab} n^b C_c - (\gamma_4 - \gamma_5) n_a \Gamma^c C_c + 2\gamma_0 n^b n_{(a} C_{b)}, \\ n^b \partial_b G_a &= \gamma^{bc} \nabla_b [\nabla_c C_a + 2\gamma_4 \Gamma^d{}_{ac} C_d - (\gamma_4 - \gamma_5) g_{ac} \Gamma^d C_d - 2\gamma_0 n_{(a} C_{c)}] \\ &\quad + (n^b \nabla_b n^c) [\nabla_c C_a + 2\gamma_4 \Gamma^d{}_{ac} C_d - (\gamma_4 - \gamma_5) g_{ac} \Gamma^d C_d - 2\gamma_0 n_{(a} C_{c)}] \\ &\quad + \Gamma^c{}_{ab} n^b C_c + R_{ab} C^b,\end{aligned}\quad (4.37)$$

where the variable

$$G_a = n^b Y_{ba} = 2M_a + (n_a \gamma^{ib} - \gamma^i{}_a n^b) \nabla_i C_b, \quad (4.38)$$

is used to allow for the most convenient form of these expressions. Different choices of the constraint addition parameters γ_4, γ_5 result in different behavior in terms of growth of the constraint fields. It is also obvious that different choices of these parameters can simplify the constraint subsystem, the natural choice seemingly being $\gamma_4 = \gamma_5 = 1/2$.

Linearization: Now the behavior of a set of fields that satisfies the linearized equations on a fixed constraint satisfying background is considered. First, in equation (4.36) the tetrad consisting of the null vectors l^a, k^a, m^a, \bar{m}^a defined in (4.26) is used to decompose the first index of Y_{ba} . From this the condition

$$\nabla^b \left(k_b l^c Y_{ca} + l_b k^c Y_{ca} - m_b \bar{m}^c Y_{ca} - \bar{m}_b m^c Y_{ca} \right) = 0, \quad (4.39)$$

for the linearization is obtained. Here the notation C_a for the linearized violation can be used because the constraints are satisfied in the background.

Boundary conditions: Taking the standard setup at the outer boundary, so that s^a , used in the construction of the tetrad, denotes the outward pointing spatial unit vector normal to the boundary. Restricting the attention to boundary conditions that contain at most one derivative of the constraints, *geometrically* the most natural choice seems to be $l^b Y_{ba} \hat{=} 0$. In the first order GHG language these conditions are

$$G_a + \nabla_s C_a + 2\gamma_4 \Gamma^c_{as} C_c + (\gamma_4 - \gamma_5) s_a \Gamma^b C_b - \gamma_0 n_a C_s \hat{=} 0. \quad (4.40)$$

Whereas, discarding the first order reduction, those of (4.29) are instead

$$G_a + \nabla_s C_a + \Gamma^c_{as} C_c - (2\gamma_4 - 1) \Gamma^c_{an} C_c - (\gamma_4 - \gamma_5) n_a \Gamma^b C_b + \frac{1}{r} C_a \hat{=} 0. \quad (4.41)$$

With either conditions one might guess that the choice $\gamma_4 = \gamma_5 = 1/2$ reduces reflections from the boundary, especially when using a non-harmonic $\Gamma_a = -H_a \neq 0$ gauge. Incidentally this choice also makes the two conditions almost coincident. Suppose, all derivatives of C_a, G_a tangent to the boundary vanish, and that the background is flat. Then the solutions can be analyzed in the same type of approximation.

Mode solutions on flat-space: When linearized around flat-space this system takes the form

$$\square C_a - 2\gamma_0 \partial^b (n_{(a} C_{b)}) = 0. \quad (4.42)$$

The right-travelling mode solutions are

$$C_n = \rho_1 e^{s_1^+ t + i\omega x} + \rho_2^s e^{s_2^+ t + i\omega x}, \quad C^i = \rho_2^i e^{s_2^+ t + i\omega x}, \quad (4.43)$$

with eigenfrequencies

$$s_1^+ = -\frac{1}{2}\gamma_0 - \frac{i}{2}\sqrt{4\omega^2 - \gamma_0^2}, \quad s_2^+ = -\gamma_0 - i\sqrt{\omega^2 - \gamma_0^2}. \quad (4.44)$$

A very desirable property for the boundary conditions would be that they absorb outward going waves perfectly, that is, without reflection. With this motivation high-

order derivative boundary conditions on the gravitational wave degrees of freedom have been studied [30, 31], and implemented in the SpEC code [81] in order to absorb higher spherical harmonics of the Weyl scalar Ψ_4 . In the current context absorption means that outgoing mode solutions, those associated with an s^+ , lie in the kernel of the boundary conditions. This is only the case if the damping $\gamma_0 = 0$ is switched off. Since the low order spherical harmonics might be expected to dominate in the gauge and constraint subsystems, optimizing against this phenomena may be more important than using high-order conditions for the gauge and constraint subsystems whilst neglecting the damping terms.

Remainder of mode solutions: Substituting these mode solutions into the boundary conditions (4.41), or the natural geometric conditions (4.40), each after appropriate linearization, and expansion at large frequency ω gives remainders of order $O(\gamma_0 C_a)$, indicating that neither is the optimal that can be obtained by adding source terms to the constraint boundary conditions. Taking instead

$$\begin{aligned} (\partial_t + \partial_s + \gamma_0)C_n + \frac{1}{2}\gamma_0 C_x &\hat{=} 0, \\ (\partial_t + \partial_s + \frac{1}{2}\gamma_0)C_i &\hat{=} 0, \end{aligned} \tag{4.45}$$

the remainder is rather of order $O(\gamma_0 C_a \omega^{-1})$. There is some freedom in expressing these conditions in the first order GHG language

$$\begin{aligned} G_a + \nabla_s C_a + 2\gamma_4 \Gamma_{as}^c C_c + (\gamma_4 - \gamma_5) s_a \Gamma^b C_b \\ + \frac{1}{2}\gamma_0 \gamma_a^b C_b - \gamma_0 n_a (C_n + \frac{1}{2}C_s) + \frac{1}{r}C_a &\hat{=} 0. \end{aligned} \tag{4.46}$$

The conditions (4.40) can be similarly rewritten. A similar analysis can be performed using the pure gauge subsystem presented in [65], but simulations with `bamps` show that the existing gauge boundary conditions are so far sufficient. Tests with the various boundaries are presented in section 6.

4.2 The `bamps` code

4.2.1 Grid setup

Grid types: The numerical domain on which the evolution equations 4.1 are solved in `bamps` is either a cubed-ball or a cubed-shell grid. Each type is built up of multiple deformed cubes. Two dimensional sketches of both setups are shown in Fig. 7. A patch is described by two fundamental overlapping charts. In *local*

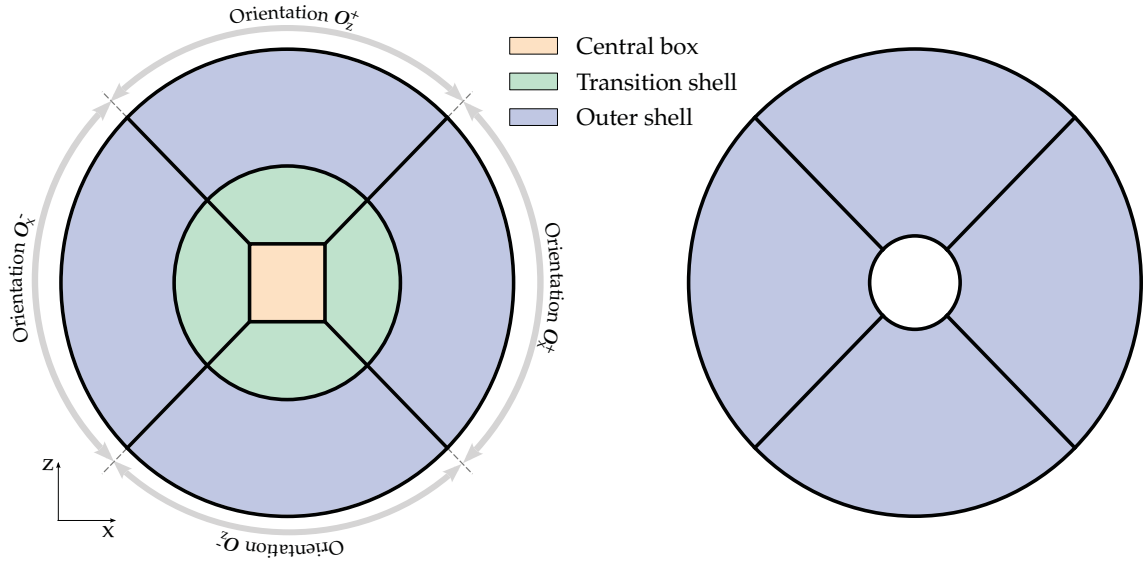


Figure 7: In this figure 2d sketches of the **bamps** grid setups are shown. On the left is the cubed-ball grid, on the right the cubed-shell grid. The grids are built up of several coordinate patches which are deformed cubes.

coordinates \bar{x}, \bar{y} and \bar{z} it is a rectangular box $[\bar{x}_0, \bar{x}_1] \times [-1, 1] \times [-1, 1]$. In *global Cartesian coordinates* x, y and z the cubes are transformed and rotated in such a way that when added together they build the desired domain. A more detailed description of the applied coordinate transformation is given in the following. The cubed-ball grid includes the origin and has a spherical outer boundary. It consists of 13 coordinate patches:

The central cube is centered around the origin and ranges from $-r_{\text{cu}}$ to r_{cu} in the global Cartesian coordinate directions.

The transition shell transfers the grid from the inner cube grid to a spherical shell with radius r_{cs} . It contains six patches.

The outer shell consists of six patches which extends the grid with additional cubed-shells up to the outer grid boundary at r_{ss} .

The cubed-shell grid is an excision grid, meaning that it does not include the origin. It is a special case of the cubed-ball grid, consisting only of the six outer shell coordinate patches.

Cubed sphere coordinate transformation: The coordinate transformation used in **bamps** to construct the grids introduced above relies on the so-called “cubed

sphere” construction. It was introduced by [83] and first applied in the context of numerical relativity in [101, 102]. Since then this idea was implemented in multi-patch approaches [69, 74, 88, 109]. In contrast to many of the earlier examples, the numerical method of **bamps** does not require overlapping grids, which simplifies the discussion. In [83], the coordinates are constructed by considering great arcs parametrized by equidistant angles. Such angle coordinates are used in [74, 101, 102], while [69, 109] use an intermediate set of coordinates also given in [83] that does not have the equidistant angle property. In **bamps** the latter type of coordinates is applied. The concrete coordinate transformation is the following. First, the local coordinates of each patch are transformed to temporary coordinates

$$x_{\text{temp}} = \frac{\bar{x}}{\bar{s}}, \quad y_{\text{temp}} = \frac{\bar{x}\bar{y}}{\bar{s}}, \quad z_{\text{temp}} = \frac{\bar{x}\bar{z}}{\bar{s}}. \quad (4.47)$$

This patch, which is orientated in positive x direction, will later be referred to as the master patch. From here, cyclic permutation by some 90 degrees is used to rotate the patches from their temporary position to their final location in the sphere. The denominator \bar{s} depends on where the coordinate transformation happens. For the patches of the outer shell it is

$$\bar{s} \equiv (1 + \bar{y}^2 + \bar{z}^2)^{1/2}, \quad (4.48)$$

In the transition shell its definition includes a transition function λ ,

$$\bar{s}(\lambda) = \left(\frac{1 + 2\lambda}{1 + \lambda(\bar{y}^2 + \bar{z}^2)} \right)^{1/2}, \quad \lambda = \frac{\bar{x}^2 - \bar{x}_0^2}{\bar{x}_1^2 - \bar{x}_0^2}. \quad (4.49)$$

This coordinate transformation is constructed to transition from the inner cube to the outer shells. Note that this transformation is uniform along the 3d diagonals, where the distance between inner and outer shell boundary is smallest. This significantly improves the maximum possible timestep in the transition shell.

Subpatches: Each coordinate patch can be further divided into subpatches. Subpatches are helpful for increasing resolution, and form the backbone of the parallelism of **bamps**. Each master patch can be split into $\mathcal{N}_x \times \mathcal{N}_y \times \mathcal{N}_z$ subpatches with coordinates

$$\bar{x}^i \in [\bar{x}_0^i + k^i \Delta \bar{x}^i, \bar{x}_0^i + (k^i + 1) \Delta \bar{x}^i], \quad (4.50)$$

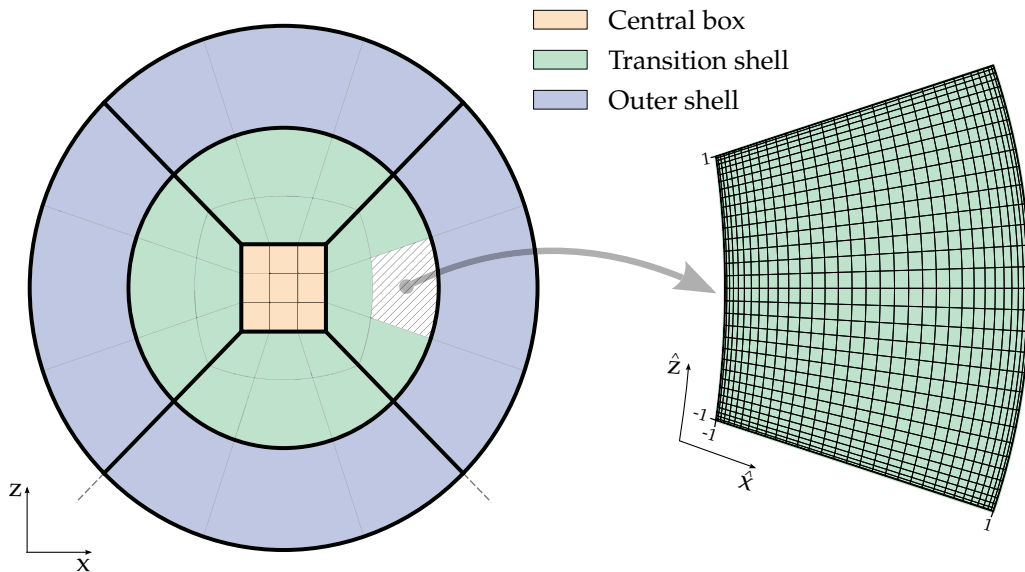


Figure 8: The left part of the diagram gives a two dimensional sketch of the **bumps** cubed-ball grid layout. The ball is built up of several transformed cubes. These patches can further be divided into subpatches. In the example shown it is $\mathcal{N}_{\text{cu}} = 3$, $\mathcal{N}_{\text{cs}} = 2$ and $\mathcal{N}_{\text{ss}} = 1$. On the right is shown that each subpatch is covered by Gauss-Lobatto grids ranging from -1 to 1 in local coordinates.

with $\Delta\bar{x}^i = (\frac{\bar{x}_1 - \bar{x}_0}{\mathcal{N}_x}, \frac{2}{\mathcal{N}_y}, \frac{2}{\mathcal{N}_z})$ and $k^i = 0, \dots, \mathcal{N}_i - 1$. In practice the subdivisions are made in such a way that subgrids of two neighboring patches match, and that neighboring patches and subpatches share grid-point positions on their respective boundaries. This is necessary because the current implemented patching boundary treatment relies on the fact that the grid points match. Concretely the inner cube is split into $\mathcal{N}_{\text{cu}} \times \mathcal{N}_{\text{cu}} \times \mathcal{N}_{\text{cu}}$ subpatches. The transition and outer shell are divided in \mathcal{N}_{cs} or \mathcal{N}_{ss} subpatches in the radial direction. For the angular direction the number of subpatches is chosen to be $\mathcal{N}_{\text{cu}} \times \mathcal{N}_{\text{cu}}$. In Fig. 8 a 2d sketch of the **bumps** cubed-ball grid subdivided into subpatches is illustrated.

4.2.2 Numerical method

Spatial discretization: In **bumps** the spatial right hand sides of the evolution equations are approximated using a pseudospectral method (also see section 2.2). A linear transformation is used to map the local coordinates of each subpatch \bar{x}^i into a unit cube $\tilde{x}^i = (\tilde{x}, \tilde{y}, \tilde{z})^T \in [-1, 1]^3$. A subpatch is discretized by Gauss-Lobatto

collocation points in each dimension,

$$\tilde{x}_\alpha = -\cos\left[\frac{\pi}{N_x-1}\alpha\right] \text{ with } \alpha = 0, \dots, N_x - 1, \quad (4.51)$$

and similarly in the other directions. The number of grid points N depends on the patch location in the grid. The central cube is discretized with $N_{\text{cu}} \times N_{\text{cu}} \times N_{\text{cu}}$ points. The radial directions of the transition and outer shell are filled with N_{cs} and respectively N_{ss} points. The number of angular points are chosen to be the same as in the central cube. This assures that the grids are matching. In Fig. 8 on the right the Gauss-Lobatto discretization of a subpatch is shown.

Basis expansion: On the collocation points all evolution fields u are expanded in each dimension in a spectral basis using Chebyshev polynomials $T_n(x)$. For example, in the \tilde{x} direction it is

$$u_{\alpha\beta\delta} = u(\tilde{x}_\alpha, \tilde{y}_\beta, \tilde{z}_\delta) = \sum_{n=0}^{N_x-1} c_n^x(\tilde{y}_\beta, \tilde{z}_\delta) T_n(\tilde{x}_\alpha), \quad (4.52)$$

and analogously in the remaining two directions. Here the pseudospectral approach is used. This means that not the expansion coefficients c^x, c^y, c^z are stored but the function values $u_{\alpha\beta\delta}$ at the collocation points $\tilde{x}_{\alpha\beta\delta}^i$.

Derivatives: The spatial derivatives of the evolution fields are computed by a matrix multiplication. For example in the \tilde{x} -direction it is

$$(\partial_{\tilde{x}} u)_{\alpha\beta\delta} = \sum_{n=0}^{N_x-1} D_{\alpha n} u_{n\beta\delta}, \quad (4.53)$$

with the Gauss-Lobatto derivative matrix (2.24). Afterwards the derivatives are transformed to global Cartesian coordinates with the appropriate Jacobian. In **bamps** the diagonal terms of the derivative matrix are not computed by the analytic formulas stated above but the identity

$$D_{\alpha\alpha} = -\sum_{n=0, n \neq \alpha}^{N_x-1} D_{\alpha n} \quad (4.54)$$

is used. This *negative-sum-trick* maps a constant function explicitly to zero and is known to give the derivative matrix better stability with regards to rounding errors [19].

Time integration: The evolution fields are integrated forward in time using a 4th order Runge-Kutta scheme. Unless otherwise stated in the following the time-step is set to $\Delta t = \frac{1}{4}\Delta x_{\min}$, with Δx_{\min} being the minimal Cartesian spatial grid spacing of the whole domain. Empirically it was found within the following simulations that this choice always leads to stable numerical evolutions, in the sense that increasing resolution results in smaller errors. A stability analysis of the fully discrete system has not been carried out within this work.

Filtering: A crucial ingredient for numerical stability of the following simulations is the use of a filter against high-frequency growth. Following [96] exactly, after every full time-step the filter is applied in each dimension. The filter is easily implemented as a matrix multiplication. For example, in the \tilde{x} direction, the function values are filtered by

$$(\mathcal{F}u)_{\alpha\beta\gamma} = \sum_{n=0}^{N_x-1} \mathcal{F}_{n\alpha} u_{n\beta\gamma}, \quad (4.55)$$

with the filter matrix

$$\mathcal{F}_{\alpha\beta} = \sum_{n=0}^{N_x-1} S_{\alpha n} e^{-36(n/n_{\max})^{64}} A_{n\beta}. \quad (4.56)$$

where $n_{\max} = N_x - 1$ and $S_{\alpha\beta}$ and $A_{\alpha\beta}$ are the Chebyshev synthesis and analysis matrices respectively (also see [26, 106]).

4.2.3 Imposition of octant symmetry

bamps octant grid: When evolving octant symmetric data in **bamps**, it is possible to only evolve one eighth of the cubed-ball grid. This saves computational and memory costs. In the **bamps** octant mode an odd number of subpatches \mathcal{N}_{cu} and an odd number of grid points N_{cu} has to be chosen. The numerical domain is reduced to $x \geq 0$, $y \geq 0$ and $z \geq 0$, as sketched in Fig. 9. This means that all subpatches containing one of the Cartesian axes are cut in half along them. In these patches the symmetry is used to construct special matrices which compute the derivatives and filters.

Matrix construction: Consider discrete function values u_k on a Gauss-Lobatto grid with an odd number of N collocation points. The function should be defined

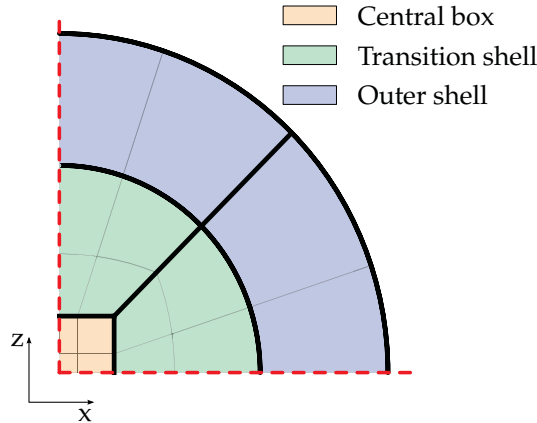


Figure 9: For octant symmetric data the symmetry is used to evolve only one eighth of the full domain. An odd number of subpatches \mathcal{N}_{cu} is taken and the subpatches containing the axis are cut in each symmetry direction. The figure shows the remaining grid in the xz plane.

from $-x_{\text{max}}$ to x_{max} and be symmetric around $x = 0$. Then,

$$u_{n^*-i} = \pm u_{n^*+i}, \quad (4.57)$$

where $n^* = (N - 1)/2$ and $i = 1, \dots, n^*$. The sign obviously depends on the parity function around $x = 0$. Because of this symmetry it is only necessary to store half the function values, for example $n = n^*, \dots, N - 1$, without losing information. For taking derivatives or filtering the data it is possible to either reconstruct the full vector of N points by copying the function values with the correct parity, or to construct special matrices using the symmetry condition. In **bamps** the latter choice is made. The matrices of dimension $N \times N$ are of the form,

$$M = \begin{bmatrix} A_{ij} & 2a_i & B_{ij} \\ b_j & 2c & d_j \\ C_{ij} & 2e_i & D_{ij} \end{bmatrix}, \quad (4.58)$$

where i and j run from 0 to $n^* - 1$. Out of this “full” matrix two “octant” matrices are constructed which operate on the reduced data,

$$M^\pm = \pm \begin{bmatrix} c & b_{n^*-1-j} \\ e_i & C_{i,n^*-1-j} \end{bmatrix} + \begin{bmatrix} c & d_j \\ e_i & D_{ij} \end{bmatrix}. \quad (4.59)$$

For even functions M^+ , for odd functions M^- is taken.

		$\beta^s > \alpha > 0$	$\alpha > \beta^s > 0$	$\beta^s = 0$	$-\alpha < \beta^s < 0$	$\beta^s < -\alpha < 0$
$u_{ab}^{\hat{0}}$	0	zero	zero	zero	zero	zero
u_{ab}^{-}	$\beta^s - \alpha$	incoming	outgoing	outgoing	outgoing	outgoing
u_{ab}^{\dagger}	$\beta^s + \alpha$	incoming	incoming	incoming	incoming	outgoing
$u_{Aab}^{\hat{\beta}}$	β^s	incoming	incoming	zero	outgoing	outgoing

Table 2: Incoming and outgoing characteristic variables to a subpatch boundary with spatial normal vector s^i depending on the gauge variables.

4.2.4 Patching boundary conditions

In order to glue all subpatches together appropriate conditions at the connecting boundaries of the subpatches have to be imposed. For this the penalty method is applied as described in [60, 61, 97]. The main idea of this method is to add penalty terms for each incoming characteristic variable at the boundary to the right hand side of the evolution equations. On the boundary surface the outward pointing spatial normal vector s^i is defined. The characteristic variables of the evolution system are given in equation (4.5) with speeds (4.6). Incoming characteristic variables to the subpatch boundary have positive speeds. On these the condition that they are equal to the outgoing characteristic variables of the neighboring subpatch has to be imposed. Table 2 summarizes all incoming and outgoing characteristic variables depending on the lapse function α and the shift in s^i direction, β^s . As an example, now the boundary between two subpatches, subpatch L and subpatch R , and the case $-\alpha < \beta^s < 0$, is considered. With respect to the spatial normal vector s^i at the boundary pointing outwards of subpatch L and inwards in subpatch R , the incoming characteristic variables of L are the outgoing ones of R . In the chosen case, u_{ab}^{\dagger} are incoming to L and outgoing of R . The condition to be imposed is

$$u_{ab}^{\dagger L} \hat{=} u_{ab}^{\dagger R}. \quad (4.60)$$

Multiplying the evolution equations 4.2 from the left with the matrix of eigenvectors $T^{-1\hat{\alpha}}_{\beta}$, the evolution equations for the characteristic variables are obtained,

$$d_t u^{\hat{\alpha}L} = T^{-1\hat{\alpha}}_{\mu} A^{k\mu}_{\nu} \partial_k u^{\nu L} + T^{-1\hat{\alpha}}_{\mu} S^{\mu}. \quad (4.61)$$

Here, the d denotes that the transformation $T^{-1\hat{\alpha}}_{\mu}$ stands outside the partial derivative. At the boundary a penalty to the right hand side of the evolution equation of the incoming characteristic is added, which is often called *weakly imposing* the

boundary condition

$$d_t u_{ab}^{\hat{\dagger}L} \hat{=} T^{-1\hat{\dagger}}{}_{\mu} A^{k\mu}{}_{\nu} \partial_k u_{ab}^{\nu L} + T^{-1\hat{\dagger}}{}_{\mu} S^{\mu} + p \left(u_{ab}^{\hat{\dagger}R} - u_{ab}^{\hat{\dagger}L} \right). \quad (4.62)$$

Afterwards the inverse transformation is used to get back to the evolution equations enhanced with the necessary penalty terms at the boundary. These are also the equations which are implemented in the code. All six boundaries of the subpatches are treated independently from each other. This means that on the edges penalty contributions from two on the corner from three directions have to be considered. The size of the penalty parameter p can be derived from an energy estimate of the semi-discrete evolution system. This is presented in section 4.3.

4.2.5 Outer boundary implementation

At the spherical outer boundary of the domain the Bjørhus method [23, 70] is used to impose the constraint, physical and gauge conditions given in section 4.1. As for the patching boundaries, the conditions are imposed on the incoming characteristic variables. However, this time no penalty terms are used but instead the right hand side of the evolution equations is modified at the boundary in such a way that the boundary conditions are satisfied. On the boundary surface the outward pointing spatial normal unit vector s^i is defined. The projection operator $q^j{}_i = \delta^j{}_i - s^j s_i$ is used to split the principal part of the evolution equation in a part normal and tangential to the boundary surface

$$\partial_t u^{\mu} \approx A^{k\mu}{}_{\nu} (s_k s^j + q^j{}_k) \partial_j u^{\nu} = A^{s\mu}{}_{\nu} \partial_s u^{\nu} + A_{\nu}^{A\mu} q_A^B \partial_B u^{\nu}. \quad (4.63)$$

Expressed in characteristic variables the normal part is

$$d_t u^{\hat{\alpha}} \sim T^{-1\hat{\alpha}}{}_{\mu} A^{s\mu}{}_{\nu} T^{\nu}{}_{\hat{\beta}} T^{-1\hat{\beta}}{}_{\xi} \partial_s u^{\xi} = \Lambda^{s\hat{\alpha}}{}_{\hat{\beta}} d_s u^{\hat{\beta}}. \quad (4.64)$$

Again the straight d derivative symbol denotes that the transformation matrix stands outside the partial derivative. The matrix $\Lambda^{s\hat{\alpha}}{}_{\hat{\beta}}$ is a diagonal matrix containing the characteristic speeds. At the outer boundary it is reasonable to assume that the absolute value of the shift β^s is always smaller than the size of the lapse α . This leads to two cases to be considered.

Case $-\alpha < \beta^s < 0$: In this case the incoming characteristic at the outer boundary condition is $u^{\hat{\dagger}}$. According to section 4.1 the following boundary conditions, which

are repeated schematically, have to be imposed:

1. One of the constraint preserving boundary conditions (4.29), (4.40) or (4.46),

$$\perp^{(C)} d_s u^{\hat{\dagger}} + P^{(C)} + NP^{(C)} \hat{=} 0. \quad (4.65)$$

2. One of the gauge boundary conditions (4.32) or (4.33), which become either,

$$\begin{aligned} \perp^{(G)} d_t u^{\hat{\dagger}} + P^{(G)} + NP^{(G)} &\hat{=} 0, \\ \perp^{(G)} d_s u^{\hat{\dagger}} + P^{(G)} + NP^{(G)} &\hat{=} q^{(G)}. \end{aligned} \quad (4.66)$$

3. The physical boundary condition (4.30),

$$\perp^{(P)} d_s u_{ab}^{\hat{\dagger}} + P^{(P)} + NP^{(P)} \hat{=} q^{(P)}. \quad (4.67)$$

Here the principal terms with derivatives tangent to the boundary are labeled with $P^{(x)}$ and the non-principal terms with $NP^{(x)}$. At the boundary surface the normal part of evolution equation of the incoming characteristic $u^{\hat{\dagger}}$ is projected into the constraint, the physical and gauge part

$$d_t u_{ab}^{\hat{\dagger}} \approx v^{\hat{\dagger}} (\perp_{ab}^{(C) cd} + \perp_{ab}^{(P) cd} + \perp_{ab}^{(G) cd}) d_s u_{cd}^{\hat{\dagger}}. \quad (4.68)$$

All three parts have to be replaced using the boundary conditions. This is done by subtracting the conditions from the bulk right hand side, which is denoted as $D_t u_{ab}^{\hat{\dagger}}$,

$$d_t u_{ab}^{\hat{\dagger}} \hat{=} D_t u_{ab}^{\hat{\dagger}} - v^{\hat{\dagger}} (\text{Conditions})_{ab}. \quad (4.69)$$

The special case (4.32) treated in the obvious way. Transforming back this modified right hand side leads to modified GHG evolution equations at the boundary.

Case $0 < \beta^s < \alpha$: In this case also the characteristic $u_{Aab}^{\hat{\beta}}$ is incoming. As described in [70], the additional constraint preserving boundary condition

$$d_s u_{Aab}^{\hat{\beta}} - s^i q^B_A \partial_B \Phi_{ibc} \hat{=} 0 \quad (4.70)$$

has to be imposed by subtracting it from the evolution equation, of $u_{Aab}^{\hat{\beta}}$

$$d_t u_{Aab}^{\hat{\beta}} = D_t u_{Aab}^{\hat{\beta}} - v^{\hat{\beta}} (\text{Condition})_{Aab}. \quad (4.71)$$

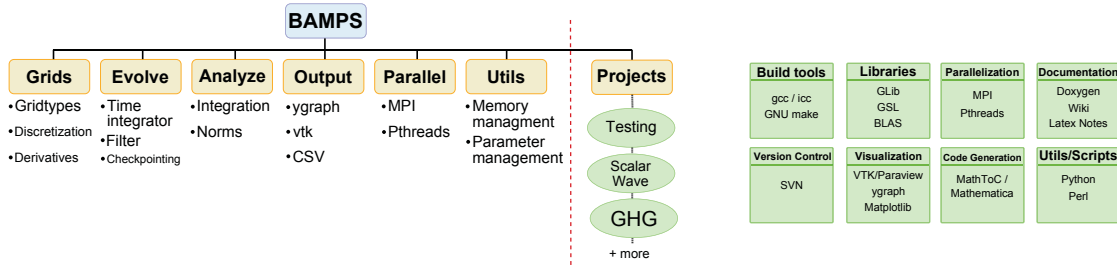


Figure 10: On the left an overview of the modular design of the **bamps** code is presented. The figure on the right lists the tools used within the **bamps** tool chain.

With this modified right hand side at the boundary the system is transformed back to the evolution equations for the evolution fields.

4.2.6 Code implementation details

Code structure: The **bamps** code is written in the C programming language in a modular fashion. The code is designed in such a way that the technical layer is separated from the actual projects for solving physics problems. Fig. 10 shows the code structure and names the tools used within the **bamps** infrastructure. Inside physics projects a Mathematica script, **MathToC**, translates equations written in tensor notation into C code. As a standalone program an axisymmetric apparent horizon finder, **AHloc**, has been developed. It is typically used to search for apparent horizons in **bamps** generated data at the post-processing step. It is also possible to run the finder in a daemon-like mode in which it searches horizons in data of a running instance of **bamps**. The apparent horizon finder is explained in more detail in subsection 5.2.

Computational method: The dominant computational methods within a simulation is dense matrix-matrix multiplications on a 3d data array. For this **bamps** relies on a handwritten function for all the simulations carried out within this work. Further details on the actual method can be found in [27].

Parallelization: **bamps** is programmed to run in parallel on several computing nodes using the message passing interface (MPI). The \mathcal{N}_{sub} subpatches of a **bamps** grid are distributed on M MPI processes as evenly as possible. This means that each process has to handle at least, $n = \lfloor \frac{\mathcal{N}_{\text{sub}}}{M} \rfloor$, subpatches. As in general the total number of grids is not divisible by the number of MPI processes without remainder, $\mathcal{N}_{\text{sub}} \bmod M$ processes have to take care of one additional grid. In practice the number of MPI processes is chosen in such a way that the number of processes

which have to compute one grid less is minimized.

4.3 Energy estimate for the penalty factor

In this section an estimate for the right choice of penalty factor at the patching boundaries of the `bamps` domains is derived. The actual technical implementation of the patching condition is explained in subsection 4.2.4. The calculation is based on the one presented in [97]. However, here it is presented for a general hyperbolic system in curvilinear coordinates, albeit under rather restrictive assumptions.

4.3.1 The continuum case

In the following calculation the evolution equations are written in the matrix notation as presented in (4.2), but with all non-principal terms S^μ and all state vector indices μ, ν suppressed. Furthermore, the calculation is carried out within the linear, constant coefficient approximation.

As the GHG system is symmetric hyperbolic, there is a symmetrizer H such that $HA^p s_p$ is Hermitian for every unit spatial vector s^p [62]. The energy of the system is

$$E^2 = \int_V dV u^\dagger H u, \quad (4.72)$$

with the volume form $dV = dx dy dz \sqrt{\gamma}$. As discussed in section 4.2, each subpatch of `bamps` has a set of global Cartesian coordinates $x^i = (x, y, z)$ and a set of local coordinates $\tilde{x}^i = (\tilde{x}, \tilde{y}, \tilde{z})$ in which the subpatch is a unit cube. The Jacobian $J_i^i = \frac{\partial x^i}{\partial \tilde{x}^i}$ transforms between the two charts. To formulate boundary conditions at the patching boundaries which control the energy in the subpatch, the time derivative of the energy is studied. Using the evolution equations to replace the time derivatives by spatial derivatives gives

$$\partial_t E^2 = \int dV \partial_p [u^\dagger H A^p u]. \quad (4.73)$$

In the constant coefficient approximation the determinant of the three metric in the volume form can be commuted with the partial derivative. This leads to a divergence in flat Cartesian coordinates

$$\partial_t E^2 = \int dx dy dz \partial_p [u^\dagger H A^p u \sqrt{\gamma}]. \quad (4.74)$$

Switching to the subpatch local coordinates gives

$$\partial_t E^2 = \int d\tilde{V} \frac{1}{\det J_i^i} \partial_{\tilde{p}} [u^\dagger H A^{\tilde{p}} u \sqrt{\tilde{\gamma}} \det J_i^i] = \int d\tilde{x} d\tilde{y} d\tilde{z} \partial_{\tilde{p}} \Phi^{\tilde{p}}. \quad (4.75)$$

Here it is $\sqrt{\tilde{\gamma}} := \sqrt{\gamma} \det J_i^i$ and the flux $\Phi^{\tilde{p}} = u^\dagger H A^{\tilde{p}} u \sqrt{\tilde{\gamma}}$ has been defined. Integrating over all boundary surfaces of the subpatch results in

$$\partial_t E^2 = \int_{-1}^1 \int_{-1}^1 d\tilde{y} d\tilde{z} \Phi^{\tilde{x}} \Big|_{\tilde{x}=-1}^1 + \int_{-1}^1 \int_{-1}^1 d\tilde{x} d\tilde{z} \Phi^{\tilde{y}} \Big|_{\tilde{y}=-1}^1 + \int_{-1}^1 \int_{-1}^1 d\tilde{x} d\tilde{y} \Phi^{\tilde{z}} \Big|_{\tilde{z}=-1}^1. \quad (4.76)$$

At a boundary surface, for example $\tilde{x} = \text{const}$, the unit normal vector can be written as,

$$\tilde{s}^i = \underbrace{(\tilde{\gamma}^{\tilde{j}\tilde{k}} \partial_{\tilde{j}} \tilde{x} \partial_{\tilde{k}} \tilde{x})^{-\frac{1}{2}}}_{\equiv l} \tilde{\gamma}^{\tilde{i}\tilde{k}} \partial_{\tilde{k}} \tilde{x} = l \partial^{\tilde{i}} \tilde{x}. \quad (4.77)$$

The spatial metric $\tilde{\gamma}_{ij}$ is 2 + 1 split,

$$\tilde{\gamma}_{ij} = \begin{pmatrix} l^2 + \tilde{\gamma}_{\tilde{x}\tilde{A}} \tilde{\gamma}_{\tilde{x}}^{\tilde{A}} & \tilde{\gamma}_{\tilde{x}\tilde{A}} \\ \tilde{\gamma}_{\tilde{x}\tilde{B}} & \tilde{q}_{\tilde{A}\tilde{B}} \end{pmatrix}. \quad (4.78)$$

The relationship between the determinant of $\tilde{\gamma}_{ij}$ and the metric in the boundary surface $\tilde{q}_{\tilde{A}\tilde{B}}$ is, $\sqrt{\tilde{\gamma}} = l \sqrt{\tilde{q}}$. Rewriting

$$\Phi^{\tilde{x}} = \Phi^{\tilde{p}} \partial_{\tilde{p}} \tilde{x} = u^\dagger H A^{\tilde{p}} u l \sqrt{\tilde{q}} \partial_{\tilde{p}} \tilde{x} = \sqrt{\tilde{q}} \underbrace{u^\dagger H A^s u}_{\tilde{\Phi}^s}, \quad (4.79)$$

and expressing the time derivative of the energy as the sum of boundary surfaces integrals over the outward pointing fluxes $\tilde{\Phi}^s$ leads to

$$\partial_t E^2 = \int_{-1}^1 \int_{-1}^1 dA_{\tilde{y}\tilde{z}} \tilde{\Phi}^s \Big|_{\tilde{x}=-1}^1 + \int_{-1}^1 \int_{-1}^1 dA_{\tilde{x}\tilde{z}} \tilde{\Phi}^s \Big|_{\tilde{y}=-1}^1 + \int_{-1}^1 \int_{-1}^1 dA_{\tilde{x}\tilde{y}} \tilde{\Phi}^s \Big|_{\tilde{z}=-1}^1. \quad (4.80)$$

The area element is $dA_{\tilde{y}\tilde{z}} = \sqrt{\tilde{q}} d\tilde{y} d\tilde{z}$. The fluxes can be expressed in terms of incoming and outgoing characteristic variables at the boundary surface. The system is symmetric hyperbolic, therefore it has a full set of eigenvectors (see 4.1.1). With the transformation matrix, T_s^{-1} , the characteristic variables of the system are computed

as $v = T_s^{-1}u$. The flux expressed in the language of characteristic variables is,

$$\tilde{\Phi}^s = \underbrace{u^\dagger (T_s^{-1})^\dagger}_{v^\dagger} \underbrace{T_s^\dagger H T_s}_{\tilde{H}} \underbrace{(T_s)^{-1} A^s T_s}_{\Lambda_s} \underbrace{T_s^{-1} u}_v = v^\dagger \tilde{H} \Lambda_s v. \quad (4.81)$$

The diagonal matrix Λ_s contains all the speeds of the characteristic variables

$$\Lambda_s = \begin{pmatrix} \Lambda_I & 0 \\ 0 & -\Lambda_{II} \end{pmatrix}. \quad (4.82)$$

Here, the characteristic variables are ordered in such a way that all incoming with positive speeds Λ_I and outgoing with negative speeds $-\Lambda_{II}$ are grouped. In this partition it follows that

$$v = \begin{pmatrix} v_I \\ v_{II} \end{pmatrix}, \quad \tilde{H} = \begin{pmatrix} \tilde{H}_I & 0 \\ 0 & \tilde{H}_{II} \end{pmatrix}, \quad (4.83)$$

and with this

$$\tilde{\Phi}^s = v_I^\dagger \tilde{H}_I \Lambda_I v_I - v_{II}^\dagger \tilde{H}_{II} \Lambda_{II} v_{II}. \quad (4.84)$$

If all integrands in (4.80) are negative semi-definite, the energy of the system does not grow over time. For the boundary conditions the ansatz $v_I = \kappa v_{II} + g$ is used. This means that at the boundary surface the incoming characteristic variables are set equal to a linear combination of the outgoing characteristic variables plus some given data g . The triangle inequality gives

$$\tilde{\Phi}^s = (g^\dagger + v_{II}^\dagger \kappa^\dagger) \tilde{H}_I \Lambda_I (\kappa v_{II} + g) \leq g^\dagger H_I \Lambda_I g + v_{II}^\dagger \left[\kappa^\dagger \tilde{H}_I \Lambda_I \kappa - \tilde{H}_{II} \Lambda_{II} \right] v_{II}. \quad (4.85)$$

The first term only depends on the given data which can be chosen freely. The second can be made negative by choosing κ sufficiently small.

4.3.2 The semi-discrete case

In this subsection the energy estimate for the semi-discrete system is carried out. Of special interest is the question: *How can penalty terms at the boundary be used to control the energy in the subpatch?* Strictly speaking, the calculation is only true if the pseudospectral expansion is done using Legendre polynomials. In **bamps**

the more convenient Chebyshev polynomials are used. Nevertheless, it was empirically found that the values for the penalty parameters obtained by the following calculation lead to robust and stable patching boundaries in **bamps**.

The semi-discrete evolution equations are

$$\partial_t u_{\alpha\beta\delta} = A^p[\partial_p u]_{\alpha\beta\delta} = A^p[J_{\tilde{p}}^{\tilde{p}}]_{\alpha\beta\delta}[\partial_{\tilde{p}} u]_{\alpha\beta\delta}. \quad (4.86)$$

The energy of this system is defined using Gauss-Lobatto quadrature with the appropriate integration weights $\omega_\alpha, \omega_\beta, \omega_\delta$,

$$E^2 = \sum_{\alpha\beta\delta} \omega_\alpha \omega_\beta \omega_\delta \sqrt{\tilde{\gamma}}_{\alpha\beta\delta} u_{\alpha\beta\delta}^\dagger H u_{\alpha\beta\delta}. \quad (4.87)$$

Again the time energy of the system is computed. Defining $\tilde{\omega}_{\alpha\beta\delta} = \omega_\alpha \omega_\beta \omega_\delta [\sqrt{\tilde{\gamma}}]_{\alpha\beta\delta}$ and using the inverse product rule to write

$$\partial_t E^2 = \sum_{\alpha\beta\delta} \tilde{\omega}_{\alpha\beta\delta} \partial_p \left[u_{\alpha\beta\delta}^\dagger H_{\alpha\beta\delta} A^p u_{\alpha\beta\delta} \right]. \quad (4.88)$$

Transforming to local coordinates and assuming that $\partial_{\tilde{p}} \sqrt{\tilde{\gamma}}_{\alpha\beta\delta} = 0$ leads to

$$\partial_t E^2 = \sum_{\alpha\beta\delta} \omega_{\alpha\beta\delta} \partial_{\tilde{p}} \left[u_{\alpha\beta\delta}^\dagger H_{\alpha\beta\delta} A^p u_{\alpha\beta\delta} \sqrt{\tilde{\gamma}}_{\alpha\beta\delta} \right]. \quad (4.89)$$

Using the summation by parts property of the assumed expansion in Legendre polynomials gives

$$\begin{aligned} \partial_t E^2 = & \sum_{\beta\delta} \omega_{\beta\delta} u_{\alpha\beta\delta}^\dagger H_{\alpha\beta\delta} A^{\hat{x}} u_{\alpha\beta\delta} \sqrt{\tilde{\gamma}}_{\alpha\beta\delta} \Big|_{\alpha=0}^{N_x-1} + \sum_{\alpha\delta} \omega_{\alpha\delta} u_{\alpha\beta\delta}^\dagger H_{\alpha\beta\delta} A^{\hat{y}} u_{\alpha\beta\delta} \sqrt{\tilde{\gamma}}_{\alpha\beta\delta} \Big|_{\beta=0}^{N_y-1} \\ & + \sum_{\alpha\beta} \omega_{\alpha\beta} u_{\alpha\beta\delta}^\dagger H_{\alpha\beta\delta} A^{\hat{z}} u_{\alpha\beta\delta} \sqrt{\tilde{\gamma}}_{\alpha\beta\delta} \Big|_{\delta=0}^{N_z-1}. \end{aligned} \quad (4.90)$$

As in the continuum case the normal outward pointing s^i vector at the boundary is introduced to write

$$\begin{aligned} \partial_t E^2 = & \sum_{\beta\delta} \tilde{\omega}_{\beta\delta} u_{\alpha\beta\delta}^\dagger H_{\alpha\beta\delta} A^{\tilde{p}} [s_{\tilde{p}}^{\hat{x}}]_{\alpha\beta\delta} u_{\alpha\beta\delta} \Big|_{\alpha=0}^{N_x-1} + \sum_{\alpha\delta} \tilde{\omega}_{\alpha\delta} u_{\alpha\beta\delta}^\dagger H_{\alpha\beta\delta} A^{\tilde{p}} [s_{\tilde{p}}^{\hat{y}}]_{\alpha\beta\delta} u_{\alpha\beta\delta} \Big|_{\beta=0}^{N_y-1} \\ & + \sum_{\alpha\beta} \tilde{\omega}_{\alpha\beta} u_{\alpha\beta\delta}^\dagger H_{\alpha\beta\delta} A^{\tilde{p}} [s_{\tilde{p}}^{\hat{z}}]_{\alpha\beta\delta} u_{\alpha\beta\delta} \Big|_{\delta=0}^{N_z-1}, \end{aligned} \quad (4.91)$$

with $\tilde{\omega}_{\beta\delta} \equiv \sqrt{\tilde{q}}\omega_{\beta\delta}$. The flux is defined as

$$\tilde{\Phi}_{\alpha\beta\delta} = u_{\alpha\beta\delta}^\dagger H_{\alpha\beta\delta} A^P [s_p]_{\alpha\beta\delta} u_{\alpha\beta\delta}, \quad (4.92)$$

and the equations are transformed to characteristic variables in the obvious way. This gives for the semi-discrete case the analogue expression for the time derivative of the energy at the boundary. In case of patching the boundaries between two subpatches the penalty method is used to impose boundary conditions. For simplicity reason the following calculation is restricted to the $a = 0$ boundary. For each incoming characteristic variable a penalty term is added to the right hand side of the evolution equations

$$\partial_t u_{\alpha\beta\delta} = A^P [J_p^{\tilde{p}}]_{\alpha\beta\delta} [\partial_{\tilde{p}} u]_{\alpha\beta\delta} + \delta_{\alpha,0} [T_s]_{\beta\delta} P_{\beta\delta} \delta v_{\alpha\beta\delta}, \quad (4.93)$$

with the penalty matrix

$$P_{\beta\delta} = \begin{pmatrix} p_{\beta\delta} & 0 \\ 0 & 0 \end{pmatrix}, \quad (4.94)$$

and $\delta v_{\alpha\beta\delta} = [v^{BC}]_{\alpha\beta\delta} - [v_I^R]_{\alpha\beta\delta}$. The time derivative of the energy splits into two parts

$$\partial_t E^2 = \partial_t E_{\text{bulk}}^2 + \partial_t E_{\text{pen}}^2. \quad (4.95)$$

The first part is the contribution from the bulk

$$\partial_t E_{\text{bulk}}^2 = \sum_{\beta\delta} \tilde{\omega}_{\beta\delta} [v_I^\dagger]_{0\beta\delta} [\tilde{H}_I]_{0\beta\delta} [\Lambda_I^s]_{0\beta\delta} [v_I]_{0\beta\delta} - \sum_{\beta\delta} \tilde{\omega}_{\beta\delta} [v_{II}^\dagger]_{0\beta\delta} [\tilde{H}_{II}]_{0\beta\delta} [\Lambda_{II}^s]_{0\beta\delta} [v_{II}]_{0\beta\delta}. \quad (4.96)$$

The second part changes the time derivative of the energy because of the additional penalty terms in the evolution equation at the boundary

$$\partial_t E_{\text{pen}}^2 = \sum_{\beta\delta} \tilde{\omega}_{0\beta\delta} ([u_{0\beta\delta}]^\dagger H_{0\beta\delta} T_{0\beta\delta} P_{\beta\delta} \delta v_{0\beta\delta} + [\delta v_{0\beta\delta}]^\dagger P_{\beta\delta}^\dagger T_{0\beta\delta}^\dagger H_{0\beta\delta} u_{0\beta\delta}). \quad (4.97)$$

By inserting the identity $TT^{-1} = I$ into the appropriate places the state vector u is transformed to the vector of characteristic variables. Then multiplying out the

penalty matrix and rearranging leads to

$$\begin{aligned} \partial_t E_{\text{pen}}^2 &= \sum_{\beta\delta} p_{\beta\delta} \tilde{\omega}_{0\beta\delta} ([v^{BC}]_{0\beta\delta}^\dagger [\tilde{H}_I]_{0\beta\delta} [v^{BC}]_{0\beta\delta} \\ &\quad - [v_I]_{0\beta\delta}^\dagger [\tilde{H}_I]_{0\beta\delta} [v_I]_{0\beta\delta} - [\delta v]_{0\beta\delta}^\dagger [\tilde{H}_I]_{0\beta\delta} [\delta v]_{0\beta\delta}). \end{aligned} \quad (4.98)$$

In total the change of energy at the boundary surface is

$$\begin{aligned} \partial_t E^2 &= \sum_{\beta\delta} [v_I]_{0\beta\delta}^\dagger (\tilde{\omega}_{\beta\delta} \Lambda_I^s - p_{\beta\delta} \tilde{\omega}_{0\beta\delta}) [\tilde{H}_I]_{0\beta\delta} [v_I]_{0\beta\delta} - \sum_{\beta\delta} \tilde{\omega}_{\beta\delta} [v_{II}^\dagger]_{0\beta\delta} [\tilde{H}_{II}]_{0\beta\delta} [\Lambda_{II}^s]_{0\beta\delta} [v_{II}]_{0\beta\delta} \\ &\quad + \sum_{\beta\delta} p_{\beta\delta} \tilde{\omega}_{0\beta\delta} [v^{BC}]_{0\beta\delta}^\dagger [\tilde{H}_I]_{0\beta\delta} [v^{BC}]_{0\beta\delta} - \sum_{\beta\delta} p_{\beta\delta} \tilde{\omega}_{0\beta\delta} [\delta v]_{0\beta\delta}^\dagger [\tilde{H}_I]_{0\beta\delta} [\delta v]_{0\beta\delta}. \end{aligned} \quad (4.99)$$

Now two neighboring subpatches are considered. They are labelled L (for left) and R (for right) and have a common boundary at $a = N - 1$ for the left patch and $a = 0$ for the right patch. The change of energy in each subpatch is given by an expression as in equation (4.99). Setting the boundary conditions that the incoming characteristic variables of one subpatch have to be the outgoing one of the neighboring grid

$$v_{BC}^R \hat{=} v_{II}^L, \quad v_{BC}^L \hat{=} v_{II}^R, \quad (4.100)$$

and demand that the change of energy of the sub patches in time due to the patching boundary is not growing. Sufficient conditions for this are given by

$$p_{\beta\delta}^R = \frac{\tilde{\omega}_{\beta\delta} \Lambda_I^s}{\tilde{\omega}_{0\beta\delta}}, \quad p_{\beta\delta}^L = \frac{\tilde{\omega}_{\beta\delta} \Lambda_I^s}{\tilde{\omega}_{(N-1)\beta\delta}}. \quad (4.101)$$

These are the penalty parameters used in **bamps**. However, as previously mentioned, the actual discretization in **bamps** is made with Chebyshev rather than Legendre polynomials, which do not fulfill the needed summation-by-parts property. Furthermore the equations which are solved are not linear with constant coefficients and the Jacobians mapping from the master coordinates to our global Cartesian coordinates are not constant. As will be shown in the upcoming section 6, the implemented method is in an appropriate sense stable. However, these facts may contribute to the necessity of employing the filter (4.56).

5 Axisymmetric considerations

One of the disadvantages in the study of collapsing gravitational waves with the BAM code was the fact that 3d grids were employed to evolve axisymmetric data, making the simulations unnecessarily expensive and less accurate. In this section different considerations are presented for the case that axisymmetric spacetimes are evolved in `bamps`. First the Cartoon method [13] is discussed which is used to reduce the standard `bamps` 3d domains to a plane, by using the Killing vector to evaluate any angular derivatives. Then a detailed description of the formulation of the apparent horizon conditions in axisymmetry is given. Here, special care is taken on the regularity conditions on the symmetry axis. The apparent horizon search in the numerical data was implemented in a program called `AHloc`, which will also be discussed. Finally two types of axisymmetric, moment-of-time-symmetry initial data and their numerical construction are presented.

5.1 The analytic Cartoon method

Here the implementation of the so-called Cartoon method [13] for axisymmetry in the `bamps` code is discussed. Assuming that the 3d system is given in a Cartesian coordinate system x^i in which all variables are smooth, $T \in C^\infty$, the basic idea of the Cartoon method is to apply wherever possible the same coordinates and discretization that lead to stable evolutions in 3d. Hence the axisymmetrically reduced system is computed in Cartesian coordinates and with Cartesian tensor components, without adapting coordinates and thereby avoiding the coordinate singularity at the axis.

Concretely, the computational domain is chosen to be the xz -plane defined by $y = 0$. Partial derivatives ∂_x and ∂_z are computed as for the 3d system. What is missing are the points and the numerical data in the y -direction for the computation of ∂_y . However, the y -derivative can be obtained by invoking axisymmetry, since the fields in the $y = 0$, xz -plane determine the fields for $y \neq 0$ by the rotation symmetry. Similarly, it suffices to consider only the half-plane $x \geq 0$ and $y = 0$ while still using the same stencils for ∂_x and ∂_z as in 3d.

The Cartoon method was first introduced for a Cartesian BSSN [20, 73, 91] code using finite differencing [13]. The ∂_y derivative was computed by adding ghost points in the y direction, so that identical 3d stencils could be used for 3d and axisymmetric 2d calculations. For a spectral collocation method, the same could be done by populating a 3d spectral element by rotation. There would still be significant gains

in efficiency since only a 2d subset of a 3d spectral grid consisting of many patches needs to be populated. However, it is also possible to derive analytical formulas for ∂_y in terms of quantities in the $y = 0$ plane only, so this is clearly the preferred way to proceed. This was first implemented in [77], in that case for finite differences and the second order GHG system. For an arbitrary smooth tensor T , axisymmetry is given by the vanishing of its Lie derivative along the rotational vector, $\mathcal{L}_\phi T = 0$.

Off-axis, $x \neq 0$. In the following various tensor types of interest are considered, suppressing their t and z dependence. For a scalar it is

$$\partial_y u(x, 0) = 0. \quad (5.1)$$

The second derivative does not vanish in general. For vectors and covectors ($x \neq 0$) it is

$$\begin{aligned} \partial_y v^x(x, 0) &= -\frac{1}{x} v^y(x, 0), & \partial_y v^y(x, 0) &= \frac{1}{x} v^x(x, 0), \\ \partial_y w_x(x, 0) &= -\frac{1}{x} w_y(x, 0), & \partial_y w_y(x, 0) &= \frac{1}{x} w_x(x, 0). \end{aligned} \quad (5.2)$$

the derivative is equal to the components of the vector divided by radius, with x and y components interchanged. For a symmetric $(0, 2)$ tensor (say, the four-metric g_{ab}), at $y = 0$, $x \neq 0$ it is

$$\begin{aligned} \partial_y g_{tt} &= 0, & \partial_y g_{tz} &= 0, & \partial_y g_{zz} &= 0, \\ \partial_y g_{tx} &= -\frac{1}{x} g_{ty}, & \partial_y g_{ty} &= \frac{1}{x} g_{tx}, \\ \partial_y g_{xz} &= -\frac{1}{x} g_{yz}, & \partial_y g_{yz} &= \frac{1}{x} g_{xz}, \\ \partial_y g_{xx} &= -\frac{2}{x} g_{xy}, & \partial_y g_{yy} &= \frac{2}{x} g_{xy}, \\ \partial_y g_{xy} &= \frac{1}{x} (g_{xx} - g_{yy}). \end{aligned} \quad (5.3)$$

Some components behave like scalars, some like covectors, and some show the two terms occurring in the Lie derivative, which may result in a factor two due to symmetry.

On-axis, $x = 0$. Axisymmetry by itself does not imply differentiability on the axis, for example, $u(x, y) = \rho$. Axisymmetry and the condition that in Cartesian coordinates $T \in C^\infty$ are combined in two ways. First, consider parity under $(x, y) \rightarrow$

$(-x, -y)$, which corresponds to a rotation by π around the z -axis. Because of axisymmetry, it is $T(\rho, 0) = \pm T(-\rho, 0)$ and $\partial_y T(\rho, 0) = \mp \partial_y T(-\rho, 0)$. Since $\partial_y T$ is continuous, the limit $\rho \rightarrow 0$ exists. Hence for tensors that are even under this type of parity, the derivative vanishes, $\partial_y T_{even}(0, 0) = 0$. For tensors that are odd, the tensor vanishes, $T_{odd}(0, 0) = 0$, and $\partial_y T_{odd}(0, 0)$ is a regular, finite value. Therefore it is imposed that ∂_y vanishes on the axis for even quantities. The question is how the value for the odd quantities can be computed.

From vanishing of the Lie derivative, relations for the tensor components themselves can be obtained, but not for their derivative. For a scalar, there is no extra condition. Examples for relations obtained from (5.2)–(5.3) are

$$\begin{aligned} v^i(0, 0) &= 0, & w_i(0, 0) &= 0, \\ g_{tx}(0, 0) &= g_{ty}(0, 0) = g_{xz}(0, 0) = g_{yz}(0, 0) = 0, \\ g_{xy}(0, 0) &= 0, & g_{xx}(0, 0) &= g_{yy}(0, 0). \end{aligned} \tag{5.4}$$

Although some of the same information was obtained that has been already discussed for $(x, y) \rightarrow (-x, -y)$ parity, for even parity quantities with two or more indices there are additional relations. For the metric components these are related to covariance under rotation by $\pi/2$, or $(x, y) \rightarrow (-y, x)$.

To find the derivative ∂_y at $(0, 0)$, the l'Hopital's rule is used. Basically, in (5.2)–(5.3) the $\frac{1}{x}$ factors become a partial derivative in x because the other terms vanish. For example,

$$\partial_y v^x(0, 0) = -\partial_x v^y(0, 0), \quad \partial_y v^y(0, 0) = \partial_x v^x(0, 0). \tag{5.5}$$

Axisymmetry for partial derivatives of tensors. There also are objects like $\Phi_{iab} = \partial_i g_{ab}$, which are not tensors, but partial derivatives of tensors. The Lie derivative $\mathcal{L}_\phi \partial_i g_{ab}$ is in general not defined for non-tensors, and a priori it is not clear whether $\mathcal{L}_\phi \partial_i g_{ab} = 0$ implies axisymmetry. However, the required formulas can be derived by computing

$$\partial_i \mathcal{L}_\phi g_{ab} = \hat{\mathcal{L}}_\phi \partial_i g_{ab} + g_{cb} \partial_a \partial_i \phi^c + g_{ac} \partial_b \partial_i \phi^c, \tag{5.6}$$

where $\hat{\mathcal{L}}_\phi$ is introduced to collect those terms that correspond to the Lie derivative of a tensor, and the remaining terms are the deviation from the tensor formula. The last term in $\partial_i(\phi^c \partial_c g_{ab}) = \phi^c \partial_c \partial_i g_{ab} + \partial_c g_{ab} \partial_i \phi^c$ provides precisely the term that

would otherwise be missing in the sum over index locations in $\hat{\mathcal{L}}_\phi \partial_i g_{ab}$.

The key observation is that in the case of a *rigid* rotation in adapted coordinates generated by $\phi^a = (0, -y, x, 0)^T$, the second derivatives of ϕ^a vanish

$$\partial_a \partial_b \phi^c = 0. \quad (5.7)$$

Therefore, in this special case the correct result is obtained by using the tensor formula

$$\partial_i \mathcal{L}_\phi g_{ab} = \hat{\mathcal{L}}_\phi \partial_i g_{ab}, \quad (5.8)$$

as was also noted in [13]. This generalizes immediately to partial derivatives of arbitrary tensors, and also includes the case of the Christoffel symbol required for the BSSN or Z4c system, compare [13]. Eqn. (5.7) furthermore simplifies the computation of second derivatives.

5.2 Apparent horizons

Formulation of the AH conditions: An apparent horizon is a closed two surface in the spatial slice with expansion

$$H = D_i s^i - K + s^i s^j K_{ij} = 0, \quad (5.9)$$

where s^i is the unit normal to the surface. The approach to the apparent horizon search used in this work is based on that of [12] as also presented in [10, 103]. First given the spatial metric γ_{ij} and extrinsic curvature K_{ij} in Cartesian coordinates, they are transformed to work in spherical polar coordinates defined by

$$r^2 = x^2 + y^2 + (z - z_0)^2, \quad \theta = \arccos \left(\frac{z - z_0}{r} \right). \quad (5.10)$$

Here it is $\theta \in [0, \pi]$ and the z-axis is taken to be the symmetry axis. In axisymmetry without twist, the spatial metric and extrinsic curvature then takes the form

$$S_{ij} = \begin{pmatrix} S_{rr} & r \sin \theta S_{rT} & 0 \\ r \sin \theta S_{rT} & r^2 S_{\theta T} & 0 \\ 0 & 0 & r^2 \sin^2 \theta S_{\phi T} \end{pmatrix}, \quad (5.11)$$

in the $\phi = 0$ plane. Local flatness on the axis implies that the components $S_{rr}, S_{rT}, S_{\theta T}$ and $S_{\phi T}$ are even functions of θ around the symmetry axis, with $S_{\theta T} - S_{\phi T} \sim \theta^2$ around $\theta = 0$, and similar dependence around $\theta = \pi$. Working in the ρz plane an apparent horizon can be parametrized by the level set $s = 0$ of

$$s = r - F(\theta), \quad (5.12)$$

The apparent horizon condition (5.9) can be rewritten as a first order ODE system,

$$\begin{aligned} F' &= G, \\ G' &= (\sin^2 \theta \gamma_{rT}^2 - \gamma_{rr} \gamma_{\theta T}) F^2 L^2 q^{ij} (\Gamma^k_{ij} D_k s + L K_{ij}). \end{aligned} \quad (5.13)$$

for $F(\theta)$ and $G(\theta)$, where the unit spatial vector s^i and magnitude L are given by

$$s^i = \gamma^{ij} L D_j s, \quad L^{-2} = \gamma^{ij} (D_i s)(D_j s), \quad (5.14)$$

and $q_{ij} = \gamma_{ij} - s_i s_j$ is the induced metric in the level set. These expressions are evaluated in spherical polar coordinates. As noted elsewhere (for example in [10]) this parametrization is not completely general, only being sufficient if the apparent horizon is a ray-body containing the point z_0 . Regularity of an apparent horizon means that $G(0) = G(\pi) = 0$.

Search strategy: Given the metric and extrinsic curvature the search strategy for an apparent horizon is the following:

First, z_0, r_0 are chosen. From this point the ODE (5.13) is integrated from $\theta = 0$ to $\theta = \pi/2$, with initial conditions $F(0) = r_0$ and $G(0) = 0$. Simultaneously the ODE is integrated backwards from $\theta = \pi$ to $\theta = \pi/2$ taking as initial conditions $F(\pi) = r_0$ and $G(\pi) = 0$. If there is an apparent horizon the forwards (F^+, G^+) and backwards (F^-, G^-) solutions will satisfy,

$$\Delta F = F^+(\pi/2) - F^-(\pi/2) = 0, \quad \Delta G = G^+(\pi/2) - G^-(\pi/2) = 0. \quad (5.15)$$

This gives a non-linear root finding task on the function $S : \mathbb{R}^2 \rightarrow \mathbb{R}^2$ defined by

$$S(z_0, r_0) = (\Delta F, \Delta G). \quad (5.16)$$

One complication is that the ODE system (5.13) needs to be regularized on the

axis to impose the initial conditions. This is straightforwardly done by using the regularity conditions above, resulting in

$$G' = \left(\frac{\gamma_{\theta T}}{2\gamma_{rr}} - \frac{\gamma_{rT}}{2\gamma_{rr}} \right) F + \left(\frac{\partial_r \gamma_{\theta T}}{4\gamma_{rr}} - \frac{K_{\theta T}}{2\sqrt{\gamma_{rr}}} \right) F^2 \quad (5.17)$$

at $\theta = 0$ and similarly at $\theta = \pi$. To arrive at this expression the regularity condition $S_{\theta T} - S_{\phi T} \sim \theta^2$ has been used explicitly. The numerical implementation uses a transformation from Cartesian components, so this condition is automatically satisfied and instead the condition in a slightly more complicated form involving $\gamma_{\phi T}$ and $K_{\phi T}$ can be used.

The second step of the search is to iterate on (z_0, r_0) until a solution is found, or until the method fails. As an alternative strategy, it is normally proposed to integrate the ODE from $\theta = 0$ to $\theta = \pi$ then to perform a bisection search on $G(\pi)$. It was not possible to obtain satisfactory results this way because every surface except the apparent horizon itself diverges near $\theta = \pi$, making the bisection hopeless. Reasonable first guesses for z_0 would seem to be the position of the maximum of the Kretschmann scalar, or, if an apparent horizon was already found in a previous time-slice, the coordinate center of the previous horizon.

Horizon mass: In twist-free axisymmetry the apparent horizon mass M_H is related to the area of the apparent horizon A_H as,

$$M_H^2 = \frac{A_H}{16\pi}. \quad (5.18)$$

The area of the apparent horizon can be computed as a simple integral,

$$A_H = 2\pi \int_0^\pi L^{-1} \sqrt{\gamma} r^2 \sin \theta \, d\theta. \quad (5.19)$$

where the fact that the apparent horizon is a surface of revolution was used. Here γ is the determinant of the spatial metric in Cartesian coordinates.

Simplifying assumptions: In many simulations the focus is on finding apparent horizons centered at the origin in spacetimes that are additionally reflection symmetric about the $z = 0$ plane. In this case the root-finding search can be traded above for a bisection search by simply fixing $z_0 = 0$ and integrating the ODE (5.13) from $\theta = 0$ to $\theta = \pi/2$. Here the integration is started from different initial radii r_0 until points are found about which $G(\pi/2)$ changes sign. Then a bisection in r_0 is

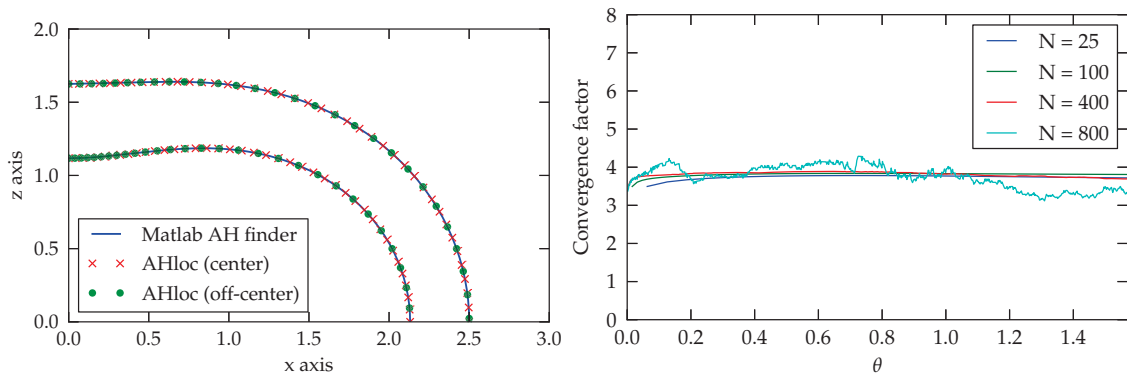


Figure 11: In the left hand panel the apparent horizon for a centered $A = 12$ Brill wave, as found by the apparent horizon finder `AHloc` and a bespoke Brill wave apparent horizon finder, are plotted. This data has been used as a standard test case elsewhere in the literature [12, 43]. The computed ADM mass is $M_{\text{ADM}} = 4.67$, which compares perfectly with $M_{\text{ADM}} = 4.67 \pm 0.01$ given in [12]. The horizon mass is $M_H = 4.66$, again in agreement with the literature. The right panel shows pointwise self-convergence labelled by $N = 25, 100, 400$ and 800 , with $N + 1$ being the lowest number of points in the series, and $2N + 1$ and $4N + 1$ points were used to make the plot. Very few points are needed to show clean convergence because the surface varies slowly in θ . This also means that one cannot reliably test convergence at high resolutions because the differences between the computed surfaces are essentially at the level of round-off.

carried out to find the apparent horizon, where $G(\pi/2) = 0$. Typically the criterion $G(\pi/2) < 10^{-8}$ to end the search is chosen. As in the more general case, if multiple such surfaces are found the outermost is taken as the apparent horizon.

Numerical implementation: In practice the apparent horizon search is carried out in the `AHloc` code as follows. During a `bamps` evolution the necessary components of the spatial metric and extrinsic curvature are outputted in the $y = 0$ plane at different coordinate times. For the integration of the ODE, various ODE integrators of the GSL [5] are used. To determine the apparent horizon accurately as fast as possible the *explicit embedded Runge-Kutta Prince-Dormand (8, 9) method* is chosen, a high-order adaptive step integrator. When convergence testing a simple fourth order Runge-Kutta integrator has been used. To evaluate the metric and extrinsic curvature at each point $(r = F, \theta)$ along the level set a barycentric Lagrange interpolation inside each `bamps` subpatch is carried out. For the root-finding again the GSL is used, now choosing one of the ‘hybrid’ algorithms that do not need the Jacobian of the system of equations being solved.

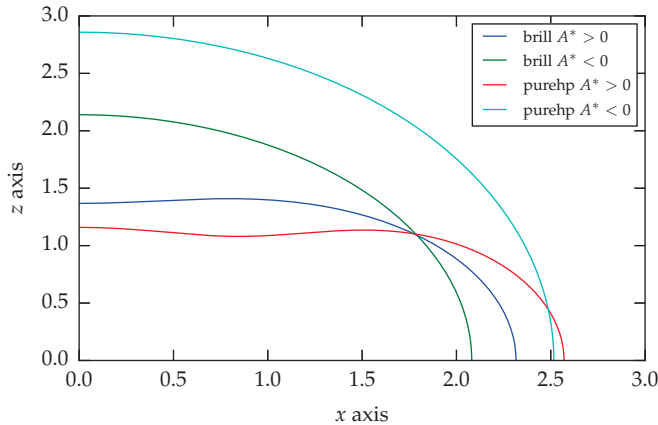


Figure 12: The apparent horizons for centered Brill data with $A = 11.82$ and $A = -5.3$ and for pure plus polarization data with $A = 2.381$ and $A = -2.28$.

5.3 Initial data

Brill wave data

Brill wave initial data has already been described in section 3.1. In the context of **bamps**, a pseudospectral elliptic solver is used to generate Brill initial data for evolutions. The method is discussed in section 5.3. In this section the results of the apparent horizon search with AHloc is presented. In the positive amplitude Brill data, an apparent horizon can first be found at $A = 11.82$ with horizon mass $M_H = 4.8$, which is in agreement with earlier work by [12]. This comparison was also taken as a standard testcase for the apparent horizon finder. On the left, Fig. 11 shows the found horizons for this case. For geometrically oblate data an apparent horizon can first be found at $A = -5.30$ with mass $M_H = 4.4$. This horizon is plotted in Fig. 12.

Pure plus polarization wave data

Metric ansatz: Observers distant from a compact object see gravitational waves in the form

$$d\tilde{l}^2 = dr^2 + r^2(1 + h_+)d\theta^2 + r^2 \sin^2 \theta(1 - h_+)d\phi^2 + 2r^2 \sin \theta h_\times d\theta d\phi, \quad (5.20)$$

with the wave polarizations h_+ and h_\times small perturbations of the Minkowski metric. This suggests modifying the ansatz (3.1) to

$$d\tilde{l}^2 = dr^2 + r^2(e^{2q}d\theta^2 + e^{-2q} \sin^2 \theta d\phi^2), \quad (5.21)$$

so that if the seed function is chosen to be small and centered far from the origin the initial data will represent a pure plus polarization gravitational wave. One could similarly make an ansatz for pure cross polarization waves, or indeed make other choices completely like [92] which have also been implemented and tested.

The constraints: Starting with moment of time symmetry initial data, the remaining constraint takes the form

$$\tilde{\Delta}\Psi = \frac{1}{8}\Psi\tilde{R}. \quad (5.22)$$

The conformal Ricci scalar is

$$\tilde{R} = \frac{2}{r^2}[e^{-2q} - 1 - (r\partial_r q)^2] - \frac{1}{r^2\sin^3\theta}\partial_\theta(\sin^3\theta\partial_\theta e^{-2q}), \quad (5.23)$$

and the Laplacian of the conformal metric is

$$\tilde{\Delta}\Psi = \frac{1}{r^2}\partial_r(r^2\partial_r\Psi) + \frac{e^{2q}}{\sin^2\theta}\partial_\theta(e^{-2q}\sin^2\theta\partial_\theta\Psi). \quad (5.24)$$

Once more the obvious boundary conditions for asymptotic flatness at spatial infinity are imposed. The seed function is chosen to be

$$q(r, \theta) = A r^4 \sin^2 \theta e^{-[r^2 - 2r\rho_0 \sin \theta + \rho_0^2]}, \quad (5.25)$$

which makes the conformal metric regular on axis.

Apparent horizons: Taking centered data with $A < 0$ an apparent horizon is first found at around $A = -2.28$, with mass $M_H = 5.47$. Looking for apparent horizons in centered data when $A > 0$, the curious result was found that there is a region $[2.381, 2.568]$ in which apparent horizons are first found. In the range $[2.569, 3.006]$, the data again seemed to be horizonless. Continue at $A = 3.007$ horizons were found again up to $A = 3.750$ where the search was stopped. The resolution of the search was $\Delta A = 0.001$. A closer look at the data at the boundaries of the ‘horizonless’ region shows that the shape of the horizon is very nearly not a ray-body, and it is expected that the method used simply cannot find the horizons in this range of amplitudes. Very likely this could be remedied by implementing an offset in ρ in the parametrization of the surface similar to that in z which is already implemented. However, this is left for further improvements in the future. The first apparent horizon for this data, found at $A = 2.381$, is plotted in Fig. 12. It has a

mass of $M_H = 4.8$.

Solving the constraints

Compactified coordinates: To solve for moment of time symmetry initial data, the spatial metric is written in spherical polar coordinates (r, θ, ϕ) , and compactified in the radial coordinate, resulting in coordinates (A, θ, ϕ) . The compactification is defined either by,

$$r = \frac{m A}{2(1 - A)}, \quad (5.26)$$

as suggested in [16], and used in [63] in the same elliptic solver employed here, or

$$r = \frac{m A}{2(1 - A^2)}, \quad (5.27)$$

similar to that employed for example in [33]. The parameter m partially controls the rate of compactification, but in either case spatial infinity corresponds to $A = 1$.

Numerical solution: A Chebyshev discretization is employed in the radial A direction, and a Fourier grid in the angular directions. Since the Hamiltonian constraint in this context is linear, solving the constraints amounts to a matrix inversion. With the particular method used in this work it was found that the choice (5.26) leads slightly worse constraint violations at a fixed resolution. One cause for this could be that the coordinates (5.26) are irregular at the origin.

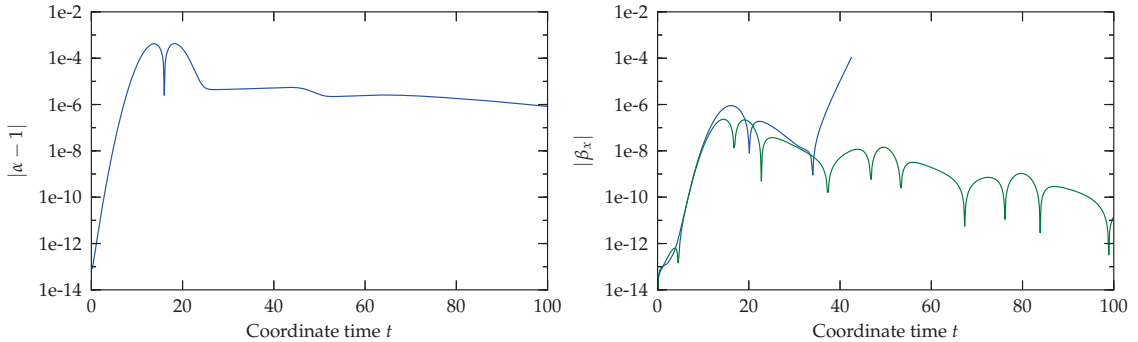


Figure 13: The left panel plots $|\alpha - 1|$ in the outer boundary as a function of time for a evolution of a gauge pulse on flat space, initially centered at the origin. The coordinates eventually seem to settle on, or very close to Minkowski slices. The right panel plots the magnitude of the shift in the outer boundary using the harmonic damped wave gauge to evolve the same gauge pulse with either the gauge boundary condition (4.32) or (4.33). In the former case the shift rapidly grows, causing the code to crash.

6 Code validation

In this section a set of numerical experiments is presented, performed in order to test the code and to obtain an optimal setup for the gravitational wave collapse simulations that follow later in this work. These tests include evolutions with the proposed boundary conditions, runs comparing the fully 3d, octant symmetry and Cartoon evolutions, as well as convergence and performance tests.

6.1 Gauge boundary

Gauge wave initial data: Minkowski spacetime is evolved with a perturbation initially placed in the lapse, so that

$$\alpha(t = 0) = 1 + A e^{-[x^2+y^2+z^2]/\sigma}. \quad (6.1)$$

In the following set of experiments it is $A = 0.01$ and $\sigma = 10$, with a fixed grid setup. The standard GHG formulation used in the SpEC code, namely $\gamma_0 = -\gamma_1 = \gamma_2 = 1$, and $\gamma_4 = \gamma_5 = 0$, is employed. The outer boundary is set to a coordinate radius of $r = 16$. The evolutions are carried out in 3d with octant symmetry imposed.

Harmonic gauge: Starting with the pure harmonic gauge $H_a = 0$, the outgoing gauge wave is harmlessly absorbed using either the gauge boundary condition (4.32) or (4.33). At the particular resolution and grid-setup that is chosen for this test, the

harmonic constraint violation at the end of the evolution, at $t = 100$, is around 10^{-14} and shows no sign of increasing with either choice of gauge boundary condition. The difference between the results with the two gauge boundary conditions is rather small, the maximum difference in the shift being around 10^{-7} at the end of the run. But here the initial pulse is very weak, and this is of no concern. In the left panel of Fig. 13 the quantity $|\alpha - 1|$ in the outer boundary is shown to demonstrate how the coordinates settle down.

Generalized harmonic gauge: Switching now to use the generalized harmonic gauge condition (4.11) with $\eta_L = 0.4, p = 1$ and $\eta_S = 6$. Using then the gauge boundary condition (4.32) the shift starts to grow at the boundary, and the numerics fail at $t \sim 42$. This behavior is perhaps not surprising given the large damping coefficients and the understanding obtained for the constraint preserving subsystem with damping in section 4.1.2. The gauge source functions have the same effect on the gauge as the damping terms on the constraints, namely they cause reflections from the boundary. It is expected that this will be suppressed as the outer boundary is placed further out so that the gauge sources are smaller where the boundary condition is applied. Using instead the gauge boundary conditions (4.33) this growth is completely absent. This behavior is demonstrated in the right panel of Fig. 13 where one sees the magnitude of the shift vector in the outer boundary in each case. With the gauge boundaries (4.33), at the end of the run the harmonic constraint violation C_x is around 10^{-14} and appears not to be growing. Looking at the shift however, it does seem that some further improvement may be possible in the future, as its peak lies at the outer boundary, with a value around 10^{-11} .

6.2 Constraint experiments

Simplified subsystem: Some of the experiments of the previous section are now repeated with the choice $\gamma_4 = \gamma_5 = 1/2$, and with different choices of γ_0 , using always the gauge boundary condition (4.33). With the pure harmonic gauge $H_a = 0$, the constraint violation at $t = 100$ is again around 10^{-14} if taken $\gamma_0 = 1$, and slightly larger, but still less than 10^{-13} in the case $\gamma_0 = 0.02$, the value suggested by the experiments in [Wey1] for a related formulation. Moving to the generalized harmonic choice (4.11) once more, again the violation at the end of the experiment is of the same order as when using the pure harmonic gauge. The result is plotted in Fig. 14. These results may not be representative when evolving different initial data, but cautiously $\gamma_4 = \gamma_5 = 1/2$ and $\gamma_0 = 1$ are taken as the default setting

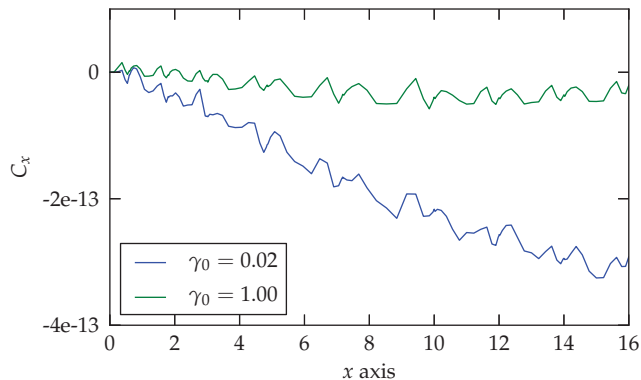


Figure 14: The plot shows the C_x component of the harmonic constraint along the x at time $t=100$ for two different choices for the constraint damping parameter γ_0 in the evolution of a gauge pulse on flat-space as in Fig. 13. The formulation parameters have been set to $\gamma_4 = \gamma_5 = 1/2$ and the generalized harmonic gauge has been used. On this basis $\gamma_0 = 1, \gamma_4 = \gamma_5 = 1/2$ are taken as the standard choice in `bamps`.

for the following work. Periodically different other choices are tested, most often playing with γ_0 in such experiments.

Constraint preserving conditions: The same experiments, with the generalized harmonic gauge and the new default formulation parameters, are repeated with changing to the alternative constraint boundaries (4.40) or (4.46). The constraint violation throughout the evolutions is very similar to the initial choice (4.29). Although initially the violation with the reflection reducing condition is slightly smaller than with the ‘geometric’ condition, later on there is practically nothing to choose between them. Considering that the violations are in the round-off regime 10^{-14} it is hard to judge from this experiment which of the conditions behaves most favorably.

6.3 Lapse power in constraint damping

Setup and initial data: A centered Brill wave with amplitude $A = 2.5$ is evolved. This data is subcritical and has a ADM mass of $M_{\text{ADM}} = 0.19$. The same grid setup as in the previous section is used, but with a slightly higher resolution (19^3 rather than 15^3 points per cube). It is $\gamma_0 = 0.2\alpha^l$ with $l = 0$, the standard choice elsewhere, or $l = -1$, a modification which might reduce constraint growth in the strongest field region. As above, the generalized harmonic gauge (4.11) is used. At the outer boundary the gauge boundary condition (4.33) is imposed.

Basic dynamics: The Kretschmann scalar initially has a peak at the origin, evaluated around 2300 on the `bamps` grid, slightly less than in the previous study of

section 3 and [Wey2]. This peak oscillates at the origin, peaking after an initial bounce with value around 500. The feature then rapidly propagates away and by a coordinate time $t = 10$, the peak value on the grid is less around 10^{-2} . The lapse initially decreases at the origin, this feature then propagating out to the outer boundary, behind which the lapse drifts back towards its initial value, unity.

Constraint violation: Examining the C_x constraint for the $A = 2.5$ data along the x -axis, only very small differences in the constraint violation between the $l = 0$ and $l = -1$ evolutions can be observed. The small differences are not surprising because the lowest value the lapse function takes is around 0.78 having started from 1. The peaks of the C_x constraint in the $l = -1$ evolution are about 2-5% smaller than in the $l = 0$ run. Increasing the amplitude of the initial data to $A = 4$, one might expect the improvement to be more significant as the lowest value of lapse decreases to 0.37, but the difference still amounts to between 2-5% at the peaks of the violation.

6.4 BAM vs. bamps comparison

Another validation strategy for **bamps** is to compare the numerical results with those of an independent code. For this again the BAM [28] code is used, evolving identical initial data with the same gauge conditions. In this comparison a centered $z_0 = 0$ Brill wave with $A = 1$ is evolved. This weak amplitude is chosen because evolving the Brill data accurately with BAM rapidly becomes expensive as A increases in magnitude. For the gauge either pure harmonic slicing $\eta_L = 0$ with either harmonic shift $\eta_S = 0$ or the damped harmonic shift $\eta_S = 1$ is used. Note that in this test neither the spherical shells nor the constraint preserving boundary conditions of [64] have been used. Since the outer boundaries were placed at $x = y = z = 12$, the solutions to the continuum PDEs being solved are not identical. Therefore there is not much hope for perfect agreement for long. Fig. 15 shows the spatial metric component γ_{xx} at $t = 1.625$, when the agreement is still very good for either choice of the shift, being practically indistinguishable by eye. In practice the main source of disagreement at the resolution of these runs comes from mesh-refinement boundaries in the BAM grid setup.

6.5 Octant and Cartoon

Initial data and grids: To test the implementation of symmetry reduced expressions, either octant, Cartoon, or their combination, weak $A = 1$ centered pure

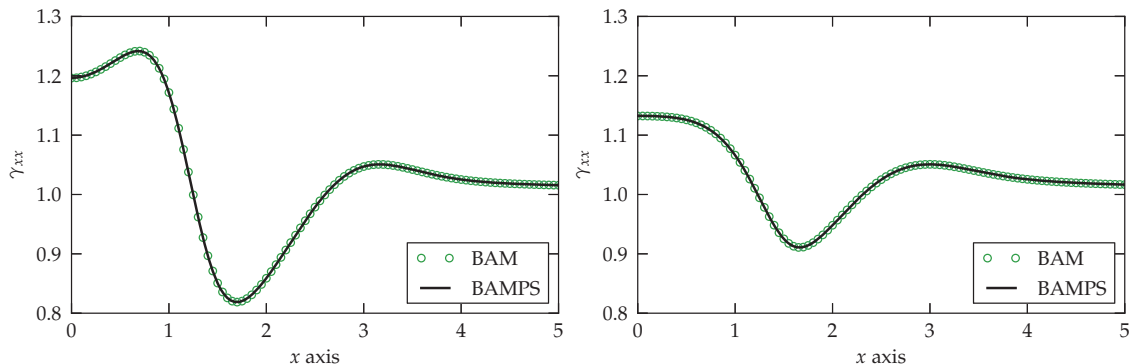


Figure 15: Comparison of the results of a Brill wave $A = 1$ evolution with BAM and `bamps`. Shown are snapshots of the metric component γ_{xx} along the x axis at $t = 1.625$. In the left panel the pure harmonic gauge was used, on the right the damped wave gauge with $\eta_L = 0$ and $\eta_S = 1.0$. The results of the codes are in good agreement in either case.

plus polarization initial data, as described in section 5.3, is evolved. Once again the generalized harmonic gauge (4.11) and the gauge boundary condition (4.33) are used. The starting point was a base cubed-ball 3d grid with $N = 15$ points per direction, and the number of subpatches derived from $\mathcal{N}_{\text{cu}} = 5$, $\mathcal{N}_{\text{cs}} = 4$ and $\mathcal{N}_{\text{ss}} = 3$. The outer boundary was placed at $r = 12$ in the units of the code. For ease of comparison, the breakdown of the grids was:

	$\mathcal{N}_{\text{cu}}^{\text{total}}$	$\mathcal{N}_{\text{cs}}^{\text{total}}$	$\mathcal{N}_{\text{ss}}^{\text{total}}$	$\mathcal{N}^{\text{total}}$	N^{total}
3d	125	600	450	1175	4×10^6
octant	27 (12, 6, 1)	48 (48, 12)	81 (36, 9)	216	5×10^5
Cartoon	25	80	60	165	4×10^4
cart. oct.	9 (4, 1)	24 (8)	18 (6)	51	10^4

The numbers in parentheses denote the number of those grids that were cut in half (at the axis) once, twice, or three times respectively, for the 3d grids, and once or twice for the Cartoon grids. Note that the current non-octant Cartoon implementation is not optimal because the whole x - z plane is evolved, wasting effectively a factor of two. Currently the code is most often used in Cartoon octant mode, so fixing this does not have a high priority. Looking at the table the main observation is that the expected reduction factor of eight (four) in the total number of grid points is present between the 3d (Cartoon) and octant grids, but that this number is not so closely reflected in the grid breakdown, where only a factor six (three) in the total number of grids is reached. This is obviously because there are many grids

with fewer points. Since the parallelization does not take this fact into account, it is possible that one MPI process is given *all* non-cut grids, and so it cannot be expected that the speedup rate is determined to a large extent by ratio in the number of grids. As the domain is made larger the relative number of cut grids decreases, so asymptotically the full speedup factors of eight or four might be attained.

Basic dynamics: Although irrelevant for the octant Cartoon comparison, since these data has not been used before, a brief description of their evolution is given here. Initially the peak of the Kretschmann scalar occurs at $\rho = \pm 0.65$ with a value 1.18. This profile then oscillates about three times at the origin, attaining a peak value of 7.25 before rapidly dispersing. Looking at the lapse the familiar behavior that at the origin it oscillates slightly before presenting a longer decrease, although at the minimum is only 0.995, having started from $\alpha(t = 0) = 1$ everywhere. Afterwards this pulse propagates out, roughly following the disturbance in the Kretschmann. Looking at the shift component β^x along the x -axis, early on there is a growth which peaks at $x = 1.06$, with value 0.0027. The development of the shift looks more like a slowly oscillating standing wave than a localized propagating feature.

3d, octant, Cartoon and octant-Cartoon comparison: Taking first the 3d and octant evolutions, the agreement throughout the evolution is nearly perfect. There are small differences however, starting from the beginning of the simulation at the level of round-off; differences of 10^{-15} in metric components, which slowly drift as the evolution goes on. This behavior is expected because the derivative approximation differ at this level. Similar differences were found between the other setups. These differences are never larger than the constraint violation, in for example C_x . The convergence (see section 6.6 for more discussion) with each setup has been tested, although not for this data, with no indication of a problem. For the speed comparison the code has been run with each setup on 24 cores (with hyper threading) of our local cluster *Core12* with Intel Xeon X5650 processors. The octant run was a little more than 6 times faster than the 3d run, as expected given the foregoing discussion. The octant Cartoon run was about 2.4 times faster than the pure Cartoon test, which is a little disappointing. Going from $\mathcal{N}_{ss} = 3$ to $\mathcal{N}_{ss} = 6$ radial subdivisions in the outer shells, this value increases to 2.9, demonstrating the expected dependence. Comparing the full 3d and octant Cartoon runs, there was a gratifying speed up of nearly a factor 400.

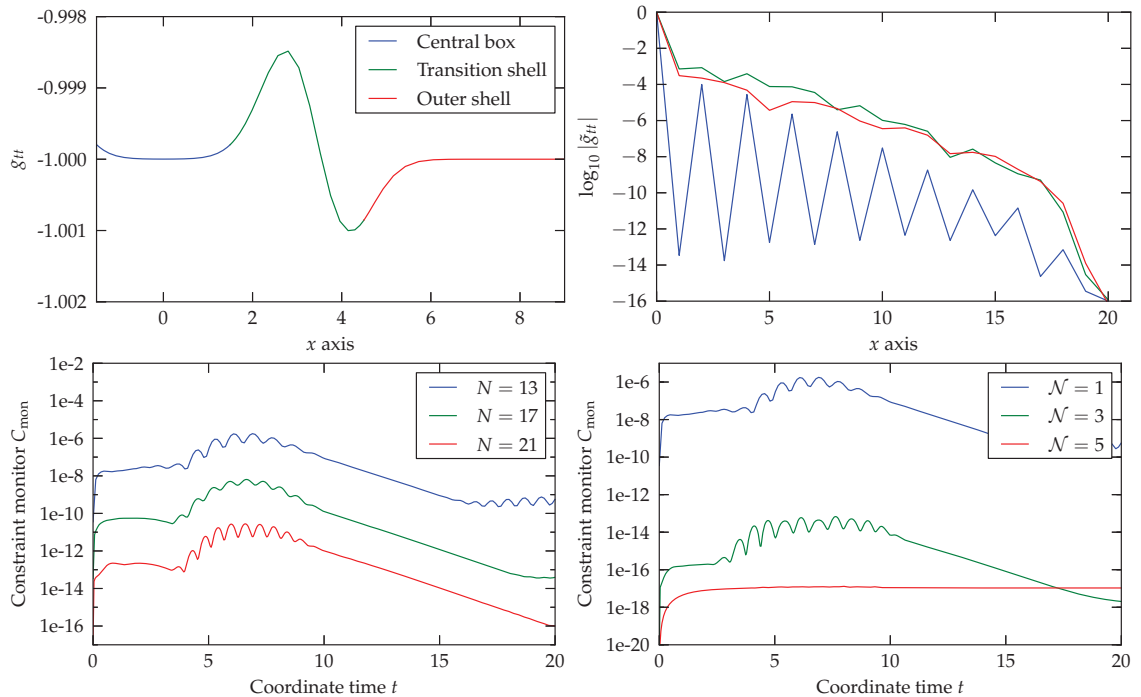


Figure 16: Evolution of a gauge wave with $A = 0.01$ and $\sigma = 1.0$. In the upper panels a spatial resolution of $N = 21$ is used on a grid with $\mathcal{N} = 1$ subpatches. The upper left panel gives a snapshot of g_{tt} along the x axes at $t=3.55$. The upper right shows the Chebyshev expansion coefficients at the same time with the same color coding. The lower panels show convergence of the constraints for the same initial data; on the left the number of points N in each grid, on the right the number of subpatches \mathcal{N} is increased.

6.6 Convergence

The numerical method of **bamps** allows two options for increasing resolution. The first is to add grid-points in every domain, the second is to subdivide grids further, keeping the number of points inside each subpatch fixed. Given fixed finite computational resources it is not obvious what is the optimum strategy to achieve the smallest possible error, because although adding points might give spectral convergence, it also comes with a N^{-2} dependence in the allowed time-step, whereas on the other hand, as presented shortly, adding more subpatches allows the code to scale up to a large number of processors. Probably the optimal strategy relies on a balance between each. To examine the effect of each strategy in the simplest possible way, gauge wave initial data on the Minkowski spacetime is evolved. It is set up by choosing $\alpha = 1 + A \exp[-(r/\sigma)^2]$, $\beta^i = 0$, with $r = \sqrt{x^2 + y^2 + z^2}$ as usual, and otherwise the flat spatial Cartesian metric and vanishing extrinsic curvature. The

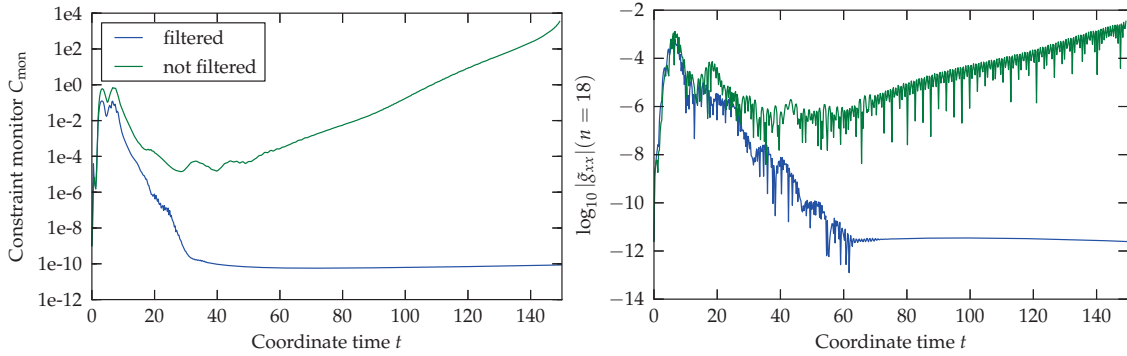


Figure 17: Influence of the filter at example of a $A = 1$ Brill wave evolution. On the left the time evolution of the constraint monitor C_{mon} is shown. In the simulation using a filter the constraint violation settles down to 10^{-10} . Without using a filter the constraint violation grows and leads to a failure of the simulation at $t \approx 150$. On the right the evolution of the fourth highest Chebyshev expansion coefficient is shown. It is the highest mode which is not affected by the filter. Without the filter the high frequencies grow over time and cause the simulation to fail. The filter sets the highest frequency to zero which avoids the growth of the high frequency modes.

results are plotted in the four panels of Fig. 16 and confirm the expectations.

6.7 Filtering

To demonstrate the necessity of the filter (4.56) a centered $A = 1$ Brill wave is evolved. The results are plotted in Fig. 17. The left panel shows that without filtering the constraint violation starts to grow exponentially in time, whereas with filter the growth is completely absent and the norm of constraints remains steady at a very low value. The right panel plots the magnitude of the fourth highest spectral coefficient of g_{xx} in the transition shell as a function of time. This coefficient is the first that is directly unaffected by the filter. It shows that the growth in the constraints seems to be associated with an explosion in the higher spectral coefficients. Interestingly the same experiment was repeated with gauge wave initial data, and this effect was not observed, at least in the same time-frame. It is expected that the same behavior would manifest if evolved for long enough. The obvious conclusion drawn from this is that it is important to test these methods with several data types to get a reliable picture of their properties.

6.8 Performance

Profiling: To evaluate the performance of the code, simple timing functions have been used throughout an evolution on a grid with $N = 21$ points per cube and $\mathcal{N} = 1$ subpatches running in serial mode. For this test all output has been switched off, but obviously in production runs the amount of time spent there is determined by the user. Thus care is needed in balancing output against performance. Particularly expensive in the context of collapse simulations is the data necessary for the apparent horizon searches, which requires 2d output of the spatial metric and extrinsic curvature. The result of this test is plotted in Fig. 18. Very little time was spent in the ‘analyze’ routines, which compute the auxiliary quantities needed in postprocessing, such as the constraints, the Kretschmann scalar, or in principle gravitational wave-forms. This is determined by the user, but in this case the small 1% value is likely to be representative because the ‘analyze’ routines are called very rarely, roughly every ~ 50 timesteps. Calling the filter should cost as much as computing derivatives once, since it involves matrix multiplication for each direction. Since this is done only at the end of each full time-step it seems reasonable that the computation is dominated by the ‘evolve’ function, which contains the time sub-steps. The evolve step is divided primarily between the boundary computation ($\sim 10\%$) and evaluating the equations of motion ‘right hand side’ ($\sim 90\%$). The boundary timer includes both the time spent computing the outer boundary and that in interpatch communication. It is perhaps surprising that so much time is spent on the boundaries, given the lower dimensionality of the surfaces, but of course this value depends on the particular grid being computed. When running with MPI, network communication is required in this part of the code so it is in danger of becoming the bottleneck. But representative MPI experiments show that the time spent in ‘boundaries’ decreases to about 4%, because grids with more points have been used. Therefore network communication is unlikely to prevent scaling of the code. In the serial test there are a total of 120393 points in the domain vs. 34398 in the boundaries. The outer boundary computation is expensive because of the evaluation of the number of operations needed to evaluate the constraints (4.29) and the incoming curvature characteristics (4.30). Finally the ‘right hand sides’ are split between computing derivatives and the algebra necessary to evaluate the equations of motion, most of which is spent computing the former. This also suggests a starting place for optimizing the code further in the future.

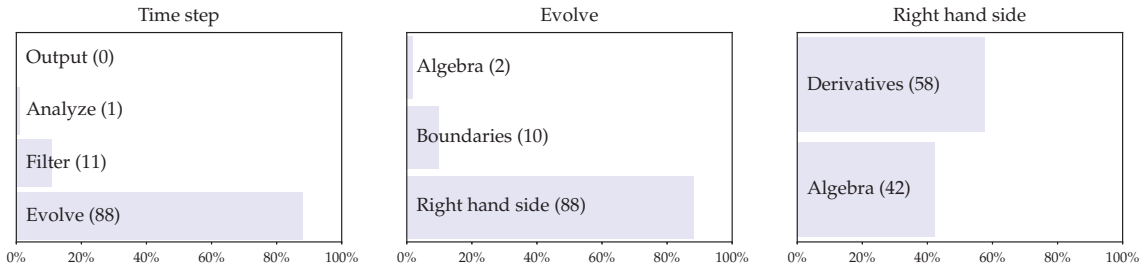


Figure 18: Relative time spent in different parts of **bamps** during GHG evolution in serial mode. Within one timestep the dominant part is the evolution routine where almost 90% of the time is spent. The evolution routine is further divided, and spends time evaluating the right-hand-sides. The right-hand-sides are split roughly equally between computing derivatives and pure algebra.

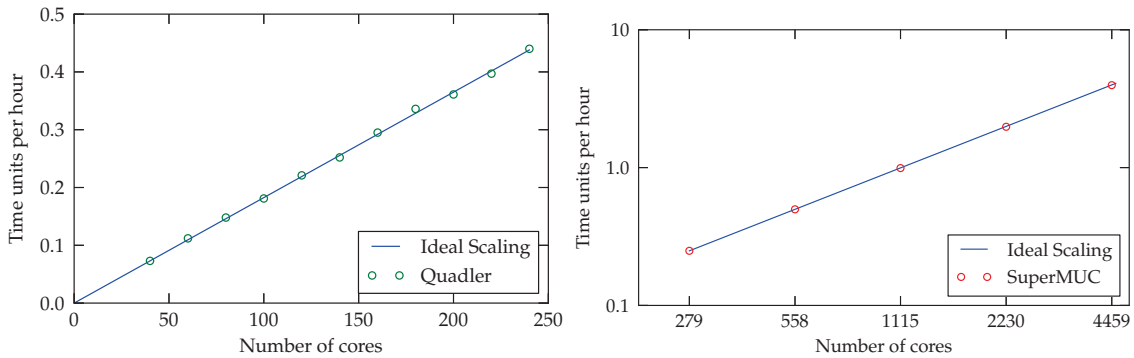


Figure 19: Strong scaling of **bamps**. On the left the scaling behavior on the local *Quadler* cluster is shown. For this a grid with $\mathcal{N} = 3$ was used. In total this grid consists of 1625 patches. The plot on the right shows the strong scaling of a grid with $\mathcal{N} = 5$ on the *SuperMUC* cluster. Here a grid with $\mathcal{N} = 5$ sub patches was used. In total this grid consists of 4459 patches.

Strong-scaling: The current **bamps** parallelization strategy is to obtain perfect scaling using many subpatches, and splitting these subpatches across many processors. The key is that, in contrast to buffer zones required in the decomposition of a finite differencing grid, only 2d surfaces of points need to be passed by network communication, making the relative time spent there negligible. In a finite differencing approach the relative size of the buffer zones decreases with resolution, but in practice it can still be significant in production runs, especially when higher order stencils are applied. Fig. 19 presents strong scaling plots performed on local resources, the *Quadler* cluster with Intel Xeon E5430 processors, and on the *SuperMUC* cluster located in LRZ Garching, with Intel Xeon E5-2680 8C processors. In each test the code was run in 3d. In the former a grid with 1625 patches in total was set up, dividing these amongst the available cores; perfect scaling can be observed.

Since the first test is for a small number of processors, in the latter a grid with a total of 4459 subpatches was set up. The number of cores used was increased until one patch was assigned per core. Again perfect scaling was observed. On the other hand `bamps` is currently not parallelized whatsoever at the subpatch level, which means that the maximum number of points per subpatch is in principle determined by the amount of memory available to one core. At least when running the code in Cartoon mode however, in practical terms this does not seem to be problematic. Instead the N^{-2} restriction in the time step makes increasing the number of points infeasible long before being close to filling the available memory. In 3d this may no longer be the case.

7 Evolution of single blackholes with bamps

The main thrust of the **bamps** development has been towards treating collapsing axisymmetric gravitational waves accurately. For super-critical data the cubed-ball grid is unsuitable after the formation of an apparent horizon. Therefore the strategy for long-term evolution is to take the data and interpolate onto a cubed-shell (excision) grid, with the excision surface suitably positioned, changing the lapse and shift to be sure that the excision surface is a true outflow boundary. A necessary requirement for this is to treat a single blackhole, which will be discussed here.

7.1 Initial data

Kerr-Schild coordinates: A Schwarzschild solution in Kerr-Schild coordinates was evolved as was done in [27] where a preceding version of the **bamps** code was used. Although the current numerical method is not particularly close to that used previously, some components of the older code were inherited. Importantly evolving this data allows a simple comparison with the previous method and results. In spherical polar coordinates the metric and extrinsic curvature takes the form

$$g_{ab}dx^a dx^b = -\left(1 - \frac{2M}{r}\right) dt^2 + \frac{4M}{r} dt dr + \left(1 + \frac{2M}{r}\right) dr^2 + r^2 d\Omega^2, \quad (7.1)$$

with $d\Omega^2$ the flat metric on the two-sphere, and

$$K_{ij}dx^i dx^j = -\frac{2M}{\sqrt{1 + \frac{2M}{r}}} \left[\frac{1}{r^2} \left(1 + \frac{M}{r}\right) dr^2 - d\Omega^2 \right], \quad (7.2)$$

respectively. Inside the code the line-element is written in Cartesian coordinates in the standard way. More discussion of Kerr-Schild coordinates can be found in [40, 72].

Harmonic Killing coordinates: Evolutions starting from the harmonic Killing slicing described in [41], serve as a convenient starting point when transitioning from one generalized harmonic gauge to another. For this initial data, in spherical polars, the metric and extrinsic curvature are

$$g_{ab}dx^a dx^b = -\left(1 - \frac{2M}{r}\right) dt^2 + \frac{8M^2}{r^2} dt dr + \left(1 + \frac{4M^2}{r^2}\right) \left(1 + \frac{2M}{r}\right) dr^2 + r^2 d\Omega^2, \quad (7.3)$$

and

$$K_{rr} = -\frac{4M^2}{r^6} \frac{4M^3 + 4M^2r + 3Mr^2 + 2r^3}{\sqrt{1 + \frac{2M}{r}} \sqrt{1 + \frac{4M^2}{r^2}}}, \quad K_{\theta\theta} = \frac{4M^2r^2}{\sqrt{1 + \frac{2M}{r}} \sqrt{1 + \frac{4M^2}{r^2}}}, \quad (7.4)$$

with the remaining components vanishing. For this data spatially harmonic coordinates are obtained by building Cartesians according to

$$x = (r - M) \sin \theta \cos \phi, \quad y = (r - M) \sin \theta \sin \phi, \quad z = (r - M) \cos \theta, \quad (7.5)$$

The resulting metric has a coordinate singularity at $r = M$, with r implicitly defined in the obvious way from the new coordinates. The coordinate singularity is not a principle problem as the excision surface can be pushed outside this radius. But `bamps` relies on standard Cartesian coordinates in several places. So in the code one could transform in the standard way but then choose the gauge source function

$$H^a = 2(\tilde{J}\partial\tilde{J})^{(ab)}{}_b. \quad (7.6)$$

with $J^a{}_{a'}$ the Jacobian between the standard a -index Cartesians and harmonic Cartesian a' index coordinates (7.5), the compound object $(\tilde{J}\partial\tilde{J})$ is defined by,

$$(\tilde{J}\partial\tilde{J})^a{}_{bc} = (\tilde{J}^{-1})_b{}^{a'} \partial_c \tilde{J}^a{}_{a'}. \quad (7.7)$$

with $\tilde{J}^a{}_{a'} = \sqrt{|J|} J^a{}_{a'}$ and where indices are manipulated in the obvious way with g_{ab} to obtain (7.6). Instead the gauge source function is just chosen to be fixed at its initial value, as will momentarily be discussed. In this section the code exclusively was run in `Cartoon` mode, on a cubed-shell grid. If not stated otherwise, the excision surface is at $r = 1.8M$, and the outer boundary at $r = 31.8M$. In the base setup it is $\mathcal{N} = 3$ radial subpatches each with $N = 25$ points per direction. The runs were performed on a desktop machine with an eight-core intel i7 CPU, which was able to compute at about $250M/\text{hour}$, the base run requiring about 14 MB of RAM.

7.2 Freezing gauge source functions

Killing gauge sources: Given initial data which admit a time-like Killing vector and neglecting the effect of outer boundary conditions, the evolution can be made trivial at the continuum level by choosing the Killing lapse and shift, and taking the

gauge source functions H_a so that $\partial_t \alpha = \partial_t \beta^i = 0$ initially. In particular it has to be

$$H_a = -\Gamma_a(t = 0), \quad \partial_t H_a = 0. \quad (7.8)$$

Kerr-Schild evolutions with SpEC GHG: First, the Kerr-Schild initial data was evolved with the standard formulation parameters of [70], namely $\gamma_4 = \gamma_5 = 0$ and $\gamma_0 = 1$ on the base grid as just described, using the gauge boundary conditions (4.32). Immediately the innermost subpatch has the largest constraint violation, peaked at around 10^{-6} in the C_x component of the harmonic constraint. This is not surprising because the innermost subpatch contains the part of the solution with the largest derivatives. The evolution successfully continues until the final time $t = 1000 M$. But after the initial expansion to 10^{-6} , a slow expansion in C_x is visible, and this growth becomes more rapid as the simulation continues. By the end, the maximum value of C_x is around 10^{-3} , with peaks appearing at the inner and outer boundary of roughly the same size. The resolution is increased from the base grid to $N = 27, 29$ and $N = 31$. The $N = 27$ point grid runs at about $178 M/\text{hour}$, and the initial peak in the C_x constraint violation is reduced by a factor of about two, with this ratio of improvement slowly declining until the end of the evolution. The $N = 29$ grid runs at $129 M/\text{hour}$, with both the initial magnitude of the violation and the ‘slow expansion’ of the C_x constraint quashed, the peak being a factor 2.8 smaller than in the base run at the end of the simulation. The highest resolution $N = 31$ point grid ran at $96 M/\text{hour}$, with the final improvement in C_x against the base run being a factor of 5.3. Since the largest constraint violation occurs in the excision subpatch an obvious question is whether or not the excision and outer boundaries would interact badly if they were on the same grid. Although the issue is of little practical concern for production runs, for development it deserves a little attention, and therefore the base grid from before was evolved, but cutting the outer two subpatches so that the outer boundary lies at $11.8 M$. This test is not completely fair because the outer boundary conditions are expected to perform better as they are applied further out. With this the initial peak in the violation of the C_x constraint is about five times greater than in the base run at $t = 200 M$. At the end of the evolution again at $t = 1000 M$ by coincidence the constraint violation in the restricted domain is smaller, but this is just because the slow oscillations in each simulation are out of phase.

Kerr-Schild incoming wave evolutions with SpEC GHG: Next the same initial data and gauge were evolved, but this time with a similar domain as in Fig. 3 of [70]. For this $\mathcal{N} = 2$ radial subpatches have been taken, with the same base resolution as before, so that the outer boundary is placed at $r = 21.8 M$. Exactly the same gravitational wave data was injected at the outer boundary as in that study, taking in particular,

$$\partial_t h_{ab} = \dot{f}(t)(\hat{x}^a \hat{x}^b + \hat{y}^a \hat{y}^b - 2\hat{z}^a \hat{z}^b), \quad (7.9)$$

with the vectors here the coordinate vectors defined in the obvious way. It is

$$f(t) = A \exp[-(t - t_p)^2 / \omega^2], \quad (7.10)$$

with $A = 10^{-3}$, $t_p = 60 M$ and $\omega = 10 M$. In Fig. 20 shows the results from these experiments, obtained with a sequence of different resolutions. The Weyl scalar Ψ_4 (4.25) is plotted averaged over the outer boundary,

$$4\pi \langle R\Psi_4 \rangle^2 = \int |\Psi_4|^2 dA. \quad (7.11)$$

The surface area of the outer boundary is $4\pi R^2$. Fitting the highest resolution data between $t = 100$ and $t = 200$ the ring-down frequency was found to be $\Re[\omega M] \sim 0.372$ as expected [36]. In this evolution it was found that the apparent horizon oscillates slightly as the gravitational wave is absorbed, increasing the horizon mass (5.18) by about $6 \times 10^{-7} M$, with M the ADM mass of the analytic initial data. Note that the gauge boundary condition being employed here is not identical to that used in [70], so the agreement is remarkable. The effect of much larger pulses of gravitational radiation falling onto a blackhole using similar gauge conditions was studied in [39].

Discussion of and comparison with [27]: The prior **bamps** study focussed on obtaining numerical stability in the evolution of a single Schwarzschild blackhole with the Kerr-Schild slicing. The numerical method used a Chebyshev-Fourier-Fourier spatial discretization on a single shell with a spin weighted spherical harmonic filter to prevent high frequency growth of the error. In that study the outer boundary condition employed simply fixed the incoming characteristic variables (4.5) to some given data, namely their initial values. This approach is possible only when the analytic solution is known, otherwise incoming constraint violations

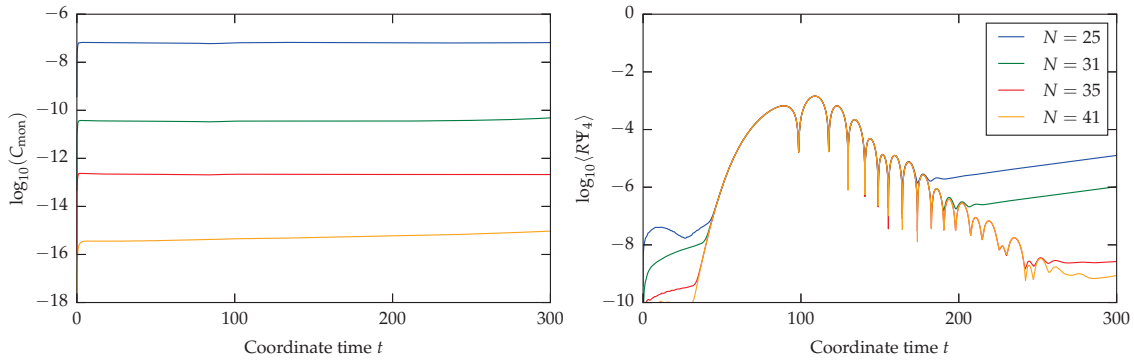


Figure 20: The right panel shows the average over the Weyl scalar Ψ_4 in the outer boundary for the evolution of Schwarzschild perturbed by a small gravitational wave injected through the boundary. The left panel demonstrates the convergence of the constraints as resolution is increased. At lower resolutions a drift is present in the ring-down. There is good agreement with Fig. 3 of [70], and the ring-down frequency agrees well with the analytical computation [36]. At the end of the test there is some disagreement with [70], but since square-roots of very small quantities are being taken it is expected that this is caused by round-off error. It seems that on the cubed-shell grid more resolution is needed to obtain clean results than with the spherical harmonic discretization used in [70]. This is perhaps not surprising, since the latter discretization is well-suited to the given data.

are generated. Placing the inner boundary at $r = 1.8 M$ and the outer boundary at $r = 11.8 M$, very long evolutions, say until at least $t = 200\,000 M$, could be performed with little resolution, in accordance with [70]. On the other hand, using this method, the naive boundary conditions rapidly deteriorated as the outer boundary was pushed out, and, crucially resolution did not help but rather made the problem worse. A possible explanation for the latter effect is that no filter was being applied in the radial (Chebyshev discretized) direction, which is a crucial ingredient for stability with the current method. The likely cause of the boundary problem is that, as explained in [82], boundary conditions that just freeze the incoming GHG characteristic variables are orders of magnitude more reflecting than the Sommerfeld like choice contained in (4.32). Evidence for this is obtained in the current code by changing from the gauge boundary condition (4.32) to use instead,

$$\perp_{ab}^{(G)cd} [\partial_t u_{cd}] \hat{=} 0, \quad (7.12)$$

evolving once more the Kerr-Schild initial data on the base grid. Placing the outer boundary further out then results in greater reflections which, once the domain is sufficiently large, causes the code to fail. However rather than trying to improve a

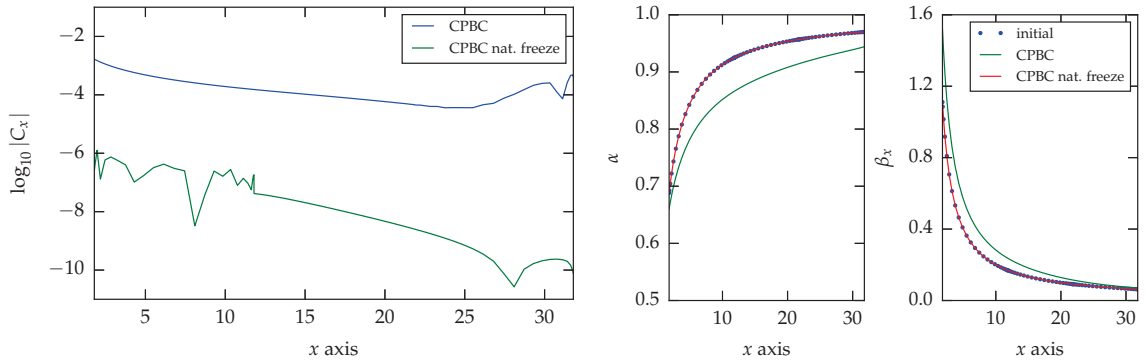


Figure 21: Comparison of the evolution of Schwarzschild with Killing-Kerr-Schild gauge sources with either the gauge boundary condition (4.32) or the alternative (4.33) at the end of the simulation $t = 1000 M$. The left panel shows the logarithm of the constraint violation C_x . In the latter case the violation is greatly reduced. In right two panels the lapse and shift are plotted; the drift present when using (4.32) is practically absent with (4.33).

condition only suitable for evolving known data, immediately the outer boundary conditions in **bamps** were switched to the constraint preserving, radiation controlling conditions. In these conditions that issue is completely absent.

Kerr-Schild evolutions with simplified constraint subsystem: Using the standard choice for the formulation parameters $\gamma_4 = \gamma_5 = 1/2$, and taking $\gamma_0 = 0.2$, returning to the base resolution from the SpEC GHG tests, by $t = 200$ the C_x constraint is about 5 times larger than that obtained before, and by the end of the simulation the new run has accrued a C_x constraint violation with a sharp peak at the outer boundary of order 10^{-1} . This result seems to be in contradiction to those of section 6.2, however there the gauge boundary condition (4.33) was employed. Increasing the constraint damping to $\gamma_0 = 1$, the initial violation is comparable to the SpEC GHG evolution previously described throughout the evolution, and the spike at the outer boundary is suppressed by roughly an order of magnitude. At the end of this run the maximum of the C_x constraint occurs at the excision boundary with a value around 10^{-3} . This experiment thus highlights that the choice of the damping parameters and boundary conditions can be rather subtle.

Kerr-Schild evolutions with alternative boundary conditions: In this section again the base grid was used. The outer boundary conditions were switched to the alternative gauge boundary conditions (4.33), with $\gamma_4 = \gamma_5 = 1/2$ and $\gamma_0 = 1$. With this setup the aforementioned growth in the constraints is completely eradicated, and the drift in the lapse and shift is also suppressed. Evolving the same data

with the same formulation and gauge boundary condition, but using the modified constraint preserving boundary condition (4.40) gives almost identical results. Using instead the reflection reducing conditions (4.46) a small improvement in the violation throughout the simulation can be observed. Repeating the experiment with the incoming gravitational wave injected through the boundary with the standard constraint preserving condition (4.29) and the gauge boundary conditions (4.33), the growth visible in Fig. 20 is also completely absent, even on the base resolution $N = 25$ grid.

Harmonic Killing slice evolutions Now the formulation parameters are taken to be $\gamma_4 = \gamma_5 = 1/2$, and $\gamma_0 = 1$, and the Harmonic Killing slice with the gauge boundary condition (4.32) is evolved. The test successfully runs to $t = 1000 M$. Comparing with the equivalent evolution of Kerr-Schild data, initially near the excision boundary the C_x constraint violation is significantly greater in the Harmonic Killing test. By $t = 200 M$ this difference has accrued to around two orders of magnitude. Later however, as the violation in the Kerr-Schild Killing evolution starts to grow, it overtakes that of the Harmonic Killing evolution. At $t = 1000 M$ the peak of the constraint violation in the Harmonic Killing run is about an order of magnitude smaller than in the earlier test. As remarked before, in the Kerr-Schild test the inner and outer boundaries have roughly the same magnitude in the C_x constraint violation. Interestingly the twin peaks are not present in the Harmonic Killing data because the outer boundary is hugely improved. This finding is consistent with the gauge wave tests presented in section 6.1, although this test is somewhat easier for the gauge boundary conditions because of the complete lack of dynamics present in the gauge wave test. In the Harmonic Killing evolution pure harmonic slicing is used, and some non-zero spatial gauge source functions, which suggests perhaps that the growth at the outer boundary is predominantly caused by the use of a non-trivial gauge source function for the lapse function, as it interacts with the boundary. Indeed looking once more at the lapse function towards the end of the Kerr-Schild evolution it can be seen that it is drifting from its initial value, but that this effect converges away with resolution. In any case, the peak in the constraint violation at the outer boundary in the Killing Kerr-Schild data is suppressed as the outer boundary is placed further out.

Harmonic Killing slice with gauge perturbation: A desirable property for a set of dynamical coordinates is that in the presence of a, perhaps approximate, timelike Killing vector they quickly asymptote to a time-independent state. For

an arbitrary physical or gauge perturbation there is no hope that this will occur, and nor can any finite set of numerical experiments prove that there is a basin of attraction to a stationary state. However one can look for some indication of this behavior. To do so initial data for the Killing harmonic coordinates is taken and then perturb the initial lapse function by Gaussian as in the previous gauge wave evolutions. In terms of the first order GHG variables this is a slightly fiddly procedure, as compared with the use of lapse, shift and spatial metric. Therefore a quick summary is given here:

- Set spatial metric and extrinsic curvature from the exact solution.
- Take the Killing lapse and shift. Use the conditions $\partial_t \alpha = 0$ and $\partial_t \beta^i = 0$ to set the gauge source functions H_a .
- Add the desired perturbation to the lapse (or shift) and then transform to the first order GHG variables.

The lapse is perturbed by a Gaussian,

$$\Delta \alpha = A \exp \left[-2 (r - r_0)^2 \right], \quad (7.13)$$

with $A = 0.3 M$ and $r_0 = 4 M$. A similar experiment was made in [71], but starting from a Maximal slice of Schwarzschild to test the gauge driver system. The perturbation in the lapse propagates away, rapidly leaving behind the solution with the harmonic Killing data with unperturbed spatial coordinates, or at least negligibly perturbed. The greatest danger to the evolution is probably that the excision boundary fails to be outflow, but at least with this perturbation that does not occur.

Harmonic evolutions with incoming gravitational wave: Giving the same gravitational wave data (7.9) as previously, evolving with the standard boundary conditions (4.29) and (4.32) but using the harmonic Killing gauge source functions. It is not obvious how, if at all the spacetime computed is related to that considered before, but in any case a very similar decay was observed in Ψ_4 . Remarkably the growth present in Fig. 20 is absent even in this low resolution $N = 25$ test.

7.3 Phasing-in the damped wave gauge

The transition function: As elsewhere, [96] is followed in transforming from one generalized harmonic gauge H_a^1 to another H_a^2 . The composite source function

is simply,

$$H_a(t) = T(t) H_a^1 + [1 - T(t)] H_a^2. \quad (7.14)$$

The transition function is,

$$T(t) = \begin{cases} 0, & t < t_d, \\ \exp(- (t - t_d)^2 / \sigma_d^2), & t \geq t_d. \end{cases} \quad (7.15)$$

In the following experiments it is $t_d = 0$ and $\sigma_d = 10 M$. Note that care must be taken to construct the time and space derivatives of H_a with the transition function. This choice results in gauge source functions that are only C^1 at $t = t_d$, which could be avoided with a different transition function. It is not clear if this finite differentiability will have a large effect on extracted physical quantities from a simulation.

Kerr-Schild initial slice: For the first phase-in test, a Kerr-Schild slice of Schwarzschild is taken and evolved with $\gamma_4 = \gamma_5 = 1/2$ and $\gamma_0 = 1$, on the base resolution grid. The outer boundary conditions was set to either the gauge boundary condition (4.32) or the constraint preserving condition (4.40) (including a $1/r$ term). The wave gauge parameters were set to $p = r = 1$ and $\eta_L = \eta_S = 0.1 M$. The value of η_S here is much smaller than in our wave collapse evolutions. The reason for this is that when evolving a blackhole it is crucial that the excision boundary is pure outflow in the PDEs sense. In other words the characteristic speeds must all have the same outward pointing sign. Since the speeds in the s^i direction are like $-\beta^s \pm \alpha$ this means that the shift cannot become too small or else the excision boundary will fail, which in turn means that η_S cannot be chosen too large. Therefore the excision boundary is placed deeper into the blackhole so that $r_{\min} = M$ and carefully monitor the coordinate lightspeeds at the inner boundary. Note that this requirement is likely to cause difficulties when computing extreme gravitational waves, because on the one hand large shifts can result in poor resolution of important features, but on the other hand they may be required in some other region to successfully excise the blackhole region. The evolution immediately shows significant dynamics. The peak of the C_x constraint violation along the x -axis is two orders of magnitude greater than in our initial Kerr-Schild base run with Killing gauge sources. The reason for this is presumably the presence of non-trivial dynamics, plus the fact that the excision boundary is nearer to the physical singularity, similar to the effect

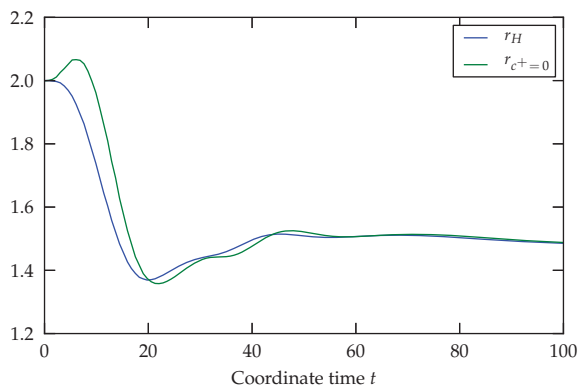


Figure 22: The radius of the apparent horizon r_H , and the radius at which the outward lightspeed vanishes $r_{c^+=0}$, computed on the base grid with inner boundary at $r = 1.2 M$. To successfully excise, the speed must be negative at the inner boundary. The figure shows that excision *exactly* on the apparent horizon is not possible throughout all of the run.

seen with the harmonic Killing slice. Regardless, by $t = 100 M$ the data seems very close to stationary. The simulation then evolves to the target time $t = 1000 M$, and remarkably at the end of the simulation the constraint violation in C_x along the x -axis has a maximum value which is an order of magnitude smaller than in the base run. At no point does the excision boundary fail to be outflow. As a check of the axisymmetric apparent horizon finder the results obtained are compared with the simpler algebraic condition,

$$H = \frac{1}{\sqrt{g_{rr}}} \partial_r \log(\gamma_{\theta\theta}) - 2K^\theta_\theta = 0. \quad (7.16)$$

which characterizes the position of the apparent horizon in spherical symmetry. Near perfect agreement was found throughout. The apparent horizon moves from its initial radius $r_H = 2.00$ inwards until it reaches $r_H = 1.44$ around $t = 25$. From there the horizon starts to grow again and seems to settle down to $r_H = 1.48$. However in our lowest resolution run, a small drift of the horizon outwards is visible. At late time of the simulation, around $t = 800$, this drift accelerates and the horizon becomes aspherical. Higher resolution runs show that this effect converges away.

Harmonic initial slice: Since the stationary fully harmonic coordinates are singular at $r = M$, one might guess that the stationary spatial generalized harmonic coordinates with gauge source functions (4.11) are also singular at some radius on the Killing slice, at least for some range of the parameters η_L, η_S . Given the broad

experience in using these coordinates in binary blackhole simulations, the naive expectation would be that, if present, this coordinate singularity is pushed further towards the physical singularity rather than out towards the event horizon for standard choices of the gauge source functions. But this behavior is not clear. To truly resolve the issue one could simply solve for such coordinates along the lines of [57], however this was not considered in this work. Instead simulations have been performed varying the initial excision surface from the base grid excision radius $r_{\min} = 1.8 M$ down to $r_{\min} = 1.0 M$ in steps of $0.2 M$. Unsurprisingly, the initial constraint violation is greater in the excision subpatch as the inner boundary is placed closer to the singularity, amounting to about an order of magnitude in the C_x constraint between the $r_{\min} = M$ and $r_{\min} = 1.2 M$ boundary runs by $t = 50$. Besides this there is little to distinguish between the five runs, and at least down to this excision radius no sign of a coordinate singularity forming. By eye the lapse function in the shared part of the domain agrees very well throughout the evolution. Although a slight drift between them is present towards the end of the test, this is acceptable since the outer boundary conditions are being imposed at different radii, the solutions need not agree everywhere. There is however a time around $t = 20$ above which the runs with inner boundary $r \geq 1.4 M$ fail to be outflow at the excision surface. Assuming that this is not caused by numerical error this means that boundary conditions are required at the surface. It furthermore means that convergence of the numerical scheme as resolution is increased is impossible. The fact that this does not correspond to a catastrophic failure of the code is perhaps inconvenient, because it indicates that great care must be taken in monitoring the excision surface. On the other hand, since placing the excision boundary very far in has a large cost in accuracy, a careful balance must be struck. In the SpEC code this is taken care of dynamically of by a control mechanism [59] which **bamps** does not yet have. In Fig. 22 the relationship between the character of the excision boundary and the apparent horizon is examined. Comparing the initially harmonic and Kerr-Schild slice evolutions with excision radius $r_{\min} = M$ it was found that although the lapse functions initially disagree, by about $t = 125 M$ they have exactly the same profile and lie almost on top of one another. After this time the agreement is maintained.

8 Evolution of collapsing Brill waves with bamps

In this section `bamps` is used to evolve centered Brill wave data with positive A . First, the focus is put at previous work on Brill data evolutions. It is studied if the results obtained with `bamps` are in agreement. Afterwards the dynamical excision strategy of `bamps` is discussed and proven to work well at the example of a simulation of a supercritical Brill wave with $A = 8$. In the last part the supercritical regime is approached. The results of this section will be published in [Wey3, Wey4].

8.1 Agreement with earlier work

Alcubierre et. al.: In [9] Brill waves were evolved numerically for the first time in 3d. The BSSN formulation was used in combination with maximal slicing and vanishing shift. Using the initial data (3.3), it was found that the critical point lies between $A = 4$ and $A = 6$, and furthermore that this finding could be refined to $A = 4.85 \pm 0.15$, although the data for this latter claim was never presented. Super-criticality was diagnosed by finding an apparent horizon, which occurred for the $A = 6$ data at $t = 7.7$. In [53] it was shown that BSSN combined with this gauge choice results in an ill-posed PDE system, meaning that this approach should be abandoned if the goal is to achieve accurate results that converge to the continuum solution as resolution is increased.

Garfinkle and Duncan: In [49] it was found, evolving Brill wave initial data with q as in (3.3), taking $z_0 = 0$, that the critical amplitude A_* lies between $A = 4$ and $A = 6$. The data was classified either by evolving until the spacetime was close to flat and subsequent collapse seemed implausible, or by explicitly finding an apparent horizon. The formulation employed was explicitly axisymmetric, and consisted of a mixed elliptic-hyperbolic system with maximal slicing $K = 0$, well-posedness of which, to the best of our knowledge, has not been studied. The results obtained in this work agree with the findings of both [9] and [49]. Evidence for this agreement is given in what follows; because the method of this work employs a different gauge it is difficult to make a side-by-side comparison, beyond classifying the spacetimes as sub or supercritical. The effect of changing the shape of the initial data parameters σ_ρ and σ_z was also studied in [49], but this has not been considered within this work.

Rinne: In the PhD thesis [80] evolutions of Brill waves with $z_0 = 0$ were presented, with a free-evolution and partially constrained scheme, both in explicit axisymmetry.

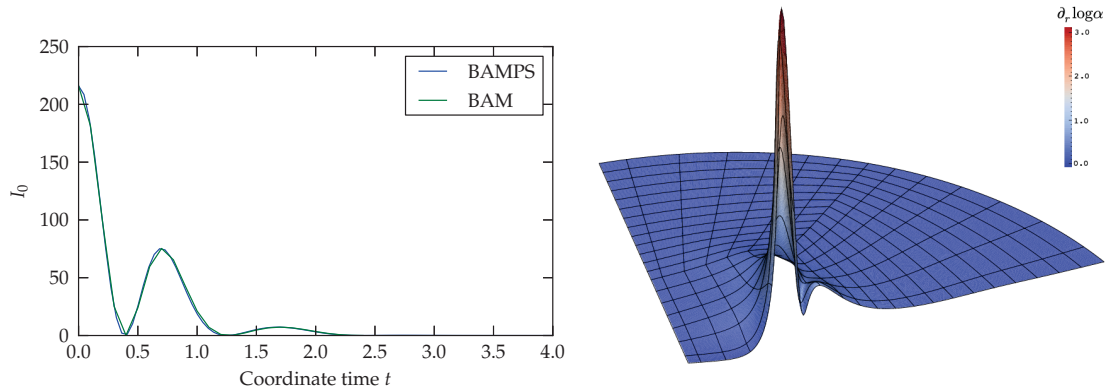


Figure 23: The left plot shows the central value of the Kretschmann scalar in a centered Brill wave $A = 1$ evolution, with BAM and **bamps**. BAM was used with moving puncture coordinates (data taken from [Wey2]) and **bamps** was run with pure harmonic slicing. This figure is meant to be directly compared to Fig. 9.2 of [80]. The fact that **bamps** employs a different spatial gauge does not matter here because harmonic lapse is a pure slicing condition, so values of the lapse function can be compared one-to-one at the symmetry axis. On the right is shown a snapshot of $\partial_r \alpha$ in the xz plane at $t \approx 1.72$, which should be compared with Fig. 9.3 of [80]. Although the spatial coordinates differ, there is an obvious qualitative agreement.

The focus at this point is on the free-evolution scheme, the $Z(2+1)+1$ formulation, since that is where the clearest comparison with the **bamps** results are possible. In that case harmonic slicing was taken with vanishing shift. This choice is convenient for the comparison with **bamps** results because although it is not possible to choose the same shift condition, harmonic lapse is a pure slicing condition, which means that **bamps** evolutions should obtain the same foliation of the same spacetime (starting from the same initial lapse) albeit with different spatial coordinates. Since there is a preferred observer, namely that at the origin, this allows to compare quantities explicitly there. Fortunately the work [80] contains several such plots. In the left panel Fig. 23 shows the Kretschmann scalar at the origin as a function of time for $A = 1$ centered Brill wave data, which should be compared with Fig. 9.2 of [80]. The evolution for this test uses harmonic slicing $\bar{\eta}_L = 0$ and the damped harmonic shift $\bar{\eta}_S = 6$ and otherwise the standard setup. The agreement is, at least by eye, extremely good. Taking $A = 4$ it was found that with sufficient resolution a sharp peak in the gradient of the lapse could be resolved and the data was, in agreement with [49], subcritical. Using the same parameters as in the previous test, the results are in agreement. The right panel of Fig. 23 shows $\partial_\rho \ln \alpha$ at $t = 1.72$. This is the time at which Rinne finds the largest peak in this quantity. A similar

plot is Fig. 9.3 in [80], which cannot be directly compared because of the differing spatial coordinates, although the qualitative agreement is very clear. In the **bamps** results the largest peak appears at around $t = 2.08$, but the magnitudes in $\partial_\rho \ln \alpha$ differ by less than 5% across these times. In Fig. 25, to be compared with Fig. 9.9 of [80], the left panel shows the logarithm of the lapse at the origin as a function of coordinate time for amplitudes $A = 4, 5, 6$. In the right hand panel the value of the Kretschmann scalar at the origin is plotted. At lower resolutions the Kretschmann scalar exhibits high-frequency oscillatory behavior, but these wiggles converge away rapidly. The most challenging data evolved in Rinne’s experiments was the $A = 5$ wave, for which sub- and super-criticality was not discerned using the free-evolution algorithm, partially because the data was still oscillatory at the time the method failed at around $t = 6$. All of the different resolutions tried with $A = 5$ in this suite of tests crashed at coordinate time $t \simeq 12$. The results of an apparent horizon search on this data are plotted in the left panel of Fig. 24. The apparent horizon was first found at $t \simeq 6.2$ and subsequently until the evolution fails. Rinne concluded that the critical amplitude lies below $A = 6$, although no apparent horizon could be found inside his data. Instead the classification was made by observing that the Kretschmann scalar was blowing-up. This diagnostic is flawed because as one approaches the critical point it is expected to generate arbitrarily large curvature even in subcritical data. In the absence of an apparent horizon or event horizon however, other diagnostics may be similarly flawed, and the Kretschmann is at least a spacetime scalar, so one might prefer it as a diagnostic to ‘collapse of the lapse’. Running the apparent horizon finder on the $A = 6$ data an apparent horizon was found at $t \simeq 2$ and later. The result is plotted in the right hand panel of Fig. 24.

Studies with BAM: In 2005 [85] the BAM finite differencing code [28, 64, 99] was used to evolve centered geometrically prolate Brill waves with the BSSN formulation combined with several different gauge conditions, maximal slicing, harmonic slicing, and the moving puncture gauge condition. The main complications were reported to be constraint violation, which was likely caused by lack of resolution, and which did vary significantly from one gauge to another. In section 3, see also [Wey2], the BAM code was used again to understand how much further, if at all, standard modern numerical relativity methods can go beyond those previously discussed. This time with the focus purely on the moving puncture gauge. Now the findings with BAM are compared with those of **bamps**. Starting in BAM with weak $A = 1$ data, it was found that the lapse initially decreased, but rapidly returned back to unity; qualitatively

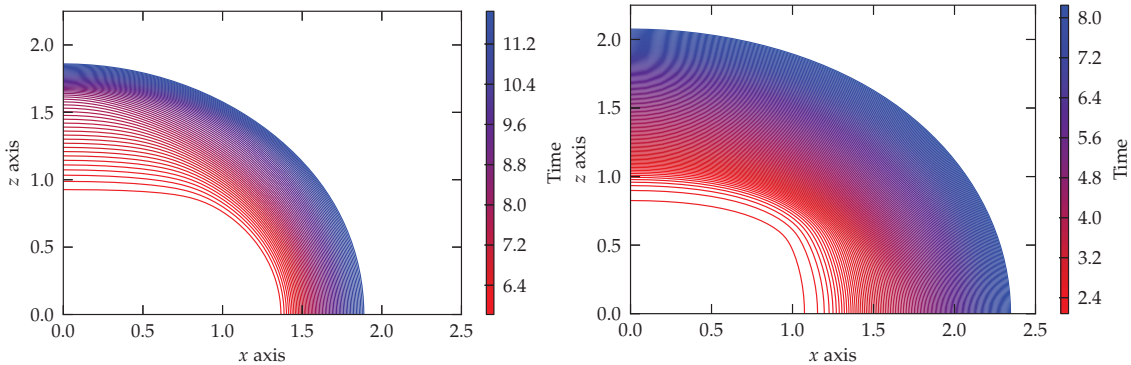


Figure 24: The left panel shows the development of the apparent horizon for Brill waves with amplitude $A = 5$, evolved with pure harmonic slicing and damped harmonic shift. The horizon is first found at $t = 5.82$, with area $A_H = 15.7$. At the end of the evolution at $t = 11.9$ the area has increased to $A_H = 16.7$. The right panel shows the same for the $A = 6$ evolution. The initial area at $t = 2.1$ is $A_H = 33.7$ and the final is $A_H = 40.6$ at $t = 8.24$.

the same behavior can be found with **bamps** despite the different gauge used and although the lapse function decreases by a smaller amount. The Kretschmann scalar was found to be peaked initially at the origin with a value around 216. The maximum value of the Kretschmann scalar in the domain immediately decreases and never grows beyond the initial peak as the wave propagates away. The left panel of Fig. 23 also plots the central value of the Kretschmann scalar obtained in this BAM experiment. Since different time coordinates are being used the values should not agree, but the size of the second peak should. The BAM value is about $I_0 \sim 75$ which agrees extremely well with the **bamps** experiment. The Hamiltonian constraint violation in this particular BAM run is of the order 10^{-3} at the time of the second peak, whereas the roughly corresponding F_t constraint inside **bamps** is less than 10^{-6} . This is not a fair comparison, but indicates that the **bamps** data is superior in this case. Therefore one expects that as more resolution is added to the BAM grid the result would converge to the **bamps** result. Taking data that is stronger, for example $A = 5$, the BSSN setup failed as an incoming pulse in the lapse became evermore sharp, resulting in what seemed to be a coordinate singularity. This would be acceptable if an apparent horizon could be found before the code crashed, but this was not the case. Going to higher amplitudes still, similar failures occurred, and the conclusion was drawn that moving puncture coordinates were not suitable for managing this initial data. In the comparison with [80] it was found that using **bamps** the $A = 5$ data can be classified supercritical. No sign of a coordinate

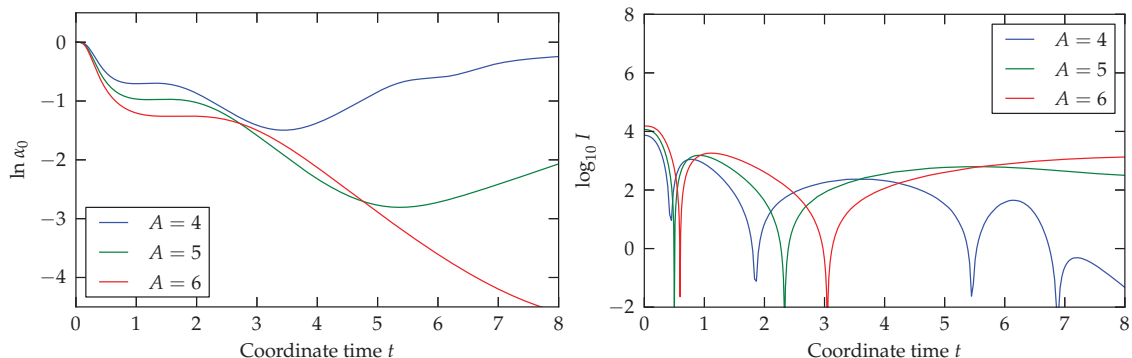


Figure 25: Comparing **bamps** results with the work of Rinne [80]. In these runs Brill waves are evolved using harmonic lapse and $\bar{\eta}_S = 6.0$ for the shift. On the left the logarithm of the central lapse over time for $A = 4, 5$ and 6 is shown. These results should be compared with Fig. 9.9 in [80]. The line for $A = 4$ agrees quite well. The others disagree. On the right the central value of the Kretschmann scalar is plotted.

singularity was seen before an apparent horizon was discovered despite the two lapse functions appearing qualitatively similar initially.

8.2 Disagreement with Sorkin

The most puzzling result to reproduce was the one presented by Evgeny Sorkin in [94]. He used an axisymmetric generalized harmonic code with an adaptive finite-differences method [93]. In his studies he reported critical behavior in positive, centered Brill wave data. However, he surprisingly stated a significantly larger value for the critical amplitude than in earlier studies of the same data. Furthermore, he found that the waves collapse to form a singularity on a ring in the equatorial plane, in, whereas Abrahams and Evans [7] found the singularity to form at the center. This section is an attempt to understand these findings by studying centered, positive Brill data evolutions with **bamps**. Firstly, it is demonstrated that with **bamps** it can also be observed that the peak of the Kretschmann scalar appears off-axis. Even more, it is shown that the position of the peak of the Kretschmann can be controlled by the choice of gauge source function. For this fact a geometric interpretation is given. Secondly, it will be demonstrated explicitly that the amplitude $A = 6.073$ evolved in [94] is supercritical by locating an apparent horizon in the evolution. The simulations of this subsection have been carried out on a cubed-ball grid with the following setup: The inner cube extends from -0.5 to 0.5 and is divided into $\mathcal{N}_{\text{cu}} = 9$ subpatches with $N_{\text{cu}} = 21$ grid points in each dimension. For the transition shell

from 0.5 to 1.0 only one shell $\mathcal{N}_{\text{cs}} = 1$ with $N_{\text{cs}} = 35$ points in the radial direction is used. From here $\mathcal{N}_{\text{ss}} = 22$ outer shells with $N_{\text{ss}} = 35$ radial collocation points have been used to go to the outer boundary at 12. All simulations have been carried out in 3d using the octant symmetry mode of `bamps`.

Position of the peak curvature: Consider a collapse spacetime which has a causal structure similar to that depicted in Fig. 5 of [55], but rather in vacuum. Furthermore consider different foliations through the spacetime, in which the time coordinate tends to tick more or less slowly in a region of high curvature depending on some *singularity avoidance* parameter. Suppose now a given a patch of this spacetime up to a finite time coordinate, as in a numerical relativity simulation. Naturally then which observer encounters the largest curvature will depend upon the singularity avoidance parameter. In context of `bamps` such a parameter is given by $\bar{\eta}_L$. To demonstrate this with `bamps`, a centered Brill wave with $A = 6.073$ has been evolved. This amplitude is shown to be supercritical in the next paragraph. The evolution has been carried out with fixed $\bar{\eta}_S = 6, p = 1$ and one of $\bar{\eta}_L = 0, 0.2$ or $\bar{\eta}_L = 0.4$. The left plot of Fig. 26 shows the lapse in the evolutions at coordinate times $t = 1$, which demonstrate the effect of the singularity avoidance parameter $\bar{\eta}_L$. The pure harmonic slicing case $\bar{\eta}_L = 0$ is the strongest singularity avoiding. There the peak of the Kretschmann appears at $\rho = 0.88$, where it simply grows until the numerics fail. Increasing the parameter to $\bar{\eta}_L = 0.2, 0.4$ the peak of the Kretschmann appears at a coordinate radius of $\rho = 0.73$ and $\rho = 0.64$ respectively, before the numerics fail.

Apparent horizon formation: Again centered $A = 6.073$ Brill data is evolved. The gauge parameters are $\bar{\eta}_S = 0.4, p = 1$ and $\bar{\eta}_S = 6$, which is the largest choice of $\bar{\eta}_L$ from above. Evolving with different resolutions, with $21^3, 25^3$ and 29^3 points in the inner cubes, rapid convergence of the constraints is found. For example, the maximum of the C_x component of the Harmonic constraints along the x-axis are approximately $5 \times 10^{-5}, 9 \times 10^{-6}$ and 8×10^{-7} respectively at $t \approx 1.25$. The apparent horizon is searched using the method described in Section 5.2. It is first found at around $t = 1$. On a fixed numerical spacetime data set perfect fourth order convergence in the apparent horizon data is found. Comparing the apparent horizons discovered on the different resolution data, perfect qualitative agreement is found. The apparent horizon at different times is plotted in Fig. 26, where the expansion of the horizon can clearly be seen.

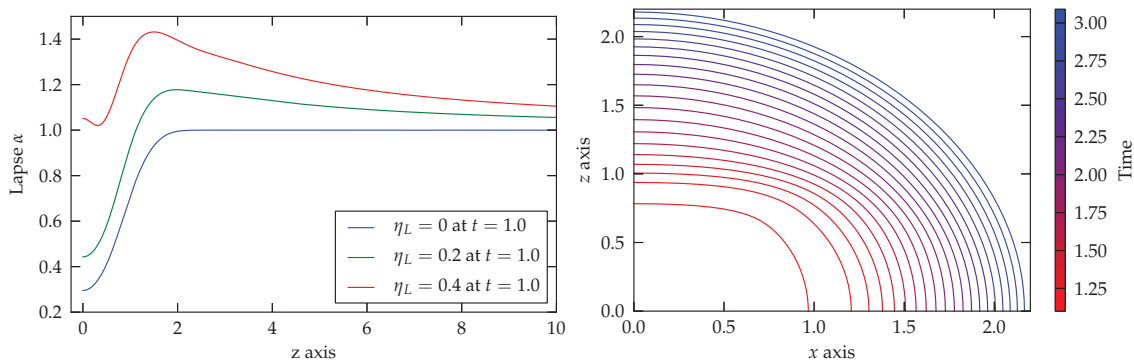


Figure 26: In the left panel the lapse for the centered $A = 6.073$ Brill wave is plotted with the three generalized harmonic gauges $\bar{\eta}_L = 0, 0.2$ and $\bar{\eta}_L = 0.4$ at coordinate time $t = 1.0$. The more “singularity avoiding” the gauge choice, the smaller the lapse becomes around the origin. In the right hand panel the apparent horizons Brill wave initial data is plotted. The initial horizon mass is $M_H = 0.84$ and has increased to around $M_H = 0.90$ before the code fails. These values are to be compared with the ADM mass, $M_{\text{ADM}} = 1.02$.

8.3 Evolution of supercritical waves

In this section the numerical evolution of a centered Brill wave with $A = 8$ is presented. This highly supercritical initial data is used as a test case for our excision algorithm for a dynamically forming blackhole.

Dynamical excision strategies

The dynamical excision method of `bamps` currently consists of the following steps:

- 1. Evolve to collapse:** Evolve on cubed ball grid, running the apparent horizon finder in ‘daemon’ mode. The finder then triggers a `bamps` checkpoint once a horizon is found.

- 2. Go-to excision grid:** Next, interpolate the checkpoint data onto a cubed-shell grid. In this step the excision boundary is placed just inside the apparent horizon. However, the single blackhole evolutions already showed that this may not always be possible, as some wiggle room is needed to allow for dynamical behavior of the horizon. This can require some experimentation, although fine-tuning does not seem necessary.

- 3. Regauge:** Adjust the lapse and shift to ensure that the excision boundary is pure outflow. As a particular choice, the lapse and shift from Kerr-Schild slicing

of Schwarzschild is taken,

$$\alpha = \left(1 + \frac{2m}{r}\right)^{-1/2}, \quad \beta^r = \frac{2m}{r} \left(1 + \frac{2m}{r}\right)^{-1}, \quad (8.1)$$

and translated to Cartesian components in the obvious way. It is desirable that the radial coordinate light-speeds are close to zero, preferably positive, at the apparent horizon, since this determines the direction of motion of the horizon. Therefore the m parameter is set to satisfy this condition reasonably well, although again without particular fine tuning.

4. Safety-net evolution: From here, the single blackhole gauge source parameters $p = 1.0, q = 0.0$ and $r = 1.0$ are used. During the evolution a safety net is employed. If any coordinate light-speed on the excision boundary reaches a given threshold, typically $c_* = -0.05$, **bamps** regauges to guarantee the outflow character is maintained. The apparent horizon is monitored. If it falls off of the numerical domain the simulation returns to an earlier checkpoint and a regauge with a smaller m is carried out to avoid this behavior. As the horizon expands its position is tracked and periodically the **Go-to** step from above is executed with excising further out and regauging with a greater m .

Discussion: As currently implemented this procedure requires that some steps have to be performed by hand. The numerical results in the following subsection serve to demonstrate ‘proof of principle’ of this algorithm. On the other hand it seems at least clear how those steps should be automated. At the regauge step the use of the first order GHG variables is again a little fiddly. It would be much more convenient if the lapse and shift were readily available as variables. But the procedure is similar to that described in the gauge perturbation tests in section 7.2, so the full details are not given here. Also at the regauge step, it might be good to choose lapse and shift by abandoning the spherical ansatz and imposing that the coordinate light-speeds at the apparent horizon vanish. The SpEC approach to controlling the excision surface is much more sophisticated, employing a control mechanism [59]. However, the main focus of **bamps** is on the collapse of waves to form, presumably, a single blackhole. Therefore it seems reasonable to stick with this simple approach if at all possible. One aspect of the method that is not very aesthetically appealing, is that by changing the lapse and shift in discrete steps a patch of spacetime is computed in coordinates that are not globally smooth. Another issue associated with this is that of geometric uniqueness, which for the

initial boundary value problem is an open question. Nevertheless one expects that the differences to the computed spacetime with one choice of regauging parameters or another will be rather small in practice, so this does not represent an immediate practical concern.

Supercritical Brill wave evolutions

Initial data and grid setup: A centered Brill wave with amplitude $A = 8$ is chosen as initial data. It has a ADM mass of $M_{\text{ADM}} = 1.77$. The maximum of the Kretschmann scalar in the initial data occurs at the origin, taking the value 1.7×10^4 . Following the algorithm just outlined, the evolution was started on a cubed-ball grid with $\mathcal{N}_{\text{cu}} = 11$, $\mathcal{N}_{\text{cs}} = 13$, $\mathcal{N}_{\text{ss}} = 20$, and 55^3 points per cube, with internal boundaries $r_{\text{cu}} = 1.5$, $r_{\text{cs}} = 6.5$ and the outer boundary placed at $r = 30 \simeq 17 M$. The code was run in Cartoon mode on the local cluster *Quadler* on 240 cores. The evolution was carried out with the generalized harmonic gauge, as in section 6 in the evolution of a *much* weaker $A = 2.5$ Brill wave, now with the gauge parameters $\bar{\eta}_L = 0$ and $\bar{\eta}_S = 6$. At coordinate time $t = 1.95$ the first apparent horizon was found with mass $M_H = 1.59 \simeq 0.9 M$.

Continuation to code crash: If continuing this evolution without going to an excision grid after the apparent horizon forms, the constraints inside the apparent horizon rapidly grow along with the Kretschmann scalar. The run then crashes at roughly $t = 3.9$. This gives the clear signal that if one wants to examine the final masses of blackholes formed during collapse, using the GHG formulation, a robust excision algorithm will be essential. In fact at $t = 3.85$ the horizon has a mass of $M_H = 1.64$ on the cubed-ball grid. At the end of the excision simulation, to be described momentarily, at $40 M$ after apparent horizon formation, the mass has grown to $M_H = 1.70$. In the first critical gravitational wave collapse paper [6], the blackhole masses were evaluated roughly $t = 17 M$ after apparent horizon formation, according to a prescription based on the quasinormal modes of Schwarzschild. Comparing those values with the ones obtained by **bamps** is difficult because here different time coordinates are used. But the basic expectation is that the maximal slicing condition is more “singularity avoiding” than one of the generalized harmonic gauges, and therefore one might expect to obtain comparable results if it is possible to evolve for a similar coordinate time after the appearance of a horizon. This is, however, not clear and deserves further investigation. In any case without excising the blackhole region, the meager $\sim 2 M$ after collapse is clearly insufficient. The

simulations of section 3 using the BSSN setup with moving-puncture method were also not able to successfully evolve this type of data beyond apparent horizon formation. But here at least a concrete improvement has been made, in that an apparent horizon was found *before* the method fails.

Evolution on excision grid: Checkpointing the solution at $t = 3.6$ the data was then interpolated onto a cubed-shell grid. Here, again the barycentric Lagrange interpolation was used as in the apparent horizon finder. The excision radius was set to $r = 0.73M$ with the outer boundary position fixed. The grid was setup with $\mathcal{N}_{ss} = 27$ radial and 9 angular subpatches, having a resolution of 35^3 points per cube. The evolution were carried out in Cartoon mode. In the first regauge step the mass parameter was set to $m = 0.4$. As shown in Fig. 27 on the right, this step immediately removes most of the constraint violation from the computational domain, and the largest spatial derivatives, so that the constraint monitor is $\sim 10^{-8}$ as compared to $\sim 10^3$ on the original cubed-ball. This difference seems very troublesome until taking into account that, for example the peak of the Kretschmann scalar on the cubed ball grid is $\sim 10^3$ whereas on the cubed-shell it is ~ 1 . So the reduction in the constraints obviously occurs because the most extreme part of the domain has been removed. Note also that the definition of the constraint monitor in this work does not include a normalization by the size of the solution, as in for example [70] and subsequent papers. In view of this our reduction in resolution is justified. The evolution then proceeded, now on 120 cores using $\bar{\eta}_L = \bar{\eta}_S = 0.1$. The regauge safety-net was triggered 3 times up to $t = 5.9M$, having fixed $c_* = -0.05$, but the apparent horizon remains on the computational domain throughout the calculation. At $t = 5.9M$ a “**Go-to**” step of the algorithm was triggered again, this time excising at $r = 1.0M$ choosing $m = 0.8$. After this the regauge safety-net was not called before $t = 17M$, when the cubed-shell grid was changed once more, keeping the same grid parameters but excising at $r = 1.12M$, and regauging with $m = 1$. The evolution continued $t = 24.7M$, at which time the grid was changed for the final time, before which the safety-net was again not called. In the last grid the excision radius was $r = 1.24M$ and the regauge was done with $m = 1.2$. After this the safety-net was not called, and the evolution was terminated at $t = 50M$ after apparent horizon formation. Note that in this evolution the “**Go-to**” step also employed the phase-in for the generalized harmonic gauge, as described in our single blackhole evolutions in section 7.3, taking the same parameters employed in those earlier tests, but now with the initial source functions

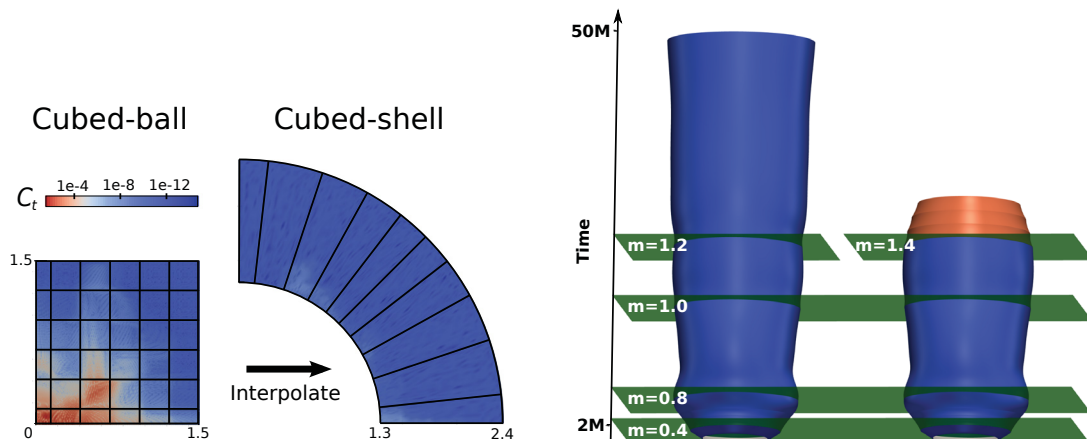


Figure 27: On the left is plotted the constraint violation at example of C_t at the time of the checkpoint $t = 3.6$. When interpolating from the cubed-ball to the cubed-shell grid, the area with highest constraint violation is removed. On the right the dynamic of the apparent horizons for two simulations are shown. The intersecting green planes denote the “Go-to” steps at which the mass parameter m is changed. In the simulation which horizon is plotted at the outer right in the last “Go-to” the mass is set too big which causes the horizon to move inwards. It finally falls off the grid and the simulations fails.

chosen so that the lapse and shift were frozen as the evolution starts on the new grid. Other experiments show that this procedure is not strictly necessary. It may be that some refinement is required for this method to allow the evolution of supercritical data *indefinitely* after the collapse, but examining the mass of the apparent horizon, it seemed that the solution has mostly settled down, which should be good enough to diagnose a final mass of the blackhole.

Dynamics of the apparent horizon: In the computation described above, as can be seen on the left of Fig. 27, the apparent horizon is always present on the computational domain. The horizon mass initially rapidly grows to a value around $M_H = 1.7$ where it remains roughly constant. Throughout the simulation whenever the regauge safety-net is triggered a slight oscillation in the horizon mass follows. When changing the grid the horizon mass exhibits a more prominent kink. On the right of Fig. 27 the apparent horizon is plotted which is obtained when, less-wisely, the parameter $m = 1.4$ is chosen in the last “Go-to” at $t = 24.7 M$. With this choice the apparent horizon rapidly contracts, although the code fails before it leaves the domain. The safety-net is called ever-more frequently as the method insists on forcing the inner boundary to remain pure outflow, until eventually the

Sweep	A range	ΔA	$A_\star \in$	N	$\mathcal{N}_{\text{cu}}, \mathcal{N}_{\text{cs}}, \mathcal{N}_{\text{ss}}$	$r_{\text{cu}}, r_{\text{cs}}, r_{\text{ss}}$	Notes
#1	[4.6, 5.0]	10^{-1}	[4.6, 4.7]	21	15, 11, 13	1, 7, 20	Non-cartoon runs
#2	[4.61, 4.70]	10^{-2}	[4.69, 4.70]	21	15, 11, 17	1, 7, 24	$p = 0, q = -2$ for $A = 4.69$
#3	[4.691, 4.999]	10^{-3}	[4.696, 4.698]	33	15, 11, 18	1, 7, 25	$p = 0.5$ for $A = 4.696$

Table 3: This table summarizes the sweeps of simulations that have been carried out in order to bracket the critical amplitude in Brill wave evolutions with positive A .

code crashes at $t = 31.6 M$. The physical interpretation of this is that the excision boundary is falling off of the domain, which starts to drift outside the blackhole region, and that the safety-net then forces the worldline of the excision boundary to be spacelike. This interpretation would be clearer if an event horizon finder was available, but is given credence by performing evolutions of a Schwarzschild blackhole with the m gauge parameter similarly poorly chosen. These tests show that the areal radius of the excision boundary can indeed fall outside of the event horizon at $r = 2 M$.

8.4 Going to the critical regime

After having reproduced and compared results of previous work with those obtained with **bamps**, a first attempt was made to study the near critical region of centered Brill waves with positive A . Therefore several simulations with **bamps** have been run, trying to bracket the critical amplitude as narrowly as possible. Simulations which settle down to flat spaces are classified as being subcritical, simulations in which an apparent horizon is detected are classified as being supercritical. At the time this study was done, the excision technique of subsection 8.3 was not fully available. Simulations of a blackhole on the cubed-ball grid do not last long enough to evolve until the blackhole settles down and its final mass can be determined. Therefore, it was not possible to study scaling in the blackhole mass within this attempt. Instead, following [55, 94] it was tried to observe critical scaling of the maximum value of the Kretschmann scalar when approaching the critical point from the subcritical side. In total three sweeps of runs have been carried out, which will be discussed in the following. If not stated otherwise, the gauge parameters are set to $p = 1.0, q = 0$ and $r = 1.0$ and $\bar{\eta}_L = 0.4, \bar{\eta}_S = 6.0$. The grid setup for each sweep is given in table 3.,

Sweep #1: Based on previous experiments, the amplitude range for the first sweep of runs was set to $A = [4.6, 5.0]$. Evolving in steps of $\Delta A = 0.1$, the critical amplitude was bracketed to $A_\star \in [4.6, 4.7]$. The basic dynamics of each of the initial

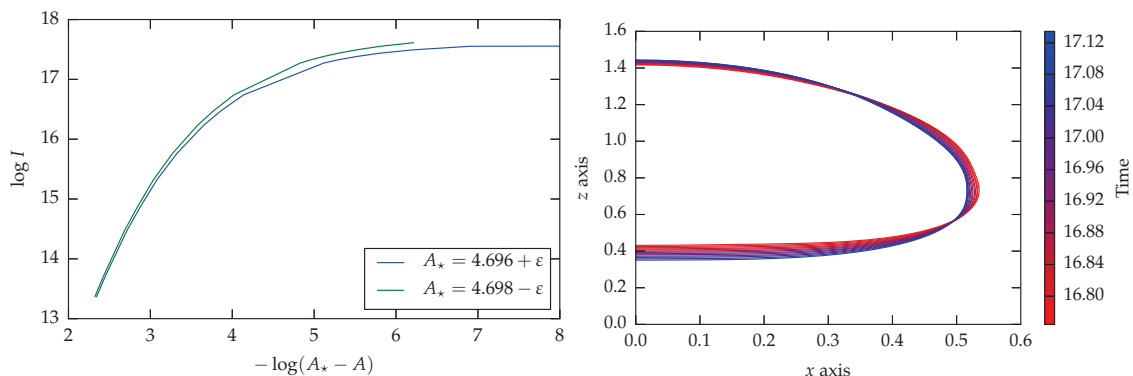


Figure 28: On the left the global maximum of the Kretschmann scalar for subcritical evolutions of Brill waves with positive A is plotted. The blue line assumes the critical value slightly above the highest subcritical amplitude, the green line slightly below the lowest supercritical amplitude found. For this $\varepsilon = 10^{-14}$ was used. The plot shows that up to this accuracy no exponential scaling can be observed.

The plot on the right shows the apparent horizons at different times in $A = 4.698$ centered Brill initial data. Evidently two apparent horizons appear in the data, centered around $z \approx \pm 0.9$, indicating the likelihood that the family results in head-on binary blackhole spacetime near the critical amplitude.

data sets are initially rather similar. At first a pulse in the Kretschmann scalar propagates out from the origin predominantly out in the ρ direction. The pulse then propagates more slowly, eventually turning around and traveling towards the origin. As it propagates in, the pulse is smeared out parallel to the z -axis. As the pulse hits the axis, there is a rapid growth resulting in a maximum at some $\pm z_0$.

Sweep #2: In the next set of runs Brill waves in the range $A = [4.6, 4.7]$ in steps of $\Delta A = 0.01$ have been evolved. These simulations found that all Brill waves with amplitude $A = 4.68$ or less can be classified as subcritical. Again, $A = 4.70$ was found to be supercritical. The simulation of $A = 4.69$ crashed around $t = 15$ with a spike in the lapse occurring and no sign of apparent horizon formation. Further studies of this amplitude led to the result that when evolving this amplitude with the gauge parameters changed to $p = 0, q = -2$, the spike in the lapse disappears and the simulation settles down to flat space. Therefore, this amplitude was classified as being subcritical. The reason that with this changed gauge choice the simulation is successful can be found by recalling the evolution equation for the lapse again,

$$\partial_t \alpha = -\alpha^2 K + \bar{\eta}_L \alpha^{q+2} \log \left(\frac{\gamma^{p/2}}{\alpha} \right) + \beta^i \partial_i \alpha. \quad (8.2)$$

In the strong field region the lapse approaches zero, causing the second term in the lapse evolution equation to vanish. However in subcritical evolution this term is needed to drive the lapse back to one. Choosing this term $q = -2$ this term does not disappear if the lapse approaches zero, allowing the subcritical evolution to settle down to flat spacetime again. Taking $p = 0$ removes the γ within the log term. In preliminary studies it was found that the γ term is responsible for the occurring spikes in the lapse function. From now on, for all supercritical runs this changed choice of gauge parameter is chosen. In supercritical runs, the default values are used.

Sweep #3: A third set of runs was set up to study the amplitudes $A = [4.691, 4.699]$ with resolution $\Delta A = 0.001$. Using the gauge parameters $q = -2, p = 0$, the amplitudes $4.691 - 4.696$ were found to settle down to flat space. With $q = 0, p = 1$, $A = 4.498$ and $A = 4.697$ could be classified as supercritical. It was necessary to change the gauge parameter again to $q = -2, p = 0.5$ to determine the status of $A = 4.696$. With this choice, it was found to be subcritical. However, still unclear is the Brill data with $A = 4.697$. Experimenting with different gauge choice and resolutions, no clear conclusion could be made. With this sweep of runs, the critical amplitude was bracketed to $A_\star \in [4.696, 4.698]$.

Discussion: With the performed simulations stated above, two major findings were made: The first finding is that in the simulations carried out, no critical scaling has been observed. According to [55], if critical phenomena are present during gravitational collapse, then one expects to see power-law scaling of curvature invariants in the subcritical regime $A \lesssim A_\star$. Fig. 28 shows on the left, as a log-log plot, the peak of the Kretschmann scalar in the spacetimes as a function of $A_\star - A$, assuming the most optimistic and pessimistic bounds on A_\star obtained by taking either $A_\star = 4.696 + \epsilon$ or $A_\star = 4.698 - \epsilon$, with $\epsilon = 10^{-14}$. With the obtained data, this quantity seems to level off when approaching the critical point. Of course, this statement can only be made up to the highest subcritical amplitude evolved, $A = 4.696$. It could be that the critical amplitude has to be approached much closer in order to observe exponential scaling.

The second finding was made in the evolution of the lowest supercritical amplitude, $A = 4.698$. At $t = 1.68$ *two disjoint apparent horizons* appear in the data. They are centered around $z \approx \pm 0.9$, which is roughly the location at which the Kretschmann scalar starts to grow ever more rapidly before the simulation fails. The apparent horizons are shown on the right of Fig. 28. This indicates that evol-

ing centered, positive A Brill data results in a head-on binary blackhole spacetime near the critical amplitude. The simulation has been rerun with increased resolution, $N = 39$, and it was found that the constraints are converging and the same apparent horizon can be found in the higher resolution simulation data. Even though this finding is certainly very interesting, as **bamps** does not provide the necessary excision grids for two black holes and furthermore does not have a moving-excision setup with an appropriate control mechanism, this unfortunately means that it is not possible to evolve the resulting spacetime to a final end-state with **bamps**.

9 Conclusions

Summary

In this thesis two common setups of Numerical Relativity have been used to study the collapse of gravitational waves.

The first setup considered was the BSSN setup. In this context the BAM code was used to evolve Brill wave data. In the case of Brill waves with positive A , the evolutions have not been successful, except for very weak waves. During evolutions steep gradients in the metric functions appear and spoil the simulation. Comparing this feature with previous studies, the gradients seem to be caused by appearing coordinate singularities. This led to the conclusion that the gauge choice of the BSSN setup, the moving-puncture gauge, is not suitable for the evolution of this data.

Successful evolutions of Teukolsky waves which have been carried out in [Wey2] raised the question about the differences between Teukolsky and Brill initial data. For this a characterization of twist-free, axisymmetric data as either geometrically oblate or prolate has been discussed. Based on this consideration an attempt was made to set up Brill wave data which is as close as possible to Teukolsky wave data. This resulted in the evolution of off-centered, negative A Brill waves. With this data it was possible to successfully evolve the collapse of the waves to blackhole formation and furthermore to track the apparent horizon from its formation up to the time when the blackhole settled down.

Even though it was possible to evolve the collapse of the waves in this setup, the simulations began failing when approaching the critical amplitude too closely. One of the main reasons for this seemed to be the lack of accuracy of the simulations. Therefore, a second approach was taken in this work to develop an improved setup which provides higher accuracy for the goal of studying the collapse of gravitational waves. For this `bamps`, a 3d pseudospectral numerical relativity code implementing the GHG setup, has been developed. The idea for this code was based on the approach taken in the SpEC code with several improvements for the study of collapsing gravitational waves in mind.

Different aspects of the GHG formulation, in particular the outer boundary conditions and the treatment of the patching boundary conditions have been discussed. Furthermore the code implementation details, including the cubed-sphere grid setup and the numerical methods have been presented. A main component in order to

obtain a stable grid setup in **bamps** was the derivation of the correct value for the penalty parameter which is necessary for the treatment of the patching boundaries.

As all data considered within this work is axisymmetric, different axisymmetric considerations for **bamps** have been discussed. One major performance boost was gained in implementing a Cartoon method in **bamps** which reduces the numerical domain to a 2d plane. Also in the context of axisymmetry apparent horizon finding has been discussed. Here special care has been taken in deriving regularity conditions on the symmetry axis. A second code, the apparent horizon finder **AHloc**, has been developed to study axisymmetric apparent horizon in the data evolved with **bamps**.

Before the actual simulations of relevant spacetimes, a set of carefully performed experiments has been carried out in order to test the code. These tests include evolutions of gauge waves, convergence tests, the use of different constraint damping and GHG formulation parameters, scaling and performance tests. They led to the conclusion that the **bamps** code is working accurately, efficiently, scales up to a large number of processors, and works on a sufficiently general grid setup to evolve interesting initial data.

Before studying the collapse of waves to blackholes, it was necessary to test single blackhole evolutions with **bamps**. Using Kerr-Schild initial data it was found that it is possible to have sufficiently long and accurate blackhole evolution with **bamps**. It was also possible to evolve a blackhole perturbed by an injected gravitational wave and to observe its ring-down. This evolution made it possible to directly compare **bamps** with published results of the SpEC code.

After the single blackhole tests the focus was shifted to evolutions of Brill wave data. Several simulations were performed in order to compare the **bamps** results with either published work or independent evolutions with the BAM code. In almost all those cases it was possible to not only reproduce the results but also to successfully evolve amplitudes which have been found troublesome before. The only disagreement was found with the work of Sorkin, where the **bamps** simulations showed that many of the amplitudes of this work considered subcritical are actually supercritical.

For the simulation of supercritical Brill waves an algorithm has been presented which excises the blackhole in **bamps** simulation after apparent horizon formation and controls that the excision boundary stays outflow. This method allowed a successful evolution of a strongly supercritical Brill wave with $A = 8$ through collapse until over $t = 50M$. Using the apparent horizon finder **AHloc**, it was possible to track the horizon from its formation until the end of this simulation.

In the final part of this thesis the critical region for positive A Brill wave data was approached. It was possible to bracket the critical amplitude to $A_* \in [4.696, 4.698]$. Approaching the critical amplitude, it turned out that the simulations became more difficult to handle. Not only is increasing resolution needed in order to resolve all features, but in some of these evolutions it was crucial to adjust the gauge parameters to gain a successful simulation. However, two interesting findings have been made. In the subcritical simulations no exponential scaling of the maximum of the Kretschmann scalar was observed. To make a final conclusion to this statement, it is necessary to approach the critical point closer. In the evolution of the $A = 4.698$, which is the lowest supercritical amplitude evolved, the spacetime approaches a head-on binary blackhole spacetime with two horizons.

Future Prospects

One of the main drawbacks in the evolution of positive amplitude Brill waves near the critical point with **bamps** is its rigid grid setup. While it allows to run highly accurate simulations which can be distributed effectively to parallel working computing cores, for very high resolutions it ultimately makes the runs too expensive. For example, one of the runs carried out in subsection 8.4 costs up to 30,000 core hours. Therefore a future step for the development of **bamps** will be an implementation of more flexible grid setups. For this it would be helpful to drop the restriction that the boundaries of subpatches have to match. This can be realized by deriving a penalty method including interpolation at boundary points. With this improvement it would be possible to put high resolution on the grid where it is needed while having lower resolution anywhere else. As the Brill evolution with **bamps** revealed that the location of blackhole formation is not predictable it would furthermore be good to have adaptive grids which can change their resolution locally during the simulation at places where the error is largest. Implementing such a method will introduce the additional question of load balancing which is not trivial to implement effectively. Therefore it might be reasonable to rely on existing libraries such as p4est [32]. Additional performance improvement might also be gained by extending the existing MPI parallelization to the use of accelerators such as GPUs. Another useful change in the grid setup of **bamps** is the implementation of a “sphere-to-cube” transition shell. With this missing building block a grid with two excision boundaries can be realized. Such a grid setup might allow to evolve the supercritical Brill data in which two blackholes form until a stationary state. However, this includes

the appropriate adjustment of the algorithm presented in Sec. 8.3 which guarantees that the excision surfaces stay outflow.

While the suggestions above are all of a technical kind, the existing version of the `bamps` code can already be used for future studies of interesting scenarios of numerical relativity. Obviously, compared with the BAM results of section 3, a next step in this direction would be the evolution of Brill waves with negative A and Teukolsky waves. While the first is straight forward to start with, for the second choice the initial data solver has to be extended to compute such data. Another idea for studying collapsing gravitational waves would be to start with flat spacetime and inject gravitational waves through the boundary. In the case of blackhole spacetimes this has already been successfully tested (see Fig.20). The advantage of this method would be that there would basically be no initial constraint violation caused by interpolated initial data. Besides the collapse of gravitational waves one might also consider evolving collapsing scalar fields with `bamps`, which has already been successfully considered, for example in [58]. All these ideas summarized lead to the conclusion that the `bamps` code already turned out to be helpful for studying the physics of collapsing gravitational waves, and it also is a perfect basis for future development and a source of inspiration for many interesting ideas to be studied.

A List of publications

- [Wey1] Andreas Weyhausen, Sebastiano Bernuzzi, and David Hilditch. Constraint Damping for the Z4c Formulation of General Relativity. *Phys. Rev. D*, 85:024038, 2012.
- [Wey2] David Hilditch, Thomas W. Baumgarte, Andreas Weyhausen, Tim Dietrich, Bernd Brügmann, Pedro J. Montero, and Ewald Müller. Collapse of Nonlinear Gravitational Waves in Moving-Puncture Coordinates. *Phys.Rev.*, D88(10):103009, 2013.
- [Wey3] David Hilditch, Andreas Weyhausen, and Bernd Brügmann. A Pseudospectral Method for Gravitational Wave Collapse. Preprint arXiv:1504.04732, 2015.
- [Wey4] David Hilditch, Andreas Weyhausen, and Bernd Brügmann. Evolutions of Centered Brill Waves with a Pseudospectral Method. 2015. In preperation.

B List of presentations

- 15.11.2010 SFB/TR7 Videoseminar in Jena
GPU Computing for Numerical Relativity
- 04.12.2010 Annual Meeting for the GRK 1523 in Oppurg
Numerical Relativity
- 31.04.2011 DPG Frühjahrstagung in Karlsruhe
GPU Computing for Numerical Relativity
- 08.09.2011 Workshop on Numerical Relativity and Gravitational Waves in Parma
Constraint damping for the Z_4 formulation of general relativity
- 02.04.2012 DPG Frühjahrstagung in Göttingen
Constraint damping for the Z_4 formulation of general relativity
- 06.12.2012 Begutachtung GRK 1523 in Jena
Numerical General Relativity
- 04.09.2013 International Conference on Mathematical Modeling in Physical Science in Prague
Numerical Evolutions of Collapsing Gravitational Waves

C Bibliography

- [1] LIGO - Laser Interferometer Gravitational Wave Observatory, <http://www.ligo.caltech.edu/>.
- [2] KAGRA - Kamioka Gravitational Wave Detector, <http://gwcenter.icrr.u-tokyo.ac.jp/en/>.
- [3] Virgo/EGO - European Gravitational Observatory, <http://www.ego-gw.it/>.
- [4] SpEC - Spectral Einstein Code, <http://www.black-holes.org/SpEC.html>.
- [5] GSL: the GNU Scientific Library: <http://www.gnu.org/software/gsl/>.
- [6] Andrew M. Abrahams and Charles R. Evans. Trapping a geon: Black hole formation by an imploding gravitational wave. *Phys. Rev. D*, 46:R4117–R4121, 1992.
- [7] Andrew M. Abrahams and Charles R. Evans. Critical behavior and scaling in vacuum axisymmetric gravitational collapse. *Phys. Rev. Lett.*, 70:2980, 1993.
- [8] P. Ajith, S. Babak, Y. Chen, M. Hewitson, B. Krishnan, J. T. Whelan, B. Brügmann, P. Diener, J. A. González, M. Hannam, S. Husa, M. Koppitz, D. Pollney, L. Rezzolla, L. Santamaria, A. M. Sintes, U. Sperhake, and J. Thornburg. Phenomenological template family for black-hole coalescence waveforms. *Class. Quantum Grav.*, 24:S689–S699, 2007.
- [9] M. Alcubierre, G. Allen, B. Brügmann, E. Seidel, and W.-M. Suen. Towards an understanding of the stability properties of the 3+1 evolution equations in general relativity. *Phys. Rev. D*, 62:124011, 2000. [gr-qc/9908079](https://arxiv.org/abs/gr-qc/9908079).
- [10] Miguel Alcubierre. *Introduction to 3+1 Numerical Relativity*. Oxford University Press, USA, 2008.
- [11] Miguel Alcubierre, G. Allen, B. Brügmann, G. Lanfermann, E. Seidel, W.-M. Suen, and M. Tobias. Gravitational collapse of gravitational waves in 3D numerical relativity. *Phys. Rev. D*, 61:041501 (R), 2000.

- [12] Miguel Alcubierre, S. R. Brandt, B. Brügmann, C. Gundlach, Joan Massó, E. Seidel, and P. Walker. Test-beds and applications for apparent horizon finders in numerical relativity. *Class. Quantum Grav.*, 17:2159–2190, 2000.
- [13] Miguel Alcubierre, S. R. Brandt, B. Brügmann, D. Holz, E. Seidel, R. Takahashi, and J. Thornburg. Symmetry without symmetry: Numerical simulation of axisymmetric systems using Cartesian grids. *Int. J. Mod. Phys. D*, 10(3):273–289, 2001. gr-qc/9908012.
- [14] Miguel Alcubierre, Bernd Brügmann, Peter Diener, Michael Koppitz, Denis Pollney, Edward Seidel, and Ryoji Takahashi. Gauge conditions for long-term numerical black hole evolutions without excision. *Phys. Rev. D*, 67:084023, 2003.
- [15] Miguel Alcubierre and Joan Massó. Pathologies of hyperbolic gauges in general relativity and other field theories. *Phys. Rev. D*, 57(8):R4511–R4515, 1998.
- [16] Marcus Ansorg, Bernd Brügmann, and Wolfgang Tichy. A single-domain spectral method for black hole puncture data. *Phys. Rev.*, D70:064011, 2004.
- [17] R. Arnowitt, S. Deser, and Charles W. Misner. The dynamics of general relativity. In L. Witten, editor, *Gravitation: An Introduction to Current Research*, pages 227–265. Wiley, New York, 1962.
- [18] Luca Baiotti and Luciano Rezzolla. Challenging the paradigm of singularity excision in gravitational collapse. *Phys. Rev. Lett.*, 97:141101, 2006.
- [19] Richard Baltensperger and Manfred R. Trummer. Spectral differencing with a twist. *J. Sci. Comp.*, 24(5):1465–1487, 2003.
- [20] T. W. Baumgarte and S. L. Shapiro. On the Numerical integration of Einstein’s field equations. *Phys. Rev.*, D59:024007, 1998.
- [21] Thomas W. Baumgarte and Stuart L. Shapiro. *Numerical Relativity: Solving Einstein’s Equations on the Computer*. Cambridge University Press, Cambridge, 2010.

- [22] Sebastiano Bernuzzi and David Hilditch. Constraint violation in free evolution schemes: comparing BSSNOK with a conformal decomposition of Z4. *Phys. Rev. D*, 81:084003, 2010.
- [23] M. Bjørhus. The ode formulation of hyperbolic pdes discretized by the spectral collocation method. *SIAM J. Sci. Comput.*, 16(3):542–557, 1995.
- [24] Luc Blanchet. Gravitational radiation from post-Newtonian sources and inspiralling compact binaries. *Living Rev. Relativity*, 5:3, 2002.
- [25] C. Bona, J. Massó, E. Seidel, and J. Stela. A New Formalism for Numerical Relativity. *Phys. Rev. Lett.*, 75:600–603, 1995.
- [26] John P. Boyd. *Chebyshev and Fourier Spectral Methods (Second Edition, Revised)*. Dover Publications, New York, 2001.
- [27] Bernd Brügmann. A pseudospectral matrix method for time-dependent tensor fields on a spherical shell. *J. Comput. Phys.*, 235:216–240, 2013.
- [28] Bernd Brügmann, José A. González, Mark Hannam, Sascha Husa, Ulrich Sperhake, and Wolfgang Tichy. Calibration of Moving Puncture Simulations. *Phys. Rev. D*, 77:024027, 2008.
- [29] Bernd Brügmann, Wolfgang Tichy, and Nina Jansen. Numerical simulation of orbiting black holes. *Phys. Rev. Lett.*, 92:211101, 2004.
- [30] Luisa T. Buchman and Olivier C. A. Sarbach. Towards absorbing outer boundaries in General Relativity. *Class. Quant. Grav.*, 23:6709–6744, 2006.
- [31] Luisa T. Buchman and Olivier C.A. Sarbach. Improved outer boundary conditions for Einstein’s field equations. *Class. Quant. Grav.*, 24:S307–S326, 2007.
- [32] Carsten Burstedde, Lucas C. Wilcox, and Omar Ghattas. **p4est**: Scalable algorithms for parallel adaptive mesh refinement on forests of octrees. *SIAM Journal on Scientific Computing*, 33(3):1103–1133, 2011.
- [33] Gioel Calabrese, Carsten Gundlach, and David Hilditch. Asymptotically null slices in numerical relativity: Mathematical analysis and spherical wave equation tests. *Class. Quant. Grav.*, 23:4829–4846, 2006.

- [34] Manuela Campanelli, Carlos O. Lousto, Pedro Marronetti, and Yosef Zlochower. Accurate evolutions of orbiting black-hole binaries without excision. *Phys. Rev. Lett.*, 96:111101, 2006.
- [35] Zhoujian Cao and David Hilditch. Numerical stability of the Z4c formulation of general relativity. *Phys. Rev. D*, 85:124032, 2012.
- [36] S. Chandrasekhar and S. Detweiler. The quasi-normal modes of the Schwarzschild black hole. *Proc. R. Soc. Lond. A.*, 344:441–452, 1975.
- [37] Matthew W. Choptuik. Universality and scaling in gravitational collapse of massless scalar field. *Phys. Rev. Lett.*, 70:9, 1993.
- [38] D. Christodoulou. *The Formation of Black Holes in General Relativity*. Number v. 4 in EMS monographs in mathematics. European Mathematical Society Publishing House, 2009.
- [39] Tony Chu, Harald P. Pfeiffer, and Michael I. Cohen. Horizon dynamics of distorted rotating black holes. *Phys.Rev.*, D83:104018, 2011.
- [40] G. B. Cook. Initial Data for Numerical Relativity. *Living Rev. Relativity*, 2000-5, 2000. [Online Article] cited on 30 Sep 2004, <http://relativity.livingreviews.org/Articles/lrr-2000-5>.
- [41] Gregory B. Cook and Mark A. Scheel. Well-behaved harmonic time slices of a charged, rotating, boosted black hole. *Phys. Rev. D*, 56:4775, 1997.
- [42] M. MacCallum D. Kramer, H. Stephani and E. Herlt. *Exact Solutions of Einstein's Field Equations*. Cambridge University Press, Cambridge, 1980.
- [43] H.P. de Oliveira and E.L. Rodrigues. Brill wave initial data: Using the Galerkin-collocation method. *Phys.Rev.*, D86:064007, 2012.
- [44] Tim Dietrich and Bernd Brügmann. Solving the Hamiltonian constraint for 1+log trumpets. *Phys.Rev.*, D89:024014, 2014.
- [45] Albert Einstein. Die feldgleichungen der gravitation. *Preuss. Akad. Wiss. Berlin, Sitzungsber.*, pages 844–847, 1915.

- [46] Albert Einstein. Zur allgemeinen relativitätstheorie. *Preuss. Akad. Wiss. Berlin, Sitzungsber.*, pages 778–786, 1915.
- [47] K. Eppley. Pure gravitational waves. In L. L. Smarr, editor, *Sources of Gravitational Radiation*, pages 275–291. Cambridge University Press, Cambridge, 1979.
- [48] H. Friedrich. On the hyperbolicity of Einstein’s and other gauge field equations. *Comm. Math. Phys.*, 100:525–543, 1985.
- [49] David Garfinkle and G. Comer Duncan. Numerical evolution of Brill waves. *Phys. Rev. D*, 63:044011, 2001.
- [50] Ericourgoulhon. 3+1 formalism and bases of numerical relativity. 2007.
- [51] Philippe Grandclément and Jérôme Novak. Spectral methods for numerical relativity. *Living Reviews in Relativity*, 12(1), 2009.
- [52] Carsten Gundlach. Critical phenomena in gravitational collapse. *Living Rev. Relativity*, 2:4, 1999.
- [53] Carsten Gundlach and Jose M. Martin-Garcia. Well-posedness of formulations of the Einstein equations with dynamical lapse and shift conditions. *Phys. Rev. D*, 74:024016, 2006.
- [54] Carsten Gundlach, Jose M. Martin-Garcia, G. Calabrese, and I. Hinder. Constraint damping in the Z4 formulation and harmonic gauge. *Class. Quantum Grav.*, 22:3767–3774, 2005.
- [55] Carsten Gundlach and José M. Martín-García. Critical phenomena in gravitational collapse. *Living Reviews in Relativity*, 10(5), 2007.
- [56] Mark Hannam, Sascha Husa, Frank Ohme, Bernd Brügmann, and Niall Ó Murchadha. Wormholes and trumpets: the Schwarzschild spacetime for the moving-puncture generation. *Phys. Rev.*, D78:064020, 2008.
- [57] Mark Hannam, Sascha Husa, Denis Pollney, Bernd Brügmann, and Niall Ó Murchadha. Geometry and regularity of moving punctures. *Phys. Rev. Lett.*, 99:241102, 2007.

- [58] James Healy and Pablo Laguna. Critical Collapse of Scalar Fields Beyond Axisymmetry. *Gen.Rel.Grav.*, 46:1722, 2014.
- [59] Daniel A. Hemberger, Mark A. Scheel, Lawrence E. Kidder, Bela Szilagyi, Geoffrey Lovelace, et al. Dynamical Excision Boundaries in Spectral Evolutions of Binary Black Hole Spacetimes. *Class.Quant.Grav.*, 30:115001, 2013.
- [60] J. S. Hesthaven. Spectral penalty methods. *Appl. Numer. Math.*, 33:23–41, 2000.
- [61] Jan S. Hesthaven, Sigal Gottlieb, and David Gottlieb. *Spectral Methods for Time-Dependent Problems*. Cambridge University Press, Cambridge, 2007.
- [62] David Hilditch. An Introduction to Well-posedness and Free-evolution. *Int.J.Mod.Phys.*, A28:1340015, 2013.
- [63] David Hilditch, Thomas W. Baumgarte, Andreas Weyhausen, Tim Dietrich, Bernd Brügmann, Pedro J. Montero, and Ewald Müller. Collapse of nonlinear gravitational waves in moving-puncture coordinates. *Phys.Rev.*, D88(10):103009, 2013.
- [64] David Hilditch, Sebastiano Bernuzzi, Marcus Thierfelder, Zhoujian Cao, Wolfgang Tichy, and Bernd Brügmann. Compact binary evolutions with the Z4c formulation. *Phys. Rev. D*, 88:084057, 2013.
- [65] David Hilditch and Ronny Richter. *Hyperbolicity of Physical Theories with Application to General Relativity*. 2013.
- [66] Nina Jansen, Bernd Brügmann, and Wolfgang Tichy. Numerical stability of the Alekseenko-Arnold evolution system compared to the ADM and BSSN systems. *Phys. Rev. D*, 74:084022, 2006. gr-qc/0310100.
- [67] R. P. Kerr. Gravitational field of a spinning mass as an example of algebraically special metrics. *Phys. Rev. Lett.*, 11:237–238, 1963.
- [68] L. E. Kidder and L. S. Finn. Spectral methods for numerical relativity. the initial data problem. *Phys. Rev. D*, 62:084026, 2000.

- [69] Luis Lehner, Oscar Reula, and Manuel Tiglio. Multi-block simulations in general relativity: high order discretizations, numerical stability and applications. gr-qc/0507004, 2005.
- [70] Lee Lindblom, Mark A. Scheel, Lawrence E. Kidder, Robert Owen, and Oliver Rinne. A new generalized harmonic evolution system. *Class. Quant. Grav.*, 23:S447–S462, 2006.
- [71] Lee Lindblom and Béla Szilágyi. An Improved Gauge Driver for the GH Einstein System. *Phys. Rev.*, D80:084019, 2009.
- [72] R. A. Matzner, M. F. Huq, and D. Shoemaker. Initial data and coordinates for multiple black hole systems. *Phys. Rev. D*, 59:024015, 1998. gr-qc/9805023.
- [73] Takashi Nakamura, Ken-ichi Oohara, and Yasufumi Kojima. General relativistic collapse to black holes and gravitational waves from black holes. *Prog. Theor. Phys. Suppl.*, 90:1–218, 1987.
- [74] Denis Pollney, Christian Reisswig, Erik Schnetter, Nils Dorband, and Peter Diener. High accuracy binary black hole simulations with an extended wave zone. *Phys. Rev. D*, 83:044045, 2011.
- [75] William H. Press, Saul A. Teukolsky, William T. Vetterling, and Brian P. Flannery. *Numerical Recipes 3rd Edition: The Art of Scientific Computing*. Cambridge University Press, New York, NY, USA, 3 edition, 2007.
- [76] Frans Pretorius. Evolution of binary black hole spacetimes. *Phys. Rev. Lett.*, 95:121101, 2005.
- [77] Frans Pretorius. Numerical relativity using a generalized harmonic decomposition. *Class. Quant. Grav.*, 22:425–451, 2005.
- [78] Frans Pretorius. Simulation of binary black hole spacetimes with a harmonic evolution scheme. *Class. Quantum Grav.*, 23:S529–S552, 2006.
- [79] O. Rinne. Constrained evolution in axisymmetry and the gravitational collapse of prolate Brill waves. *Classical and Quantum Gravity*, 25(13):135009, July 2008.

- [80] Oliver Rinne. *Axisymmetric Numerical Relativity*. PhD thesis, University of Cambridge, Cambridge, England, 13 September 2005. gr-qc/0601064.
- [81] Oliver Rinne, Luisa T. Buchman, Mark A. Scheel, and Harald P. Pfeiffer. Implementation of higher-order absorbing boundary conditions for the Einstein equations. *Class. Quant. Grav.*, 26:075009, 2009.
- [82] Oliver Rinne, Lee Lindblom, and Mark A. Scheel. Testing outer boundary treatments for the Einstein equations. *Class. Quant. Grav.*, 24:4053–4078, 2007.
- [83] C. Ronchi, R. Iacono, and P.S. Paolucci. The “cubed sphere”: A new method for the solution of partial differential equations in spherical geometry. *Journal of Computational Physics*, 124(1):93 – 114, 1996.
- [84] Milton Ruiz, David Hilditch, and Sebastiano Bernuzzi. Constraint preserving boundary conditions for the Z4c formulation of general relativity. *Phys. Rev. D*, 83:024025, 2011.
- [85] Lucia Santamaria. Nonlinear 3d evolutions of Brillwave spacetimes and critical phenomena. Master’s thesis, Friedrich-Schiller-Universität Jena, October 2006.
- [86] O. Sarbach, G. Calabrese, J. Pullin, and M. Tiglio. Hyperbolicity of the bssn system of einstein evolution equations. *Phys. Rev. D*, 66:064002, 2002. gr-qc/0205064.
- [87] G. Schäfer. The ADM Hamiltonian at postlinear approximation. *Gen. Rel. Grav.*, 18(3):255–270, 1986.
- [88] Erik Schnetter, Peter Diener, Nils Dorband, and Manuel Tiglio. A multi-block infrastructure for three-dimensional time-dependent numerical relativity. *Class. Quantum Grav.*, 23:S553–S578, 2006.
- [89] Karl Schwarzschild. Über das Gravitationsfeld einer Kugel aus inkompressibler Flüssigkeit nach der Einsteinschen Theorie. *Sitzungsber. Dtsch. Akad. Wiss. Berlin, Kl. Math. Phys. Tech.*, pages 424–434, 1916.

- [90] Karl Schwarzschild. Über das Gravitationsfeld eines Massenpunktes nach der Einsteinschen Theorie. *Sitzungsber. Dtsch. Akad. Wiss. Berlin, Kl. Math. Phys. Tech.*, pages 189–196, 1916.
- [91] M. Shibata and T. Nakamura. Evolution of three-dimensional gravitational waves: Harmonic slicing case. *Phys. Rev.*, D52:5428–5444, 1995.
- [92] Masaru Shibata. Time symmetric initial conditions of gravitational waves for 3D numerical relativity. *Phys. Rev. D*, 55:7529–7537, 1997.
- [93] E. Sorkin. Axisymmetric generalized harmonic evolution code. *Phys. Rev. D*, 81(8):084062, 2010.
- [94] Evgeny Sorkin. On critical collapse of gravitational waves. *Class. Quant. Grav.*, 28:025011, 2011.
- [95] A.N. Staley, T.W. Baumgarte, J.D. Brown, B. Farris, and S.L. Shapiro. Oppenheimer-Snyder Collapse in Moving-Puncture Coordinates. *Class. Quant. Grav.*, 29:015003, 2012.
- [96] Bela Szilagyi, Lee Lindblom, and Mark A. Scheel. Simulations of binary black hole mergers using spectral methods. *Phys. Rev.*, D80:124010, 2009.
- [97] Nicholas W. Taylor, Lawrence E. Kidder, and Saul A. Teukolsky. Spectral methods for the wave equation in second-order form. *Phys. Rev.*, D82:024037, 2010.
- [98] Marcus Thierfelder, Sebastiano Bernuzzi, and Bernd Brügmann. Numerical relativity simulations of binary neutron stars. *Phys. Rev. D*, 84(4):044012, Aug 2011.
- [99] Marcus Thierfelder, Sebastiano Bernuzzi, and Bernd Brügmann. Numerical relativity simulations of binary neutron stars. *Phys. Rev. D*, 84:044012, 2011.
- [100] Marcus Thierfelder, Sebastiano Bernuzzi, David Hilditch, Bernd Brügmann, and Luciano Rezzolla. The trumpet solution from spherical gravitational collapse with puncture gauges. *Phys. Rev. D*, 83:064022, 2011.

- [101] Jonathan Thornburg. Black hole excision with multiple grid patches. *Class. Quantum Grav.*, 21(15):3665–3691, 7 August 2004.
- [102] Jonathan Thornburg. A fast apparent-horizon finder for 3-dimensional Cartesian grids in numerical relativity. *Class. Quantum Grav.*, 21(2):743–766, 21 January 2004.
- [103] Jonathan Thornburg. Event and apparent horizon finders for 3+1 numerical relativity. *Living Rev. Relativity*, 2006. [Online article].
- [104] Wolfgang Tichy. Black hole evolution with the BSSN system by pseudo-spectral methods. *Phys. Rev. D*, 74:084005, 2006.
- [105] Wolfgang Tichy. Long term black hole evolution with the BSSN system by pseudo-spectral methods. *Phys. Rev. D*, 80:104034, 2009.
- [106] Lloyd N. Trefethen. *Spectral Methods in MATLAB*. SIAM, Philadelphia, 2000.
- [107] James R. van Meter, John G. Baker, Michael Koppitz, and Dae-Il Choi. How to move a black hole without excision: gauge conditions for the numerical evolution of a moving puncture. *Phys. Rev. D*, 73:124011, 2006.
- [108] Robert M. Wald. *General relativity*. The University of Chicago Press, Chicago, 1984.
- [109] Burkhard Zink, Erik Schnetter, and Manuel Tiglio. Multi-patch methods in general relativistic astrophysics. 1. Hydrodynamical flows on fixed backgrounds. *Phys.Rev.*, D77:103015, 2008.

D Abbreviations and Notations

Throughout this work geometrized units have been applied. In continuum equations latin letters from the beginning of the alphabet $a, b, c \dots$ are used for four dimensional indices, Latin letters $i, j, k \dots$ are used for spatial indices.

An exception are the indices n and s . The first means contraction with the timelike normal unit vector n^a , the second denotes a contraction with the spatial normal unit vector s^i .

Greek indices are used to refer to the position in a state-vector, grid indices, or where otherwise needed.

Within the following abbreviations have been used:

ADM	Arnowitt-Deser-Misner
BAM	Bi-functional Adaptive Mesh
BSSN	Baumgarte-Shapiro-Shibata-Nakamura
CPBC	Constraint Preserving Boundary Conditions
CPU	Central Processing Unit
GHG	Generalized Harmonic Gauge
GPU	Graphics Processing Unit
HDWG	Harmonic Damped Wave Gauge
LIGO	Laser Interferometer Gravitational Wave Observatory
MPI	Message Passing Interface

E Acknowledgements

I want to thank my supervisor Prof. Bernd Brügmann for having given me the opportunity to work in Numerical Relativity and for all the support he gave me during time in his group, from the beginning of my Studienarbeit, over my diploma thesis until the end of my PhD thesis.

I also want to thank David Hilditch for his valuable support during the whole time of my PhD and for inspiring my work with **bamps**. Especially for listening to me complaining when things haven't worked how they should. Without you this work would have not be possible or at least much less fun.

I am thankful for having met many nice and interesting people while working in Numerical Relativity. Thank you Sebastiano Bernuzzi, Julia Gundermann, Doreen Müller, Marcus Thierfelder, Pablo Galaviz, Zhoujian Cao, Norbert Lages, Roman Gold, Jason Grigsby, Rodrigo Panosso Macedo, Milton Ruiz and the Fantastic Five for many interesting discussions and insights, and especially for many funny moments.

I want to thank the Nvidia guys Timo Stich, Ralph Escherich and Mathias Schott for many common lunches at the asian place.

Finally, I am deeply thankful to my family. I thank my parents for their support through all the years, and my sister Susanne for again proof reading one of my works. I am particular grateful to my beloved wife Heidi and my son Jona who lived with me through all the ups and downs during this work and always supported and encouraged me.

F Lebenslauf

Andreas Weyhausen

- 29.06.1982 geboren in Leonberg
1999 mittlere Reife an der Walther-Rathenau-Realschule Schweinfurt
1999 - 2001 Berufsausbildung zum technischen Assistent für Informatik
2001 - 2002 berufliche Tätigkeit als C++ Entwickler bei WEB.DE
2002 - 2003 Wehrdienst beim Jägerlehrbataillon 353 in Hammelburg
2003 - 2005 Friedrich-Fischer-Berufsoberschule Schweinfurt
2005 fachgebundene Hochschulreife
2005 - 2010 Physikstudium an der Friedrich-Schiller-Universität Jena
2010 Physikdiplom
2010 - 2014 wiss. Mitarbeiter am Theoretisch-Physikalischen Institut der FSU Jena

Lehre

- WS 2011/2012 Lehre als Betreuer im Computational-Physik F-Praktikum
SS 2012 Lehre als Betreuer im Computational-Physik F-Praktikum

Jena, 8.7.2015

G Ehrenwörtliche Erklärung

Ich erkläre hiermit ehrenwörtlich, dass ich die vorliegende Arbeit selbständig, ohne unzulässige Hilfe Dritter und ohne Benutzung anderer als der angegebenen Hilfsmittel und Literatur angefertigt habe. Die aus anderen Quellen direkt oder indirekt übernommenen Daten und Konzepte sind unter Angabe der Quelle gekennzeichnet.

Bei der Auswahl und Auswertung dieser Arbeit haben mir die nachstehend aufgeführten Personen in der jeweils beschriebenen Weise unentgeltlich geholfen:

1. Dr. David Hilditch - beratend
2. Prof. Dr. Bernd Brüggemann - beratend
3. M.Sc. Tim Dietrich - beratend

Weitere Personen waren an der inhaltlich-materiellen Erstellung der vorliegenden Arbeit nicht beteiligt. Insbesondere habe ich hierfür nicht die entgeltliche Hilfe von Vermittlungs- bzw. Beratungsdiensten (Promotionsberater oder andere Personen) in Anspruch genommen. Niemand hat von mir unmittelbar oder mittelbar geldwerte Leistungen für Arbeiten erhalten, die im Zusammenhang mit dem Inhalt der vorgelegten Dissertation stehen.

Die Arbeit wurde bisher weder im In- noch im Ausland in gleicher oder ähnlicher Form einer anderen Prüfungsbehörde vorgelegt.

Die geltende Promotionsordnung der Physikalisch-Astronomischen Fakultät ist mir bekannt.

Ich versichere ehrenwörtlich, dass ich nach bestem Wissen die reine Wahrheit gesagt und nichts verschwiegen habe.

Jena, 8.7.2015

H Zusammenfassung

In dieser Arbeit wurde die Evolution von Gravitationswellen mit Hilfe von zwei populären Konfigurationen der Numerischen Relativitätstheorie studiert.

Hierzu wurde als erstes die BSSN-Konfiguration mit „Moving-Puncture“-Koordinaten und Finiten-Differenzen verwendet. Es hat sich herausgestellt, dass es nicht möglich ist, mit diesem Setup *starke* Brill-Wellen erfolgreich numerisch zu simulieren. Auftretende Koordinatensingularitäten während der Evolution führen zu einem Fehlschlagen der Simulationen. Es wurde festgestellt, dass Brill-Wellen mit ‚negativer Amplitude‘ sich geometrisch von Brill-Wellen mit positiver Amplitude unterscheiden und es möglich ist, den Kollaps dieser Daten zu einem Schwarzen Loch mit der BSSN-Konfiguration zu simulieren. Nahe der Schwelle zwischen dem Kollaps zu einem Schwarzen Loch schlagen auch diese Simulationen fehl. Es wurde daher geschlussfolgert, dass das BSSN-Setup sich nicht eignet, um den Kollaps von Gravitationswellen im Detail zu studieren.

In zweiten Ansatz wurde die GHG-Konfiguration verwendet. Hierzu wurde ein Computerprogramm – **bamps** – entwickelt. Es implementiert das GHG-Setup mit Hilfe einer pseudospektralen Methode auf einer „Cubed-Sphere“-Domäne. Für den äußeren Rand des Gebiets wurden verbesserte „Constraint-Preserving“-Randbedingungen hergeleitet und implementiert. Die Zwischenränder werden mit einer Penalty-Methode realisiert. Über eine Energieabschätzung konnte ein geeigneter Wert für den Penalty-Parameter gefunden werden, welcher für stabile Zwischenränder notwendig ist.

Spezielle Betrachtungen wurden für die Evolution von achsen-symmetrischen Daten in **bamps** angestellt. In diesem Fall erlaubt es die analytische Cartoon-Methode, die 3d Domäne auf eine 2d Ebene zu reduzieren. Der Horizontfinder – **AHloc** – wurde entwickelt, um in achsen-symmetrischen **bamps**-Daten nach scheinbaren Horizonten zu suchen.

Durch verschiedene numerische Experimente wurde gezeigt, dass die in **bamps** implementierte numerische Methode zu stabilen Simulationen führt, einschließlich exponentieller Konvergenz der numerischen Lösung und einer reduzierten Verletzung der Zwangsbedingungen am äußeren Rand. Weiterhin besitzt **bamps** eine hervorragende Recheneffizienz mit Geschwindigkeitssteigerungen von bis zu zwei

Ordnungen bei der Evolution von achsen- und oktant-symmetrischen Daten und einem nahezu perfekten Skalierungsverhalten auf bis zu mehreren tausend parallel rechnenden Computerkernen.

Das **bamps** Programm erlaubt stabile numerische Simulationen von einzelnen Schwarzen Löchern auf der **bamps**-, „Excision“-Domäne. Hierzu können verschiedene Anfangsdaten und Eichbedingungen verwendet werden. Ebenfalls ist es möglich, das Schwarze Loch durch eine einlaufende Gravitationswelle zu stören.

Im letzten Abschnitt der Arbeit wurden zentrierte Brill-Wellen mit positiver Amplitude in **bamps** evolviert. Hierbei wurden die Ergebnisse mit allen bisher veröffentlichten Arbeiten verglichen. Die meisten Ergebnisse konnten erfolgreich reproduziert werden. Darüber hinaus war es möglich, den Status von Simulationen zu klären, die bisher in numerischen Simulationen fehlgeschlagen sind. Die Ergebnisse, welche von Sorkin im Jahr 2010 publiziert wurden, konnten nicht bestätigt werden. Stattdessen haben die **bamps**-Simulationen gezeigt, dass der Kollaps auf einem Ring ein Koordinateneffekt ist und Amplituden, die von Sorkin als subkritisch eingestuft wurden, in Wirklichkeit superkritisch sind.

Es wurde demonstriert, dass **bamps** in Kombination mit **AHloc** verwendet werden kann, um den Kollaps einer superkritischen Brill-Wellen zu einem Schwarzen Loch zu evolvieren. Hierfür wurde ein dynamischer Excision-Algorithmus implementiert, welcher garantiert, dass der innere Rand der Domäne wohlgestellt bleibt.

Der kritische Bereich von zentrierten Brill-Wellen mit positiver Amplitude konnte auf $A_* \in [4.696, 4.698]$ eingegrenzt werden. Hierbei konnte im subkritischen Bereich noch kein exponentielles Skalierungsverhalten beobachtet werden. Im superkritischen Bereich konnte festgestellt werden, dass zwei voneinander getrennte Horizonte entstehen, die resultierende Raumzeit also zwei Schwarze Löcher enthält.